THE AERONAUTICAL QUARTERLY

A Journal devoted to Aeronautics and the Allied Sciences

Volume XII MAY 1961 Part 2

CONTENTS

Theoretical Pressure Distribution at Zero Lift at Supersonic Speeds for Slender Delta Wings having Fuselages of Circular Cross Section — *R. C. Lock*

The Axial Decay and Radial Spread of a Supersonic Jet Exhausting into Air at Rest — *J. H. Frauenberger and J. G. Forbister*

Compression Tests on Thin-Walled Cylinders — *M. Holmes*

Mass Transfer Cooling in a Boundary Layer — *D. G. Hurley*

The Elastic Stress Concentration Factors in Shouldered Shafts. Part I — *I. M. Allison*

Review of "Jet Propulsion Engines," edited by O. E. Lancaster — *J. R. Palmer*

LONDON

ROYAL AERONAUTICAL SOCIETY

4 HAMILTON PLACE W1

15/-

THE AERONAUTICAL QUARTERLY

Editorial Board

Dr. A. M. BALLANTYNE, T.D., B.Sc., Ph.D., F.R.Ae.S., Hon.F.C.A.I., F.I.A.S. (*Chairman*)

Mr. HAYNE CONSTANT, C.B., C.B.E., M.A., F.R.S., F.R.Ae.S.

Sir HAROLD ROXBEE COX, D.Sc., D.I.C., Ph.D., F.R.Ae.S., F.I.A.S.

Sir WILLIAM FARREN, C.B., M.B.E., M.A., D.Sc., F.R.S., Hon.F.R.Ae.S., Hon.F.I.A.S.

Sir ARNOLD HALL, M.A., F.R.S., F.R.Ae.S.

Sir ALFRED PUGSLEY, O.B.E., D.Sc., F.R.S., F.R.Ae.S.

Sir GEOFFREY TAYLOR, M.A., D.Sc., F.R.S., Hon.F.R.Ae.S.

Dr. P. B. WALKER, C.B.E., M.A., F.R.Ae.S.

Editor—E. C. PIKE, M.A., A.F.R.Ae.S.

Editorial Referees

Aerodynamics

(a) General

Sir LEONARD BAIRSTOW
Mr. D. KEITH-LUCAS
Prof. W. A. MAIR
Mr. L. F. NICHOLSON
Dr. R. C. PANKHURST
Mr. E. F. RELF
Prof. E. J. RICHARDS
Prof. B. THWAITES
Dr. D. KÜCHEMANN

(b) Fluid Motion

Dr. G. K. BATCHELOR
Mr. A. FAGE
Dr. D. W. HOLDER
Prof. L. HOWARTH
Dr. W. P. JONES
Dr. J. W. MACCOLL
Prof. J. H. PRESTON
Prof. H. B. SQUIRE
Prof. G. TEMPLE
Prof. G. N. WARD
Prof. A. D. YOUNG

(c) Stability and Control

Mr. L. W. BRYANT
Mr. S. B. GATES
Mr. G. H. LEE
Mr. M. B. MORGAN
Mr. H. H. B. M. THOMAS

Helicopters and Propellers

Prof. J. A. J. BENNETT
Mr. P. BRETT
Mr. L. G. FAIRHURST
Mr. R. HAFNER
Dr. G. S. HISLOP
Capt. R. N. LIPTROT

Instruments and Electrical Equipment

Dr. G. E. BAIRSTO
Sir GEORGE GARDNER
Dr. C. S. HUDSON
Mr. C. N. JAQUES
Mr. F. W. MEREDITH

Aircraft Design

Mr. R. BOORMAN
Mr. R. M. CLARKSON
Mr. A. N. CLIFTON
Mr. H. H. GARDNER
Mr. H. KNOWLER
Mr. F. H. POLLICUTT
Dr. A. E. RUSSELL
Mr. R. S. STAFFORD
Mr. W. H. STEPHENS

Radio and Radar

Mr. J. F. ATHERTON
Mr. B. G. GATES
Dr. R. L. SMITH ROSE
Dr. A. M. UTTLEY
Sir ROBERT WATSON-WATT

Aviation Medicine

Dr. K. G. BERGIN
Dr. A. BUCHANAN BARBOUR

Meteorology

Sir DAVID BRUNT
Mr. J. K. HARDY
Prof. P. A. SHEPPARD

Sound

Mr. W. MAKINSON
Mr. F. B. GREATREX
Mr. N. FLEMING

Aircraft Propulsion

Mr. A. D. BAXTER
Mr. A. V. CLEAVER
Sir A. H. ROY FEDDEN
Dr. S. HOOKER
Mr. A. R. HOWELL
Mr. W. H. LINDSEY
Mr. P. LLOYD
Prof. A. W. MORLEY
Dr. E. S. MOULT
Mr. N. S. MUIR
Mr. F. NIXON
Mr. F. M. OWNER
Mr. H. PEARSON
Mr. H. SAMMONS
Prof. O. A. SAUNDERS
Prof. A. G. SMITH

Air Transport

Mr. A. C. CAMPBELL ORDE
Mr. P. G. MASEFIELD
Mr. N. E. ROWE
Mr. B. S. SHENSTONE
Mr. W. TYE

Aircraft Accessories

Mr. A. E. BINGHAM
Mr. W. C. CLOTHIER
Mr. H. G. CONWAY
Sir GEORGE DOWTY
Mr. R. GRAHAM
Mr. C. D. HOLLAND

Performance

Mr. H. DAVIES
Mr. D. R. NEWMAN
Mr. A. H. YATES

Flight Testing

Mr. R. R. DUDDY
Mr. P. A. HUPTON
Mr. S. SCOTT HALL
Mr. H. L. STEVENS

Structures

Prof. J. H. ARGYRIS
Dr. A. J. BARRETT
Mr. A. C. BROWN
Mr. H. L. COX
Mr. D. J. FARRAR
Prof. W. S. HEMP
Prof. R. HILL
Mr. H. B. HOWARD
Col. H. T. JESSOP
Mr. E. D. KEEN
Mr. F. A. KERRY
Dr. D. M. A. LEGGETT
Mr. R. L. LICKLEY
Dr. E. H. MANSFIELD
Prof. S. C. REDSHAW
Mr. R. H. SANDIFER
Sir RICHARD SOUTHWELL

Fuels and Oils

Mr. E. L. BASS
Dr. J. W. DRINKWATER
Prof. F. H. GARNER
Prof. W. E. GARNER
Dr. K. E. W. RIDLER
Dr. C. G. WILLIAMS

Materials

Dr. L. AITCHISON
Dr. N. P. ALLEN
Mr. G. FORREST
Prof. N. F. MOTT
Mr. L. ROTHERHAM
Dr. H. SUTTON
Dr. C. SYKES

Vibration and Flutter

Mr. E. G. BROADBENT
Prof. A. R. COLLAR
Mr. H. TEMPLETON
Mr. M. O. W. WOLFE

Theoretical Pressure Distribution at Zero Lift at Supersonic Speeds for Slender Delta Wings having Fuselages of Circular Cross Section

R. C. LOCK, M.A., Ph.D.

(Aerodynamics Division, National Physical Laboratory)

SUMMARY: A method is developed for calculating the pressure distribution at zero lift for a class of slender configurations consisting of a wing of delta type plan form combined with a body of revolution of the same overall length. Slender-body and slender-wing theory are combined to take into account the interference between the wing and the fuselage. An expression is found for the pressure at a general point on the wing or fuselage, although some numerical integration is still needed. This expression is simplified to obtain algebraic formulae for the pressure at the wing-fuselage junction and along the top of the fuselage. A further simplification is possible when the fuselage radius is small compared with the local wing semi-span. A particular example is considered consisting of a "Newby" wing with a parabolic fuselage; pressure distributions and drag curves are calculated.

1. Introduction

The present programme of work in the United Kingdom on slender wings for supersonic aircraft began in the expectation that the final configuration would be of the "all wing" type, without a discrete fuselage, and accordingly most of the experimental and theoretical work that has been done up to the present has concentrated on this type of shape. More recent design studies, however, have suggested that such configurations may not in fact be the most suitable, and have tended to return to more conventional shapes in which a thin slender wing is mounted on a fuselage of circular cross section. Some experimental work on these designs is proceeding, but there does not yet seem to be available any corresponding theoretical treatment. The present paper is an attempt to fill part of this gap, at least as regards the calculation of the pressure distribution for symmetrical uncambered wing-fuselage combinations at zero lift.

There is already a considerable body of experimental evidence that, for the all-wing configurations mentioned previously, an adequate treatment is provided by the so-called "slender-wing" theory—that is, slender-body theory into which the further simplification has been introduced that the boundary condition may be

Received March 1961.

[The Aeronautical Quarterly, Vol. XII, May 1961]

satisfied in the mean plane of the wing; so that the flow may be represented, as is usual in the linearised theory of thin wings, by a source distribution in this plane of strength proportional to the local slope. Good agreement between this theory and experimentally measured pressure distributions has been obtained in general, in spite of the fact that many of the shapes tested appear to be far from "thin" in the usual sense, particularly over their forward portions. But when such wings are mounted on a fuselage of circular cross section, the theory in its present form is clearly inapplicable to the prediction of detailed pressure distributions without modification. Fortunately, the problem can be solved by the introduction of image sources within the fuselage, as has been done by Lighthill[1], Byrd[2] and Brebner[3]. These authors all restricted themselves to cases where the fuselage radius R, is constant; when this is allowed to vary, a further complication appears because the flow field due to the fuselage interferes with the boundary condition on the wing, so that an additional source distribution in the plane of the wing must be introduced to correct this effect.

There is also a possibility of obtaining improvements in performance by the use of wings having a blunt trailing edge. This refinement does not introduce any additional difficulties to the problem of calculating the pressure distribution, but does require a modification to the formula for the wave drag. This modification has been considered in Ref. 4, so that it is now possible to obtain both the detailed pressure distribution and overall wave drag for the most general wing-fuselage combination of this type. The algebraic complications tend to become excessive, however, except for the simplest shapes—one of which is considered in detail in Section 6—so that for future use a more purely numerical procedure might be desirable.

Notation

All co-ordinates and other lengths are measured in terms of the overall length of the wing-fuselage combination.

x, y, z Cartesian co-ordinates with the origin at the apex of the wing; the x-axis is in the direction of the undisturbed flow and the z-axis is normal to the mean plane of the wing

$r = \sqrt{(y^2 + z^2)}$

η alternative to y

$y_1, \eta_1 = y/s,\ \eta/s$ respectively

$\zeta = y + iz$

z_w half the local wing thickness

z_0 value of z_w at the centre section ($y = 0$)

s overall wing semi-span at the trailing edge

$\sigma(x)$ local wing semi-span

$R(x)$ fuselage radius

$R_1 = R/\sigma$

$R_B = R(1)$ fuselage radius at base

$R_{1B} = R_B/s$

$S(x)$ cross-sectional area of combination

$S_F(x) = \pi R^2$, cross-sectional area of fuselage

S_W cross-sectional area of exposed wing (*see* Fig. 1)

S_{WG} cross-sectional area of gross wing

S_{WF} cross-sectional area of part of wing blanketed by fuselage (*see* Fig. 1)

$S_{WF}\star$ *see* equation (33) and Fig. 1

$\lambda(x, y) = (\partial/\partial x)\, z_W(x, y)$, local wing slope

$$\lambda\star(x, y) = \lambda + RR' \frac{\partial}{\partial y}\left(\frac{z_W}{y}\right) \text{ (see equation (6))}$$

$$\Lambda\star(x, y) = \int_0^{\blacktriangleright} \frac{\partial z_W}{\partial x}(x, \eta)\, d\eta + RR' \frac{z_W}{y} \text{ (see equation (25))}$$

M Mach number

$\beta = \sqrt{(M^2 - 1)}$

U velocity of free stream

ρ_0 density of free stream

$q = \frac{1}{2}\rho_0 U^2$

p pressure

p_0 = pressure of free stream

$C_p = (p - p_0)/q$, pressure coefficient

C_{pF} pressure coefficient due to the fuselage alone

C_{pW} pressure coefficient due to wing and interference

$C_{pW}^{(0)}$ pressure coefficient at root section of gross wing alone

C_{pI} interference pressure coefficient at wing-fuselage junction (equation (64))

ΔC_p difference in pressure coefficient between the top of the fuselage and the wing junction

ϕ perturbation velocity potential

ϕ_1, ϕ_2 *see* equations (1) and (2)

D wave drag (for unit length)

V = (overall volume)/(length)^3

V_F = (volume of fuselage)/(length)^3

V_W = (volume of exposed wing)/(length)^3

$K_0 = (\pi/128)\, D/(qV^2)$ (*see* equation (82))

$F(x)$ *see* equation (18)

$G(x)$ *see* equation (29)

$H(x)$ *see* equation (54)

τ root thickness/chord ratio of gross wing

ε fineness ratio of fuselage

a length of equivalent pointed fuselage (*see* equation (69)) and Fig. 1)

$\lambda = \varepsilon/(sa)$

2. General Theory for Pressure Distributions

A typical wing-fuselage combination is shown in Fig. 1, which also shows the system of axes and notation used. The fuselage apex is at the origin, O, and the wing has a straight unswept trailing edge at $x=1$, $z=0$. The wing leading edge has the equation $y=\sigma(x)$, $z=0$, and $\sigma(1)=s$ is the ratio of the wing half-span to its length. The fuselage has the equation $r=R(x)$ and is assumed to be of the same length as the wing. The area of a cross section of the fuselage by a plane $x=$constant is denoted by $S_F(x)=\pi R^2$, and the cross-sectional area of the exposed wing is $S_W(x)$ so that the total area is $S(x)=S_F+S_W$.

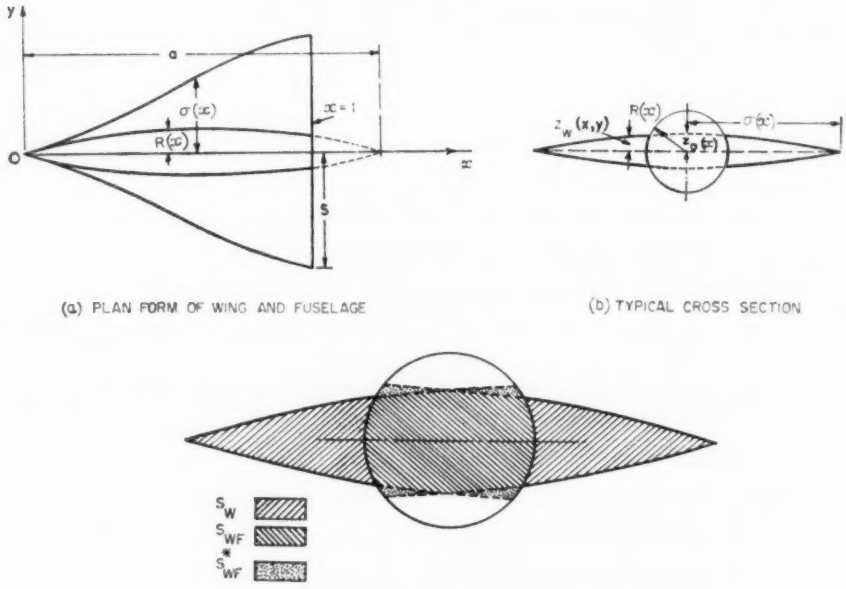

(a) PLAN FORM OF WING AND FUSELAGE

(b) TYPICAL CROSS SECTION

(c) DEFINITION OF CROSS-SECTIONAL AREAS

FIGURE 1.

The perturbation velocity potential $U\phi$ can, according to slender-body theory, be written in the form

$$\phi = \phi_1(x, y, z) + \phi_2(x), \quad . \quad . \quad . \quad . \quad . \quad (1)$$

where

$$\phi_2(x) = \int_0^x S''(\xi) \log \frac{\beta}{2(x-\xi)}\, d\xi \quad . \quad . \quad . \quad (2)$$

$$\beta = \sqrt{(M^2 - 1)}$$

and ϕ_1 is a harmonic function of y and z in the cross-flow planes $x = \text{constant}$, which has to satisfy the boundary conditions

$$\frac{\partial \phi_1}{\partial r} = \frac{dR}{dx} \quad . \quad . \quad . \quad . \quad . \quad . \quad . \quad (3)$$

on the fuselage $r = R(x)$ and

$$\frac{\partial \phi_1}{\partial z} = \pm \frac{\partial z_w}{\partial x}(x, y) \quad . \quad . \quad . \quad . \quad . \quad (4)$$

on the wing, where $z_w(x,y)$ is the wing thickness distribution. It is normally sufficiently accurate to satisfy the wing boundary condition (4) in the mean plane $z = 0$, but it will appear later that, in order to deal correctly with the interference effects, it is necessary to consider the flow induced by the fuselage at the actual surface of the wing ($z = z_w$).

These boundary conditions are to be satisfied by a suitable distribution of sources in the wing plane and at the centre of the fuselage. This can best be done by starting with the source systems appropriate to the wing and fuselage taken separately and then adding additional sources to allow for their mutual interference. Thus the exposed wing is represented initially by a source distribution of strength† $2\lambda(x, y)$ in the plane $z = 0$ ($R \leqslant |y| \leqslant \sigma$), where

$$\lambda(x, y) = \frac{\partial z_w}{\partial x}(x, y) \quad . \quad . \quad . \quad . \quad (5)$$

is the local streamwise slope of the wing surface; the fuselage is similarly represented by a line source along the axis Ox of strength $2\pi RR'(x) = S_F'(x)$.

We must now consider the additional normal component of velocity induced on the fuselage by the wing source distribution and on the wing by the fuselage source distribution. In the first place the velocity normal to the fuselage due to a wing source at $(x, y, 0)$ can be counteracted by an image system within the fuselage consisting of an equal source at the image point $(x, R^2/y, 0)$, together with an equal sink at the centre $(x, 0, 0)$. Secondly, the source $2\pi RR'$ representing the fuselage

†Taking the potential of a unit source to be $(1/2\pi) \log r$.

produces a radial velocity RR'/r, and this has a component normal to the wing surface which is approximately equal to

$$\frac{RR'}{y}\left(\frac{z_w}{y}-\frac{\partial z_w}{\partial y}\right)=-RR'\frac{\partial}{\partial y}\left(\frac{z_w}{y}\right).$$

To correct for this effect we must therefore introduce an equal and opposite source distribution in the wing plane, thereby modifying the original strength λ, defined in equation (5), to

$$\lambda^\star(x,y)=\lambda(x,y)+RR'\frac{\partial}{\partial y}\left(\frac{z_w}{y}\right). \quad . \quad . \quad . \quad . \quad (6)$$

This modified source distribution $\lambda^\star$, in the plane $z=0$, together with its image system in the fuselage, represents correctly the flow due to the exposed wing and the mutual interference with the fuselage. Taking into account both halves of the wing ($y>0$ and $y<0$), we obtain the following expression for the harmonic part of the velocity potential:—

$$\phi_1(x,y,z)=\frac{S_F'(x)}{2\pi}\log r+\frac{1}{\pi}\int_R^\sigma \lambda^\star(x,\eta)\log\left|\frac{(\zeta^2-\eta^2)(\zeta^2\eta^2-R^4)}{\zeta^2\eta^2}\right|d\eta, \quad . \quad (7)$$

where $\zeta=y+iz$ and $\lambda^\star$ is defined by equation (6).

It is interesting to note that the expression (7) for ϕ_1 corresponds to a total source strength $Q(x)$ in the transverse plane, where

$$Q(x)=S_F'(x)+4\int_R^\sigma \lambda^\star(x,\eta)\,d\eta \quad \text{(since the total strength of the image sources is zero)}$$

$$=S_F'(x)+4\int_R^\sigma \frac{\partial z_w}{\partial x}(x,\eta)\,d\eta-4R'z_w(x,R) \quad \text{(from equation (6))}$$

$$=S_F'(x)+4\frac{d}{dx}\int_R^\sigma z_w(x,\eta)\,d\eta$$

$$=S_F'(x)+S_w'(x),$$

since $S_w(x)=4\int_R^\sigma z_w(x,\eta)\,d\eta$,

provided that the wing is thin relative to the fuselage. This is, of course, as it should be but, if the modification to λ given by equation (6) had not been used, the

total source strength $Q(x)$ would have been in error (by the amount $4R'z_w(x, R)$). The reason for this discrepancy can be seen more clearly by considering the harmonic flow in a typical transverse plane. The fuselage source (of strength $2\pi RR'$) produces an outward radial velocity R' at the circle $r=R$ representing the fuselage, as required by the boundary condition there; but the total flux across that part of the circle *external to the wing* is not $2\pi RR'$, as it would be for the fuselage alone, but $2\pi RR' - 4R'z_w(x, R)$. This deficiency $4R'z_w(x, R)$ can be thought of as flowing across the two small arcs of the circle blanketed by the wing, and thereby disturbing the wing boundary condition, as already described.

It might be imagined that the neglect of the effect just described would lead only to a very small error in the resultant pressure calculations. It may be shown, however, that this is not the case, and that in fact the error would be of the same order of magnitude as the other interference effects.

The form taken by equation (7) when R is constant has been obtained previously by Lighthill[1], Byrd[2] and Brebner[3].

It is convenient to rewrite equation (1) in the form

$$\phi = \phi_F + \phi_W,$$

where ϕ_F is the potential due to the fuselage alone,

$$\phi_F = \frac{1}{2\pi}\left[S_F'(x)\log \tfrac{1}{2}\beta r - \int_0^x S_F''(\xi)\log(x-\xi)\,d\xi\right] \quad . \quad . \quad (8)$$

and ϕ_W is the additional potential due to the wing, allowing for interference effects,

$$\phi_W = \frac{1}{2\pi}\int_0^x S_W''(\xi)\log\frac{\beta}{2(x-\xi)}\,d\xi + \frac{1}{\pi}\int_R^\sigma \lambda^\star(x,\eta)\log\left|\frac{(\zeta^2-\eta^2)(\zeta^2\eta^2-R^4)}{\zeta^2\eta^2}\right|d\eta. \quad (9)$$

The pressure coefficient C_p is given in the usual way by

$$C_p = -2\frac{\partial\phi}{\partial x} - \left(\frac{\partial\phi}{\partial y}\right)^2 - \left(\frac{\partial\phi}{\partial z}\right)^2. \quad . \quad . \quad . \quad (10)$$

Before proceeding further, it is desirable to enquire to what extent we should take into account the quadratic terms $(\partial\phi/\partial y)^2+(\partial\phi/\partial z)^2$ in equation (10); these are normally included in slender-body theory but are neglected in "thin-wing" theory. To do this it is necessary to examine the orders of magnitude of the various terms involved. Suppose that the wing thickness ratio and slopes are of order τ and that the fuselage thickness ratio and slopes are of order ε; the ratio of wing semi-span to length is, of course, s. Then the relevant orders of magnitude are given by Table I. The various pressure terms are thus of the orders of magnitude given in Table II.

TABLE I

Quantity	*Order of magnitude*
S_W	τs
S_F	ε^2
ϕ_F, $\dfrac{\partial \phi_F}{\partial x}$	$\varepsilon^2 \log \varepsilon$
$\dfrac{\partial \phi_F}{\partial r}$, $\dfrac{\partial \phi_F}{\partial y}$, $\dfrac{\partial \phi_F}{\partial z}$	ε (on and near the fuselage)
ϕ_W, $\dfrac{\partial \phi_W}{\partial x}$	$\tau s \log s$
$\dfrac{\partial \phi_W}{\partial y}$, $\dfrac{\partial \phi_W}{\partial z}$	τ

TABLE II

Wing	Linear	$(\partial \phi_W / \partial x)$	$\tau s \log s$
	Quadratic	$(\partial \phi_W/\partial y)^2 + (\partial \phi_W/\partial z)^2$	τ^2
Fuselage	Linear	$(\partial \phi_F / \partial x)$	$\varepsilon^2 \log \varepsilon$
	Quadratic	$(\partial \phi_F / \partial r)^2$	ε^2
Interference			$\tau \varepsilon \log \varepsilon$

Provided that τs and ε^2 are of comparable size, which will be the case when the wings and fuselage have comparable cross-sectional areas, then the pressure contributions due to the fuselage (both linear and quadratic terms) and the linear wing term will be of equal importance, at least on and near the fuselage. On the other hand, the restriction to "thin-wing" theory for the wing means that the quadratic wing terms *must* be neglected, so that τ should be small compared with $s \log s$ and ε if the theory is to be strictly applicable. Physically this means that the wing should be "thin" compared to the fuselage, even in transverse cross section; but the results of experiments on all-wing configurations suggest that this may not prove a serious restriction.

The argument just given shows that it is legitimate to express the pressure coefficient as the sum of a contribution C_{pF} due to the fuselage alone, which should be obtained by full slender-body theory including the quadratic term†, together with a linear term C_{pW} due to the wings and interference effects.

Thus
$$C_p = C_{pF} + C_{pW}, \qquad (11)$$

with
$$C_{pF} = -2\frac{\partial \phi_F}{\partial x} - \left(\frac{\partial \phi_F}{\partial r}\right)^2$$
$$= -\frac{1}{\pi}\left[S_F''(x)\log(\tfrac{1}{2}\beta r) - S_F''(0)\log x - \int_0^x S_F'''(\xi)\log(x-\xi)\,d\xi\right] - \left(\frac{RR'}{r}\right)^2 \qquad (12)$$

†It might in fact be desirable to use more accurate methods for C_{pF}, particularly off the fuselage, since slender-body theory is only strictly valid in the immediate neighbourhood of the body concerned.

and $C_{pw} = -2\dfrac{\partial \phi_w}{\partial x}$

$$= -\frac{1}{\pi}\left[S_w''(x)\log(\tfrac{1}{2}\beta) - S_w''(0)\log x - \int_0^x S_w'''(\xi)\log(x-\xi)\,d\xi + 2\frac{\partial I}{\partial x}\right] \quad . \quad . \quad . \quad (13)$$

$$\text{where} \quad I = \int_R^{\sigma(x)} \lambda^\star(x,\eta)\log\left|\frac{(\zeta^2-\eta^2)(\zeta^2\eta^2-R^4)}{\zeta^2\eta^2}\right| d\eta; \quad . \quad . \quad (14)$$

here $\zeta = y + iz$ as before.

Thus on the wing, at the point $(x, y, 0)$,

$$\frac{\partial I}{\partial x} = \int_R^{\sigma} \frac{\partial \lambda^\star}{\partial x}(x,\eta)\log\left|\frac{(y^2-\eta^2)(y^2\eta^2-R^4)}{y^2\eta^2}\right| d\eta - 4R^3R'(x)\int_R^{\sigma}\frac{\lambda^\star(x,\eta)}{(y^2\eta^2-R^4)}\,d\eta +$$

$$+\sigma'(x)\,\lambda^\star(x,\sigma)\log\left|\frac{(y^2-\sigma^2)(y^2\sigma^2-R^4)}{y^2\sigma^2}\right| - 2R'(x)\,\lambda^\star(x,R)\log\left|\frac{y^2-R^2}{y}\right| \quad (15)$$

Equations (11) to (15) provide a general expression for the pressure due to a wing-fuselage combination of the type under consideration. All the terms except the last (equation (15)) are already familiar in this subject. In particular, Lord and Brebner[5] have shown that, for area distributions which can be conveniently expressed as power series in x, so that

$$S'''(x) = \sum_{n=0}^{N} T_n x^n, \quad . \quad . \quad . \quad . \quad . \quad . \quad (16)$$

then

$$\int_0^x S'''(\xi)\log(x-\xi)\,d\xi = \{S''(x) - S''(0)\}\log x - F(x), \quad . \quad . \quad (17)$$

where $$F(x) = \sum_{n=0}^{N} \sigma_n T_n x^{n+1}$$

and $$\sigma_n = \frac{1}{n+1}\left(1 + \tfrac{1}{2} + \ldots + \frac{1}{n+1}\right).$$

In fact, it may easily be seen that

$$F(x) = \int_0^x \frac{S''(x) - S''(\xi)}{x-\xi}\,d\xi; \quad . \quad . \quad . \quad . \quad (18)$$

this may be used to define $F(x)$ for more general types of area distribution.

Equations (10) and (11) may therefore be written in the form

$$C_{pF} = -\frac{1}{\pi}\left[S_F''(x)\log\frac{\beta r}{2x} + F_F(x)\right] - \left(\frac{RR'}{r}\right)^2 \quad . \quad . \quad . \quad (19)$$

and

$$C_{pW} = -\frac{1}{\pi}\left[S_W''(x)\log\frac{\beta}{2x} + F_W(x) + 2\frac{\partial I}{\partial x}\right] . \quad . \quad . \quad (20)$$

The only additional complications introduced by the present problem are thus concentrated in the term $\partial I/\partial x$ (equation (15)); but they turn out to be very considerable, except in the simplest examples.

3. Pressure Distributions at the Wing-Fuselage Junction

3.1. General

In cases where the wing slope $\lambda(x, \eta)$ can be expressed as a polynomial in η (so that $\lambda^\star$ consists of a polynomial together with a term in η^{-2}), it is possible to express $\partial I/\partial x$ (equation (15)) explicitly in terms of elementary functions; but for a general position on the wing the results are so complicated that it would seem more profitable to use purely numerical methods of evaluation. It is not proposed to pursue the matter further in the present paper; but fortunately it is possible to achieve a considerable simplification as regards the pressure distribution along the wing-fuselage junction, which is probably the most important region from a practical point of view.

If we take the limit of equation (15) as $\zeta \longrightarrow R$, we find the following expression for $\partial I/\partial x$ in the junction

$$\left.\frac{\partial I}{\partial x}\right|_J = 2\int_R^\sigma \frac{\partial\lambda^\star}{\partial x}(x,\eta)\log\left(\frac{\eta^2-R^2}{\eta}\right)d\eta + 2\sigma'(x)\,\lambda^\star(x,\sigma)\log\left(\frac{\sigma^2-R^2}{\sigma}\right) -$$

$$-2R'(x)\left\{\int_R^\sigma \frac{\partial\lambda^\star}{\partial\eta}(x,\eta)\log\left(\frac{\eta+R}{\eta-R}\right)d\eta + \lambda^\star(x,\sigma)\log\left(\frac{\sigma-R}{\sigma+R}\right) + \lambda^\star(x,R)\log 4R\right\}$$

. . . (21)

This expression can be simplified by separating out the terms involving logarithms, which can be done in the following way. Consider first the integral

$$\int_R^\sigma \frac{\partial\lambda^\star}{\partial\eta}(x,\eta)\log\left(\frac{\eta+R}{\eta-R}\right)d\eta.$$

Now $$\int_R^\sigma \frac{\partial\lambda^\star}{\partial\eta}(x,\eta)\log(\eta-R)\,d\eta = \int_R^\sigma \frac{\partial}{\partial\eta}\left\{\lambda^\star(x,\eta)-\lambda^\star(x,R)\right\}\log(\eta-R)\,d\eta,$$

and, integrating by parts, this becomes

$$\{\lambda^\star(x,\sigma)-\lambda^\star(x,R)\}\log(\sigma-R)-\int_R^\sigma \frac{\lambda^\star(x,\eta)-\lambda^\star(x,R)}{\eta-R}\,d\eta; \qquad (22)$$

the integrand is now non-singular at $\eta=R$ and, if $z(x,\eta)$ can be expressed as a polynomial in η, so also can the integral. Similarly,

$$\int_R^\sigma \frac{\partial\lambda^\star}{\partial\eta}(x,\eta)\log(\eta+R)\,d\eta=\{\lambda^\star(x,\sigma)-\lambda^\star(x,-R)\}\log(\sigma+R)-$$

$$-\{\lambda^\star(x,R)-\lambda^\star(x,-R)\}\log 2R-\int_R^\sigma \frac{\lambda^\star(x,\eta)-\lambda^\star(x,-R)}{\eta+R}\,d\eta. \qquad (23)$$

For this equation to have a meaning it is necessary that the analytic continuation of $\lambda^\star(x,\eta)$ for negative values of η should be known; there is no difficulty here if z is given as a polynomial in η. Note that for wings where z is not an analytic function of η over the whole range $(-\eta,\ \eta)$ (in particular when the cross section has a discontinuity in slope at $\eta=0$), $\lambda^\star(x,-\eta)$ is *not* simply the value of $\lambda^\star$ at the point $(x,-\eta)$ on the actual wing. For example, if the wing has rhombic cross sections, so that $z=a+b|\eta|$, then

$$\lambda^\star(x,\eta)=a'+b'\eta-\frac{aRR'}{\eta^2};$$

thus

$$\lambda^\star(x,-R)=a'-b'R-\frac{aR'}{R},$$

while the value of $\lambda^\star$ at the point $(x,-R)$ of the wing is the same as at $(x,+R)$, namely

$$a'+b'R-\frac{aR'}{R}.$$

Combining these two results, (22) and (23), we find that

$$\int_R^\sigma \frac{\partial\lambda^\star}{\partial\eta}(x,\eta)\log\left(\frac{\eta+R}{\eta-R}\right)d\eta+\lambda^\star(x,\sigma)\log\left(\frac{\sigma-R}{\sigma+R}\right)+\lambda^\star(x,R)\log 4R$$

$$=\lambda^\star(R)\log(\sigma-R)-\lambda^\star(-R)\log(\sigma+R)+\lambda^\star(R)\log 2+\lambda^\star(-R)\log 2R+$$

$$+\int_R^\sigma\left\{\frac{\lambda^\star(x,\eta)-\lambda^\star(x,R)}{\eta-R}-\frac{\lambda^\star(x,\eta)-\lambda^\star(x,-R)}{\eta+R}\right\}d\eta. \qquad (24)$$

It is convenient to express $\lambda^\star$ as the sum of an even and an odd function of η;

thus $$\lambda^\star(x,\eta)=\lambda_E^\star(x,\eta)+\lambda_O^\star(x,\eta),$$

where $$\lambda_E^\star=\tfrac{1}{2}[\lambda^\star(x,\eta)+\lambda^\star(x,-\eta)]$$

$$\lambda_O^\star=\tfrac{1}{2}[\lambda^\star(x,\eta)-\lambda^\star(x,-\eta)].$$

(In the example quoted, $\lambda_E^\star=a'-aRR'/\eta^2$ and $\lambda_O^\star=b'\eta$).

The right-hand side of equation (24) then takes the form

$$\lambda_E^\star(x,R)\log\left(\frac{4R(\sigma-R)}{\sigma+R}\right)+\lambda_O^\star(x,R)\log\left(\frac{\sigma^2-R^2}{R}\right)+$$

$$+2\int_R^\sigma \frac{R\{\lambda^\star(x,\eta)-\lambda_E^\star(x,R)\}-\eta\lambda_O^\star(x,R)}{\eta^2-R^2}\,d\eta. \quad (24a)$$

In order to apply the same process to the integral

$$\int_R^\sigma \frac{\partial\lambda^\star}{\partial x}(x,\eta)\log\left(\frac{\eta}{\eta^2-R^2}\right)d\eta,$$

it is first necessary to define the function

$$\Lambda^\star(x,\eta)=\int_0^\eta \frac{\partial z_w}{\partial x}(x,y)\,dy+\frac{RR'z_w}{\eta}, \quad (25)$$

so that $$\frac{\partial\Lambda^\star}{\partial\eta}=\lambda^\star,$$

$$\Lambda^\star=\Lambda_E^\star+\Lambda_O^\star, \quad (26)$$

where $\Lambda_E^\star$ and $\Lambda_O^\star$ are even and odd functions of η respectively; clearly

$$\frac{\partial\Lambda_E^\star}{\partial\eta}=\lambda_O^\star$$

and $$\frac{\partial\Lambda_O^\star}{\partial\eta}=\lambda_E^\star.$$

Applying the technique described, we find that

$$\int_R^\sigma \frac{\partial \lambda^\star}{\partial x}(x,\eta)\log\left(\frac{\eta^2-R^2}{\eta}\right)d\eta+\sigma'(x)\,\lambda^\star(x,\sigma)\log\left(\frac{\sigma^2-R^2}{\sigma}\right)$$

$$=\left[\frac{\partial \Lambda^\star}{\partial x}(x,\sigma)+\sigma'\lambda^\star(x,\sigma)\right]\log\left(\frac{\sigma^2-R^2}{\sigma}\right)-$$

$$\frac{\partial \Lambda_E^\star}{\partial x}(x,R)\log\left(\frac{\sigma^2-R^2}{R}\right)-\frac{\partial \Lambda_O^\star}{\partial x}(R)\log\left(\frac{4R(\sigma-R)}{\sigma+R}\right)-$$

$$-2\int_R^\sigma \frac{\eta\left\{\frac{\partial \Lambda^\star}{\partial x}(x,\eta)-\frac{\partial \Lambda_E^\star}{\partial x}(x,R)\right\}-R\frac{\partial \Lambda_O^\star}{\partial x}(x,R)}{(\eta^2-R^2)}+\int_R^\sigma \frac{\partial \Lambda}{\partial x}(x,\eta)\frac{d\eta}{\eta}. \quad . \quad . \quad . \quad (27)$$

Substituting from equations (24*a*) and (27) into equation (21), and using the relations

$$\frac{d}{dx}\left[\Lambda^\star(x,\sigma)\right]=\frac{\partial \Lambda^\star}{\partial x}(x,\sigma)+\sigma'\lambda^\star(x,\sigma)$$

$$\frac{d}{dx}\left[\Lambda_E^\star(x,R)\right]=\frac{\partial \Lambda_E^\star}{\partial x}(x,R)+R'\lambda_O^\star(x,R)$$

$$\frac{d}{dx}\left[\Lambda_O^\star(x,R)\right]=\frac{\partial \Lambda_O^\star}{\partial x}(x,R)+R'\lambda_E^\star(x,R),$$

we find that

$$\left.\frac{\partial I}{\partial x}\right|_J=2\frac{d}{dx}\left[\Lambda^\star(x,\sigma)\right]\log\left(\frac{\sigma^2-R^2}{\sigma}\right)-2\frac{d}{dx}\left[\Lambda_E^\star(x,R)\right]\log\left(\frac{\sigma^2-R^2}{R}\right)-$$

$$-2\frac{d}{dx}\left[\Lambda_O^\star(x,R)\right]\log\left(\frac{4R(\sigma-R)}{\sigma+R}\right)+\tfrac{1}{2}G(x), \quad . \quad (28)$$

where

$$G(x)=-8\int_R^\sigma \frac{\left[\eta\left\{\frac{\partial \Lambda^\star}{\partial x}(x,\eta)-\frac{\partial \Lambda_E^\star}{\partial x}(x,R)\right\}+RR'\{\lambda^\star(x,\eta)-\lambda_E^\star(x,R)\}-R\frac{\partial \Lambda_O^\star}{\partial x}(x,R)-\eta R'\lambda_O^\star(x,R)\right]}{(\eta^2-R^2)}d\eta+$$

$$+4\int_R^\sigma \frac{\partial \Lambda^\star}{\partial x}(x,\eta)\frac{d\eta}{\eta}. \quad . \quad (29)$$

(Note that in cases where $z(x, \eta)$ is not a purely even function of η, so that $\Lambda_E^\star \neq 0$, there may be an additional term in $\log(\sigma/R)$, due to the last term in equation (29); it does not seem desirable to separate this, since no additional simplification is achieved in the final expression for the pressure.)

If we define a gross wing cross-sectional area

$$S_{WG}(x) = 4\int_0^\sigma z_W(x, \eta)\, d\eta, \qquad (30)$$

and write

$$S_{WF} = S_{WG} - S_W, \qquad (31)$$

so that

$$S_{WF}(x) = 4\int_0^R z_W(x, \eta)\, d\eta \qquad (32)$$

is the wing area blanketed by the fuselage, then it is easy to show that

$$\Lambda^\star(x, \sigma) = \tfrac{1}{4} S_{WG}'(x)$$

and

$$\Lambda^\star(x, R) = \tfrac{1}{4} S_{WF}'(x).$$

In cases where z is not a purely even function of η, it is necessary to define an additional area

$$S_{WF}^\star = 4\int_0^R \{z_W(x, -\eta) - z_W(x, \eta)\}\, d\eta; \qquad (33)$$

then

$$\Lambda_E^\star(x, R) = -\tfrac{1}{8} S_{WF}^{\star\prime}(x).$$

The physical definition of these areas is shown in Fig. 1.

In terms of the areas S_W, S_{WF} and $S_{WF}^\star$, the final expression for the pressure at the wing-fuselage junction is found from equations (19) and (20) to be

$$C_{pJ} = C_{pF}|_J + C_{pW}|_J, \qquad (34)$$

where

$$C_{pF}|_J = -\frac{1}{\pi}\left[S_F''(x)\log\frac{\beta R}{2x} + F_F(x)\right] - R'^2 \qquad (35)$$

and

$$C_{pW}|_J = -\frac{1}{\pi}\left[S_W''(x)\log\left\{\frac{\beta\sigma}{2x}\left(1-\frac{R^2}{\sigma^2}\right)\right\} + S_{WF}''(x)\log\left\{\frac{(\sigma+R)^2}{4\sigma R}\right\} + S_{WF}^{\star\prime\prime}\log\left\{\frac{\sigma+R}{2R}\right\} + F_W(x) + G(x)\right] \qquad (36)$$

Here $F_F(x)$ and $F_W(x)$ are defined by equation (18), using the appropriate area distribution, and $G(x)$ is defined by equation (29).

When z can be expressed as a polynomial in η^2 only, so that $\lambda^\star$ is a purely even function and $\Lambda^\star$ is purely odd, equation (36) simplifies further to

$$C_{pW}|_J = -\frac{1}{\pi}\left[S_W''(x)\log\left\{\frac{\beta\sigma}{2x}\left(1-\frac{R^2}{\sigma^2}\right)\right\} + S_{WF}''(x)\log\left\{\frac{(\sigma+R)^2}{4\sigma R}\right\} + F_W(x)+G(x)\right] \quad . \quad . \quad . \quad (36a)$$

$$\text{with } G(x) = -8\int_R^\sigma \frac{\eta\,\dfrac{\partial\Lambda^\star}{\partial x}(x,\eta) - R\,\dfrac{\partial\Lambda^\star}{\partial x}(x,R) + RR'\{\lambda^\star(x,\eta)-\lambda^\star(x,R)\}}{(\eta^2-R^2)}\,d\eta + $$

$$+4\int_R^\sigma \frac{\partial\Lambda^\star}{\partial x}(x,\eta)\,\frac{d\eta}{\eta} \quad . \quad . \quad . \quad (29a)$$

If $z_W(x,\eta) = \sum_{n=0}^{N} a_n(x)\,\eta^n$, then it can be shown that $G(x) = \sum_0^N G_n(x)$,

where

$$G_n(x) = -8\left[\frac{a_n''}{n+1}I_{n+2} + \frac{I_n}{a_n}\frac{d}{dx}(a_n^2RR') + (n-1)\,a_n(RR')^2 I_{n-2}\right] +$$

$$+4\left[\frac{a_n''}{(n+1)^2}(\sigma^{n+1}-R^{n+1}) + \frac{1}{(n-1)}(\sigma^{n-1}-R^{n-1})\frac{d}{dx}(a_nRR')\right] \quad (n\neq 1), \quad (37)$$

$$\text{and} \qquad I_n = \begin{cases} \displaystyle\int_R^\sigma \frac{\eta^n - R^n}{\eta^2-R^2}\,d\eta & \text{if } n \text{ is even} \\ \displaystyle\int_R^\sigma \eta\,\frac{\eta^{n-1}-R^{n-1}}{\eta^2-R^2}\,d\eta & \text{if } n \text{ is odd.} \end{cases}$$

The first three functions G_0, G_1 and G_2 are given by

$$G_0 = -4(\sigma-R)\left[z_0'' - \frac{R}{\sigma}\frac{d}{dx}\left(\frac{z_0R'}{R}\right)\right] \quad \text{(writing } a_0 = z_0\text{)},$$

$$G_1 = -a_1''(\sigma^2 - R^2) + 4\frac{d}{dx}(a_1 RR')\log\frac{\sigma}{R},$$

and $$G_2 = -\frac{4}{9}\sigma^2(\sigma - R)\left(1 + \frac{R}{\sigma} + 7\frac{R^2}{\sigma^2}\right)a_2'' - 4(\sigma - R)\left\{\frac{d}{dx}(a_2 RR') + 2a_2' RR'\right\}.$$

In all the preceding work, no assumption has been made about the wing cross-sectional shapes except that z_w should be expressible in the form of a finite polynomial $\Sigma\, a_n(x)\,\eta^n$. Thus equation (36), used in conjunction with standard techniques of polynomial fitting, could form the basis of a numerical method for calculating the junction pressure distribution for a wing of arbitrary shape. It is not proposed to proceed further in this direction in the present paper; but in the two following sections explicit formulae will be given for two types of wings having "similar" cross sections—rhombic and parabolic respectively.

3.2. Rhombic Cross Sections

The wing thickness distribution has the equation

$$z_w(x, y) = z_0\left(1 - \frac{y}{\sigma}\right), \qquad (38)$$

so that

$$\lambda^\star = z_0' - \left(\frac{z_0}{\sigma}\right)' y - \frac{RR' z_0}{y^2}, \qquad (39)$$

$$\Lambda^\star = -\frac{RR' z_0}{\sigma} - \tfrac{1}{2}\left(\frac{z_0}{\sigma}\right)' y^2 + z_0' y + \frac{RR' z_0}{y}, \qquad (40)$$

$$S_w = 2z_0\sigma\left(1 - \frac{R}{\sigma}\right)^2, \qquad (41)$$

$$S_{WF} = 4z_0 R\left(1 - \tfrac{1}{2}\frac{R}{\sigma}\right), \qquad (42)$$

and

$$S_{WF}^\star = \frac{4R^2 z_0}{\sigma}. \qquad (43)$$

Substituting in equations (36) and (37) (with $a_0 = z_0$ and $a_1 = -z_0/\sigma$), and combining the term in $\log(\sigma/R)$ in G_1 with the other logarithmic terms, we obtain

$$C_{pw}|_J = -\frac{1}{\pi}\left[S_w''(x)\log\left\{\frac{\beta\sigma}{2x}(1 - R_1^2)\right\} + 4(z_0 R)''\log\left\{\frac{(1 + R_1)^2}{4R_1}\right\} + \right.$$
$$+ 2\frac{d}{dx}\left\{R^2\left(\frac{z_0}{\sigma}\right)'\right\}\log\frac{1}{R_1} + F_w(x) - 4(\sigma - R)z_0'' +$$
$$\left. + (\sigma^2 - R^2)\left(\frac{z_0}{\sigma}\right)'' + 4R(1 - R_1)\frac{d}{dx}\left(\frac{z_0 R'}{R}\right)\right]. \qquad (44)$$

In this equation, $R_1(x)=(R/\sigma)$; $S_W(x)$ is given by equation (41), and $F_W(x)$ is derived from it by means of equation (17) or (18).

3.3. Parabolic Cross Sections

The wing thickness distribution has the equation

$$z_W = z_0\left(1-\frac{y^2}{\sigma^2}\right), \qquad (45)$$

so that

$$\lambda^\star = z_0' - \frac{z_0RR'}{\sigma^2} - \left(\frac{z_0}{\sigma^2}\right)' y^2 - \frac{z_0RR'}{y^2}, \qquad (46)$$

$$\Lambda^\star = \left(z_0' - \frac{z_0RR'}{\sigma^2}\right) y - \tfrac{1}{3}\left(\frac{z_0}{\sigma^2}\right)' y^3 + \frac{z_0RR'}{y}, \qquad (47)$$

$$S_W = \frac{4}{3} z_0\sigma\,(2-3R_1+R_1^3), \qquad (48)$$

$$S_{WF} = 4z_0R\,(1-\tfrac{1}{3}R_1^2) \qquad (49)$$

and $S_{WF}^\star = 0$.

In this case we obtain

$$C_{pW}|_J = -\frac{1}{\pi}\left[S_W''(x)\log\left\{\frac{\beta\sigma}{2x}(1-R_1^2)\right\} + 4\frac{d^2}{dx^2}\{z_0R\,(1-\tfrac{1}{3}R_1^2)\}\log\left\{\frac{(1+R_1)^2}{4R_1}\right\} + F_W(x)+G(x)\right]. \qquad (50)$$

where

$$G(x) = -4\,(\sigma-R)\left\{z_0'' - \frac{\sigma^2}{9}\left(\frac{z_0}{\sigma^2}\right)''(1+R_1+7R_1^2) - R_1\frac{d}{dx}\left(\frac{z_0R'}{R}\right) - \frac{d}{dx}\left(\frac{z_0RR'}{\sigma^2}\right) - 2RR'\left(\frac{z_0}{\sigma^2}\right)'\right\}. \qquad (51)$$

4. Pressure Distributions along the Top of the Fuselage

It is also possible to obtain relatively simple expressions for the pressure distribution along the top of the fuselage ($y=0$, $z=R$).

Writing $\zeta = iR$ in equation (14), and differentiating the result with respect to x, we obtain equation (52) which follows†.

†*See* the footnote on p. 112.

$$\frac{\partial I}{\partial x} = 2\int_R^\sigma \frac{\partial \lambda^\star}{\partial x}(x,\eta)\log\left(\frac{\eta^2+R^2}{\eta}\right)d\eta + 4RR'\int_R^\sigma \frac{\lambda^\star(x,\eta)\,d\eta}{\eta^2+R^2} +$$

$$+ 2\sigma'\lambda^\star(x,\sigma)\log\left(\frac{\sigma^2+R^2}{\sigma}\right) - 2R'\lambda^\star(x,R)\log 2R. \quad (52)^\dagger$$

Making use of the function $\Lambda^\star(x,\eta)$ defined by equation (25), such that $\lambda^\star = \partial\Lambda^\star/\partial\eta$, this may be written

$$\frac{\partial I}{\partial x} = 2\frac{d}{dx}\left\{\Lambda^\star(x,\sigma)\right\}\log\left(\frac{\sigma^2+R^2}{\sigma}\right) - 2\frac{d}{dx}\left\{\Lambda^\star(x,R)\right\}\log 2R +$$

$$+ 4\int_R^\sigma \frac{RR'\lambda^\star(x,\eta) - \eta\dfrac{\partial\Lambda^\star}{\partial x}(x,\eta)}{\eta^2+R^2}\,d\eta + 2\int_R^\sigma \frac{\partial\Lambda^\star}{\partial x}(x,\eta)\frac{d\eta}{\eta}. \quad (53)$$

If we compare equation (53), which gives the value of $\partial I/\partial x$ at the top of the fuselage, with equation (28), which gives the value at the wing-fuselage junction, we notice that many of the terms are similar; and all the other terms in the equations for the pressure ((19) and (20)) are identical. It is therefore possible, by subtracting equation (28) from equation (53), to obtain the following expression for the *difference* in pressure between the top of the fuselage and the junction:—

$$\Delta C_p = C_p(\text{top}) - C_p(\text{junction})$$

$$= -\frac{1}{\pi}\left[S_{WG}''(x)\log\left(\frac{\sigma^2+R^2}{\sigma^2-R^2}\right) - S_{WF}''\log\tfrac{1}{2}\left(\frac{\sigma+R}{\sigma-R}\right) - \right.$$

$$\left. - S_{WF}^{\star\prime\prime}\log\left(\frac{\sigma+R}{2R}\right) + H(x)\right] \quad (54)$$

where $H(x) = 8\displaystyle\int_R^\sigma \left[\frac{RR'\lambda^\star(x,\eta) - \eta\dfrac{\partial\Lambda^\star}{\partial x}(x,\eta)}{\eta^2+R^2} + \right.$

$$\left. + \frac{\eta\left\{\dfrac{\partial\Lambda^\star}{\partial x}(x,\eta) - \dfrac{\partial\Lambda_E^\star}{\partial x}(x,R)\right\} + RR'\{\lambda^\star(x,\eta) - \lambda_E^\star(x,R)\} - R\dfrac{\partial\Lambda_v^\star}{\partial x}(x,R) - \eta R'\lambda_v^\star(x,R)}{\eta^2-R^2}\right]d\eta.$$

The first integral in $H(x)$ involves, in general, terms in $\log[(\sigma^2+R^2)/2R^2]$ and in $\tan^{-1}[(\sigma-R)/(\sigma+R)]$; the second integral has already appeared in the function $G(x)$ (equation (29)).

†The same result may also be obtained by replacing y^2 by $-R^2$ in equation (15); this is permissible because ζ occurs in equation (14) only as ζ^2, which is real in both cases. Such a procedure is not possible for a general position on the fuselage, when the modulus in equation (14) must be evaluated first and then differentiated with respect to x.

In the case of wings with *rhombic cross sections* (*cf.* Section 3.2), it is found that

$$H(x)=8\,(Rz_0''-z_0R'')\tan^{-1}\left(\frac{\sigma-R}{\sigma+R}\right)+2\left\{(R^2)''\,\frac{z_0}{\sigma}-R^2\left(\frac{z_0}{\sigma}\right)''\right\}\log\left(\frac{\sigma^2+R^2}{2R^2}\right),$$

$$\text{so that } \Delta C_p=-\frac{2}{\pi}\left[(z_0\sigma)''\log\left(\frac{\sigma^2+R^2}{\sigma^2-R^2}\right)+\left(\frac{R^2z_0}{\sigma}\right)''\log\left(\frac{2R^2}{\sigma^2-R^2}\right)-\right.$$
$$-2\,(Rz_0)''\log\tfrac{1}{2}\left(\frac{\sigma+R}{\sigma-R}\right)+\left\{(R^2)''\,\frac{z_0}{\sigma}-R^2\left(\frac{z_0}{\sigma}\right)''\right\}\log\left(\frac{\sigma^2+R^2}{2R^2}\right)+$$
$$\left.+4\,(Rz_0''-z_0R'')\tan^{-1}\left(\frac{\sigma-R}{\sigma+R}\right)\right] \qquad (55)$$

For wings with *parabolic cross sections* (*cf.* Section 3.3), the corresponding expressions are

$$H(x)=8\left[\tfrac{1}{3}R^3\left(\frac{z_0}{\sigma^2}\right)''-\tfrac{1}{3}\frac{z_0}{\sigma^2}(R^3)''+Rz_0''-z_0R''\right]\tan^{-1}\left(\frac{\sigma-R}{\sigma+R}\right)-$$
$$-\tfrac{16}{3}\left(\frac{\sigma-R}{R}\right)\frac{d}{dx}\left\{R^3\left(\frac{z_0}{\sigma^2}\right)'\right\},$$

$$\text{and } \Delta C_p=-\frac{2}{\pi}\left[\tfrac{4}{3}(z_0\sigma)''\log\left(\frac{\sigma^2+R^2}{\sigma^2-R^2}\right)-2\,\frac{d^2}{dx^2}\left\{z_0R\left(1-\tfrac{1}{3}\frac{R^2}{\sigma^2}\right)\right\}\log\tfrac{1}{2}\left(\frac{\sigma+R}{\sigma-R}\right)+\right.$$
$$+4\left\{\tfrac{1}{3}R^3\left(\frac{z_0}{\sigma^2}\right)''-\tfrac{1}{3}\frac{z_0}{\sigma^2}(R^3)''+Rz_0''-z_0R''\right\}\tan^{-1}\left(\frac{\sigma-R}{\sigma+R}\right)-$$
$$\left.-\tfrac{8}{3}\left(\frac{\sigma-R}{R}\right)\frac{d}{dx}\left\{R^3\left(\frac{z_0}{\sigma^2}\right)'\right\}\right]. \qquad (56)$$

5. Approximations Valid when R/σ is Small

In many cases of practical interest the fuselage radius will be fairly small compared with the local semi-span over much of the length; we therefore proceed in this section to examine what simplifications can be achieved in the theory of Sections 3 and 4 by assuming that $R_1=R/\sigma$ is small.

Considering first the pressure in the wing-fuselage junction (Section 3), we notice that the principal term (the first) in $C_{pW}|_J$ is of order $(z_0\sigma)''\log[\beta\sigma/(2x)]$. If we neglect relative to this all terms of order $R_1^2\log R$, or lower, we obtain

$$C_{pW}|_J\simeq-\frac{1}{\pi}\left[S_W''(x)\log\left(\frac{\beta\sigma}{2x}\right)+S_{WF}''(x)\log\left(\frac{1}{4R_1}\right)+F_W(x)+G(x)\right], \qquad (57)$$

since S_{WF}'' is of order R_1 and $S_{WF}{}^{\star\prime\prime}$ of order R_1^2, relative to S_W''.

If we now examine the series (37) for $G(x)$, we see that

$$\left.\begin{aligned} G_0 &= \left[G_0^{(0)} + 4R\,\frac{d}{dx}\left\{\frac{(z_0R)'}{R}\right\}\right][1+O(R_1^2)] \\ G_1 &= G_1^{(0)}\{1+O(R_1^2\log R_1)\} \\ \text{and}\quad G_n &= G_n^{(0)}\{1+O(R_1^2)\} \quad (n\geqslant 2) \end{aligned}\right\} \quad . \quad . \quad . \quad (58)$$

where $$G_n^{(0)} = -\frac{4\sigma^{n+1}}{(n+1)^2}\,a_n''$$

is the value of G_n when $R\equiv 0$. Now, in the notation of equations (30) and (31),

$$S_W = S_{WG} - S_{WF},$$

and if we define
$$F_{WF} = \int_0^x \frac{S_{WF}''(x) - S_{WF}''(\xi)}{x-\xi}\,d\xi \quad . \quad . \quad (59)$$

and
$$F_{WG} = \int_0^x \frac{S_{WG}''(x) - S_{WG}''(\xi)}{x-\xi}\,d\xi, \quad . \quad . \quad (60)$$

then clearly
$$F_W = F_{WG} - F_{WF}. \quad . \quad . \quad . \quad . \quad . \quad (61)$$

If we consider the gross wing alone (continued through the body), and denote the value of the pressure coefficient at the centre section ($y=0$) of this wing by $C_{pW}^{(0)}$, then

$$C_{pW}^{(0)} = -\frac{1}{\pi}\left[S_{WG}''(x)\log\left(\frac{\beta\sigma}{2x}\right) + F_{WG}(x) + G^{(0)}(x)\right], \quad . \quad (62)$$

and we can therefore write equation (57), making use of equations (58) and (61), in the form

$$C_{pW}|_J = C_{pW}^{(0)} - C_{pI}, \quad . \quad . \quad . \quad . \quad . \quad (63)$$

where
$$C_{pI} \simeq -\frac{1}{\pi}\left[S_{WF}''(x)\log\left(\frac{2\beta R}{x}\right) + F_{WF} - 4R\,\frac{d}{dx}\left\{\frac{(z_0R)'}{R}\right\}\right]. \quad . \quad (64)$$

To the same order of approximation S_{WF}, which is the cross-sectional area of that part of the gross wing blanketed by the fuselage, may be taken to be $4z_0R$, so that the interference pressure (equation (64)) may also be written in the form

$$C_{pI} \simeq -\frac{1}{\pi}\left[S_{WF}''(x)\log\left(\frac{2\beta R}{x}\right) + F_{WF} - R\,\frac{d}{dx}\left(\frac{S_{WF}'}{R}\right)\right] \quad . \quad . \quad (64a)$$

The final approximate expression for the pressure at the wing-fuselage junction is thus

$$C_p|_J \simeq C_{pF}|_J + C_{pW}^{(0)} - C_{pI}, \quad . \quad . \quad . \quad . \quad (65)$$

with the three terms on the right-hand side given by equations (35), (62) and (64) respectively. It will be noticed that the equation for the interference pressure has a certain similarity to the equation for the pressure due to a body of revolution whose area distribution is equal to S_{WF}; this might perhaps have been expected, but the two expressions are not identical and the similarity can not therefore be exploited further.

A similar simplification can be achieved by making the same approximation with regard to the pressure distribution along the top of the fuselage (Section 4). Neglecting terms of order $R^2 \log R$ or smaller in equations (55) and (56), we obtain in both cases

$$\Delta C_p = C_p \text{ (top)} - C_p \text{ (junction)} \simeq -\frac{1}{\pi} S_{WF}'' \log 2 - 2 (R z_0'' - z_0 R''), \quad . \quad (66)$$

with $S_{WF} \simeq 4Rz_0$ as before.

This result is also true, in fact, for wings of general cross-sectional shape.

The approximate equations (64) and (66) are valid for a wing of quite general thickness distribution, and thus provide a rapid method of estimating the pressure at the top and junction of any wing-fuselage combination of this type once the root pressure distribution for the gross wing alone is known (*see* Refs. 5 and 7).

6. Numerical Example

6.1. General

To conclude the discussion of pressure distributions, we now consider the application of the preceding results to a particular example which may be of some practical interest. This consists of a wing of delta plan form, with rhombic cross sections, having a parabolic arc root section, combined with a fuselage which is also of parabolic section but may have a blunt base.

Thus we take $\sigma(x) = sx$ . . . . . (67)

$$z_0(x) = 2\tau x(1-x) \quad . \quad . \quad . \quad . \quad . \quad . \quad . \quad (68)$$

and $R(x) = 2\varepsilon \frac{x}{a}\left(1 - \frac{x}{a}\right)$ (with $a \geqslant 1$), . . . (69)

so that the wing is of aspect ratio $4s$ and root thickness/chord ratio τ, while the fuselage is of fineness ratio ε and has a blunt base (if $a > 1$) of radius $R_B = (2\varepsilon/a^2)(a-1)$.

The fuselage area distribution is

$$S_F(x) = \frac{4\pi\varepsilon^2}{a^4} x^2 (a-x)^2, \quad . \quad . \quad . \quad . \quad . \quad . \quad (70)$$

and its volume is $$V_F = \frac{2\pi\varepsilon^2}{15a^4} (10a^2 - 15a + 6). \quad . \quad . \quad . \quad . \quad (71)$$

The exposed wing area distribution is

$$S_W(x) = 4\tau s x^2 (1-x)(1-R_1^2), \quad . \quad . \quad . \quad . \quad (72)$$

where $$R_1 = \frac{R}{sx} = \frac{2\varepsilon}{sa^2}(a-x).$$

It is convenient at this stage to introduce the parameter

$$\lambda = \frac{\varepsilon}{sa}; \quad . \quad . \quad . \quad . \quad . \quad . \quad (73)$$

2λ represents the ratio of the fuselage slope at the apex $x=0$ to that of the wing plan form (thus when $\lambda = \frac{1}{2}$ the wing and fuselage merge at the apex).

Then $$R_1 = 2\lambda\left(1 - \frac{x}{a}\right),$$

so that $$\frac{S_W''(x)}{4\tau s} = 2(1-2\lambda)^2 + 6(1-2\lambda)\left(-1 + 2\lambda + \frac{4\lambda}{a}\right)x + \\ + \frac{48\lambda}{a}\left(-1 + 2\lambda + \frac{\lambda}{a}\right)x^2 - \frac{80\lambda^2}{a^2}x^3 \quad . \quad (74)$$

and, from equation (17),

$$\frac{F_W(x)}{4\tau s} = 6(1-2\lambda)\left(-1 + 2\lambda + \frac{4\lambda}{a}\right)x + \frac{72\lambda}{a}\left(-1 + 2\lambda + \frac{\lambda}{a}\right)x^2 - \frac{440}{3}\frac{\lambda^2}{a^2}x^3. \quad . \quad (75)$$

The wing volume is $$V_W = \frac{\tau s}{15}\left[5(1-2\lambda)^2 + \frac{12\lambda}{a}(1-2\lambda) + \frac{8\lambda^2}{a^2}\right] \quad . \quad . \quad . \quad (76)$$

6.2. Junction Pressure Distribution

Equation (44) now becomes

$$\frac{C_{pW}|_J}{4\tau s} = -\frac{1}{\pi}\left[S_W^{\star\prime\prime}(x)\log\{\tfrac{1}{2}\beta s(1-R_1^2)\} - 8\lambda\left\{1 - 3x\left(1 + \frac{1}{a}\right) + \frac{6x^2}{a}\right\}\log\left\{\frac{4R_1}{(1+R_1)^2}\right\} - \right. \\ \left. - 8\lambda^2 x\left(1 - \frac{x}{a}\right)\left(1 - \frac{2x}{a}\right)\log\left(\frac{1}{R_1}\right) + F_W^{\star}(x) + G^{\star}(x)\right], \quad (77)$$

where
$$G^{\star}(x)=4x(1-R_1)\left\{1-R_1+\frac{\lambda(a-1)}{a-x}\right\}; \quad . \quad . \quad (78)$$

$$S_w^{\star\prime\prime}(x)=\frac{S_w''(x)}{4\tau s}$$

and
$$F_w^{\star}(x)=\frac{F_w(x)}{4\tau s}$$

are given by equations (74) and (75).

The contribution due to the fuselage is

$$C_{pF}|_J=-\frac{4\varepsilon^2}{a^2}\left[2\left(1-\frac{6x}{a}+\frac{6x^2}{a^2}\right)\log\left\{\frac{\beta\varepsilon}{a}\left(1-\frac{x}{a}\right)\right\}+1-\frac{16x}{a}+\frac{22x^2}{a^2}\right]; \quad (79)$$

this can be written for comparison with equation (77) in the form

$$\frac{C_{pF}|_J}{4\tau s}=-\frac{\varepsilon^2}{\tau s a^2}\left[2\left(1-\frac{6x}{a}+\frac{6x^2}{a^2}\right)\log\left\{\lambda\beta s\left(1-\frac{x}{a}\right)\right\}+1-\frac{16x}{a}+\frac{22x^2}{a^2}\right] \quad . \quad (79a)$$

For a given value of a (that is for a fuselage with a given ratio of base area to maximum area), the value of $C_{pW}/(\tau s)$ depends only on the parameter λ, which is proportional to the ratio of the maximum fuselage radius to the wing span, and on the wing slenderness parameter βs. The fuselage contribution C_{pF} depends similarly on the fineness ratio ε and on β; the ratio of the fuselage contribution to the wing (plus interference) contribution is thus proportional to the ratio $\varepsilon^2/(\tau s)$, or to the ratio of the fuselage volume to the wing volume.

To provide a practical illustration of the foregoing example, the following cases have been computed and the results are shown in Figs. 2 to 7:—

(*a*) $\lambda=\frac{1}{2}$: $a=1{\cdot}0$ (Fig. 2), $1{\cdot}2$ (Fig. 3) and $1{\cdot}4$ (Fig. 4)

(*b*) $\lambda=\frac{1}{4}$: $a=1{\cdot}0$ (Fig. 5), $1{\cdot}2$ (Fig. 6) and $1{\cdot}4$ (Fig. 7).

In each case the relative size of the wing and fuselage has been chosen so that $\varepsilon^2/(\tau s a^2)=2\lambda$, which is equivalent to $\tau/s=\frac{1}{2}\lambda$. Thus typical values of τ, s and ε would be

(*a*) $\lambda=\frac{1}{2}$: $\tau=0{\cdot}05$, $s=0{\cdot}2$, $\varepsilon/a=0{\cdot}1$

(*b*) $\lambda=\frac{1}{4}$: $\tau=0{\cdot}05$, $s=0{\cdot}4$, $\varepsilon/a=0{\cdot}1$.

The corresponding values of the ratio (fuselage volume)/(exposed wing volume) are:—

	$a=1{\cdot}0$	$1{\cdot}2$	$1{\cdot}4$
$\lambda=\frac{1}{2}$	3·142	7·540	14·450
$\lambda=\frac{1}{4}$	0·967	1·839	2·861

The fuselage area distribution is

$$S_F(x) = \frac{4\pi\varepsilon^2}{a^4} x^2 (a-x)^2, \quad . \quad . \quad . \quad . \quad . \quad (70)$$

and its volume is $$V_F = \frac{2\pi\varepsilon^2}{15a^4}(10a^2 - 15a + 6). \quad . \quad . \quad . \quad . \quad (71)$$

The exposed wing area distribution is

$$S_W(x) = 4\tau s x^2 (1-x)(1-R_1^2), \quad . \quad . \quad . \quad . \quad (72)$$

where $$R_1 = \frac{R}{sx} = \frac{2\varepsilon}{sa^2}(a-x).$$

It is convenient at this stage to introduce the parameter

$$\lambda = \frac{\varepsilon}{sa}; \quad . \quad . \quad . \quad . \quad . \quad . \quad (73)$$

2λ represents the ratio of the fuselage slope at the apex $x=0$ to that of the wing plan form (thus when $\lambda = \frac{1}{2}$ the wing and fuselage merge at the apex).

Then $$R_1 = 2\lambda\left(1 - \frac{x}{a}\right),$$

so that $$\frac{S_W''(x)}{4\tau s} = 2(1-2\lambda)^2 + 6(1-2\lambda)\left(-1 + 2\lambda + \frac{4\lambda}{a}\right)x +$$

$$+ \frac{48\lambda}{a}\left(-1 + 2\lambda + \frac{\lambda}{a}\right)x^2 - \frac{80\lambda^2}{a^2}x^3 \quad . \quad (74)$$

and, from equation (17),

$$\frac{F_W(x)}{4\tau s} = 6(1-2\lambda)\left(-1 + 2\lambda + \frac{4\lambda}{a}\right)x + \frac{72\lambda}{a}\left(-1 + 2\lambda + \frac{\lambda}{a}\right)x^2 - \frac{440}{3}\frac{\lambda^2}{a^2}x^3. \quad . \quad (75)$$

The wing volume is $$V_W = \frac{\tau s}{15}\left[5(1-2\lambda)^2 + \frac{12\lambda}{a}(1-2\lambda) + \frac{8\lambda^2}{a^2}\right] \quad . \quad . \quad . \quad (76)$$

6.2. Junction Pressure Distribution

Equation (44) now becomes

$$\frac{C_{pW}|_J}{4\tau s} = -\frac{1}{\pi}\left[S_W^{\star\prime\prime}(x)\log\{\tfrac{1}{2}\beta s(1-R_1^2)\} - 8\lambda\left\{1 - 3x\left(1 + \frac{1}{a}\right) + \frac{6x^2}{a}\right\}\log\left\{\frac{4R_1}{(1+R_1)^2}\right\} -\right.$$

$$\left. - 8\lambda^2 x\left(1 - \frac{x}{a}\right)\left(1 - \frac{2x}{a}\right)\log\left(\frac{1}{R_1}\right) + F_W^{\star}(x) + G^{\star}(x)\right], \quad (77)$$

where
$$G^{\star}(x)=4x(1-R_1)\left\{1-R_1+\frac{\lambda(a-1)}{a-x}\right\}; \quad . \quad . \quad (78)$$

$$S_w{}^{\star\prime\prime}(x)=\frac{S_w{}^{\prime\prime}(x)}{4\tau s}$$

and
$$F_w{}^{\star}(x)=\frac{F_w(x)}{4\tau s}$$

are given by equations (74) and (75).

The contribution due to the fuselage is

$$C_{pF}|_J=-\frac{4\varepsilon^2}{a^2}\left[2\left(1-\frac{6x}{a}+\frac{6x^2}{a^2}\right)\log\left\{\frac{\beta\varepsilon}{a}\left(1-\frac{x}{a}\right)\right\}+1-\frac{16x}{a}+\frac{22x^2}{a^2}\right]; \quad (79)$$

this can be written for comparison with equation (77) in the form

$$\frac{C_{pF}|_J}{4\tau s}=-\frac{\varepsilon^2}{\tau s a^2}\left[2\left(1-\frac{6x}{a}+\frac{6x^2}{a^2}\right)\log\left\{\lambda\beta s\left(1-\frac{x}{a}\right)\right\}+1-\frac{16x}{a}+\frac{22x^2}{a^2}\right] \quad . \quad (79a)$$

For a given value of a (that is for a fuselage with a given ratio of base area to maximum area), the value of $C_{pW}/(\tau s)$ depends only on the parameter λ, which is proportional to the ratio of the maximum fuselage radius to the wing span, and on the wing slenderness parameter βs. The fuselage contribution C_{pF} depends similarly on the fineness ratio ε and on β; the ratio of the fuselage contribution to the wing (plus interference) contribution is thus proportional to the ratio $\varepsilon^2/(\tau s)$, or to the ratio of the fuselage volume to the wing volume.

To provide a practical illustration of the foregoing example, the following cases have been computed and the results are shown in Figs. 2 to 7:—

(*a*) $\lambda=\frac{1}{2}$: $a=1{\cdot}0$ (Fig. 2), $1{\cdot}2$ (Fig. 3) and $1{\cdot}4$ (Fig. 4)

(*b*) $\lambda=\frac{1}{4}$: $a=1{\cdot}0$ (Fig. 5), $1{\cdot}2$ (Fig. 6) and $1{\cdot}4$ (Fig. 7).

In each case the relative size of the wing and fuselage has been chosen so that $\varepsilon^2/(\tau s a^2)=2\lambda$, which is equivalent to $\tau/s=\frac{1}{2}\lambda$. Thus typical values of τ, s and ε would be

(*a*) $\lambda=\frac{1}{2}$: $\tau=0{\cdot}05$, $s=0{\cdot}2$, $\varepsilon/a=0{\cdot}1$

(*b*) $\lambda=\frac{1}{4}$: $\tau=0{\cdot}05$, $s=0{\cdot}4$, $\varepsilon/a=0{\cdot}1$.

The corresponding values of the ratio (fuselage volume)/(exposed wing volume) are:—

	$a=1{\cdot}0$	$1{\cdot}2$	$1{\cdot}4$
$\lambda=\frac{1}{2}$	3·142	7·540	14·450
$\lambda=\frac{1}{4}$	0·967	1·839	2·861

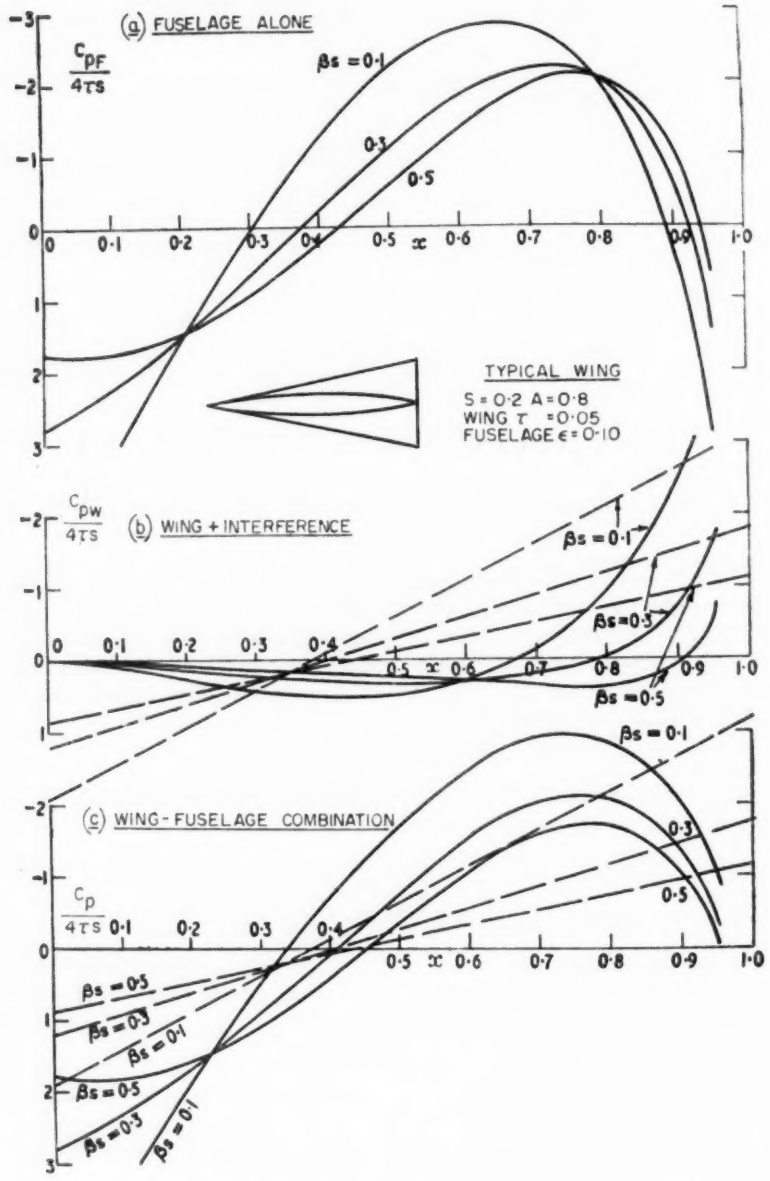

FIGURE 2. Wing-fuselage junction pressure distributions: $\lambda = \frac{1}{4}$, $a = 1{\cdot}0$
—— —— —— Gross wing alone (centre section)

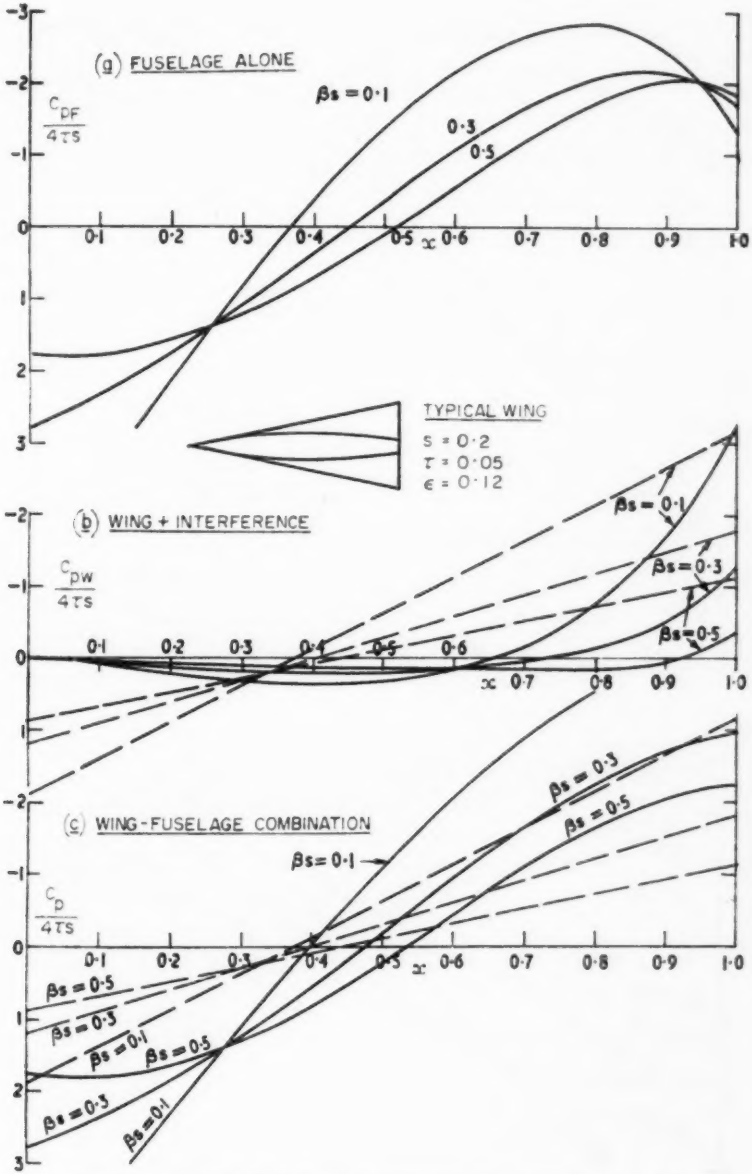

FIGURE 3. Wing-fuselage junction pressure distributions: $\lambda = \frac{1}{4}$, $a = 1{\cdot}2$.
— — — — Gross wing alone (centre section)

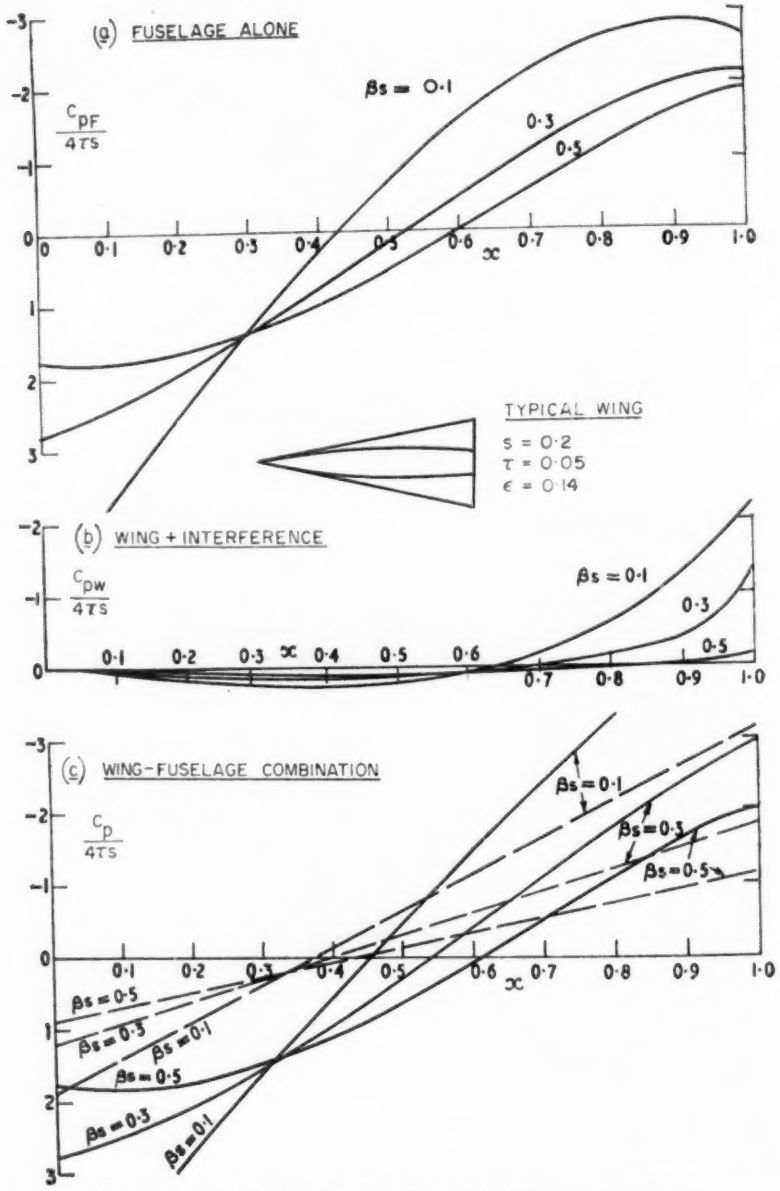

FIGURE 4. Wing-fuselage junction pressure distributions: $\lambda = \frac{1}{2}$, $a = 1{\cdot}4$.
—— —— —— Gross wing alone (centre section)

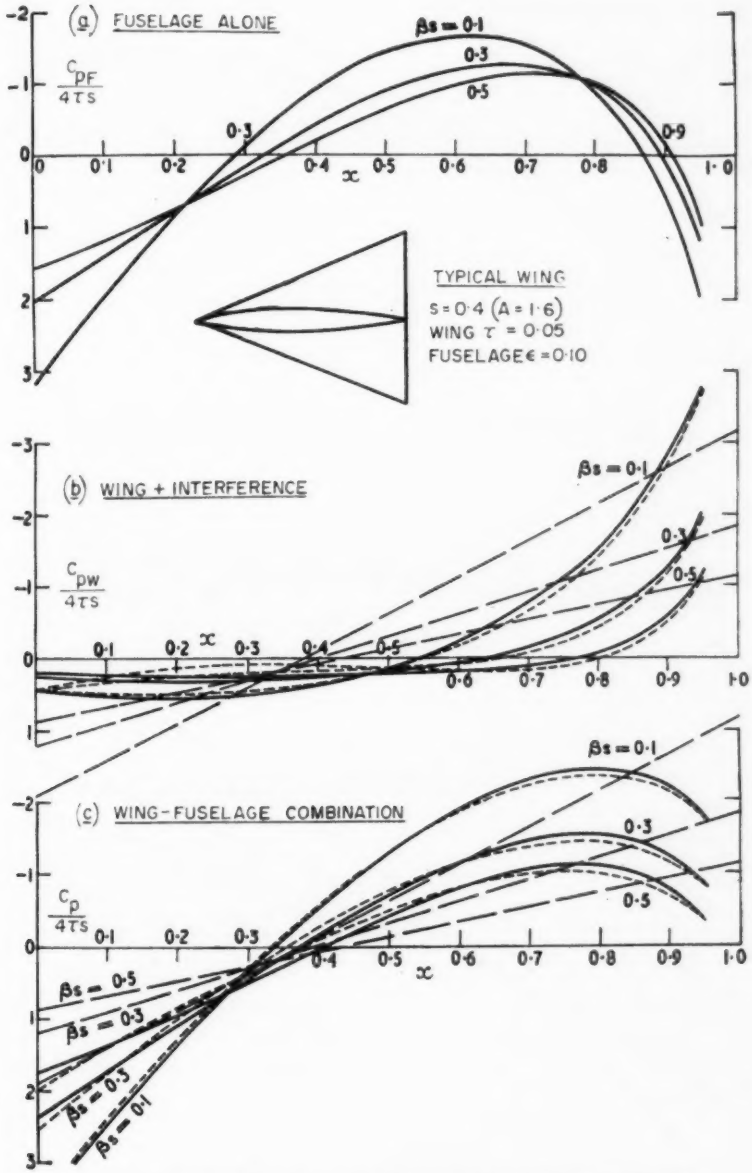

FIGURE 5. Wing-fuselage junction pressure distributions: $\lambda = \frac{1}{4}$, $a = 1{\cdot}0$.

—— —— —— Gross wing alone (centre section)

— — — — — Approximate method (equation (81))

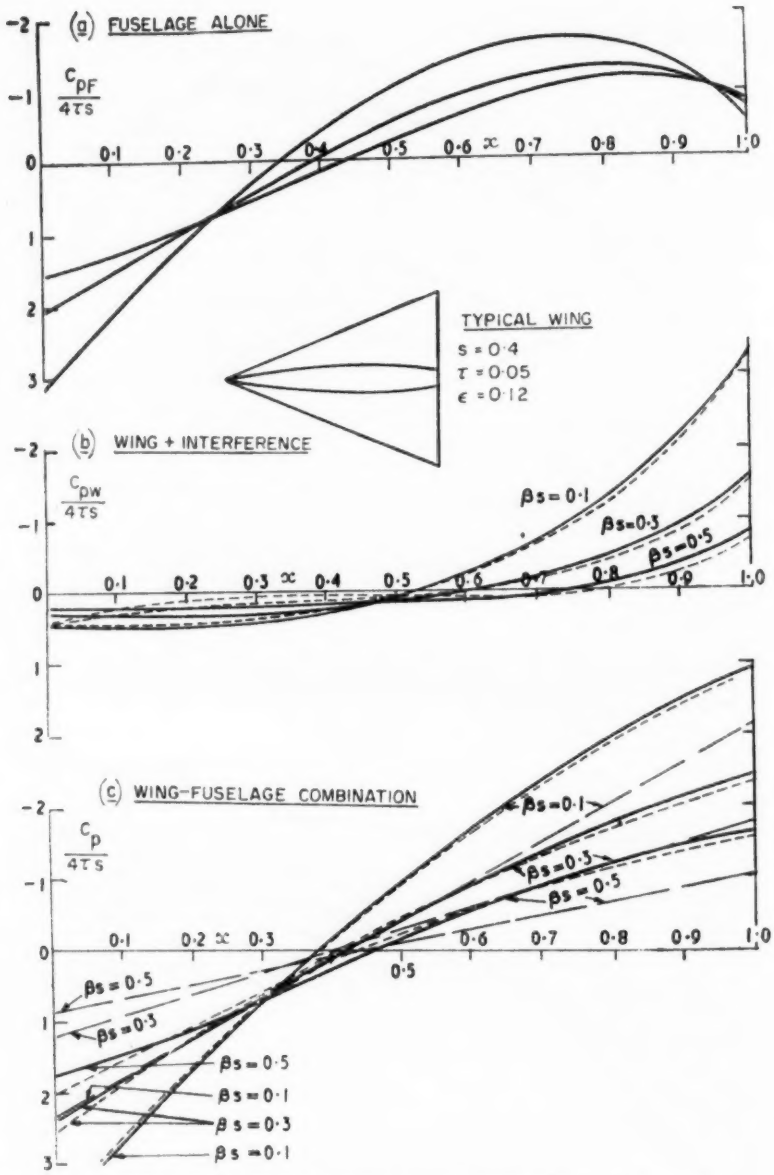

FIGURE 6. Wing-fuselage junction pressure distributions: $\lambda = \frac{1}{4}$, $a = 1{\cdot}2$.
—— —— —— Gross wing alone (centre section)
– – – – – – Approximate method (equation (81))

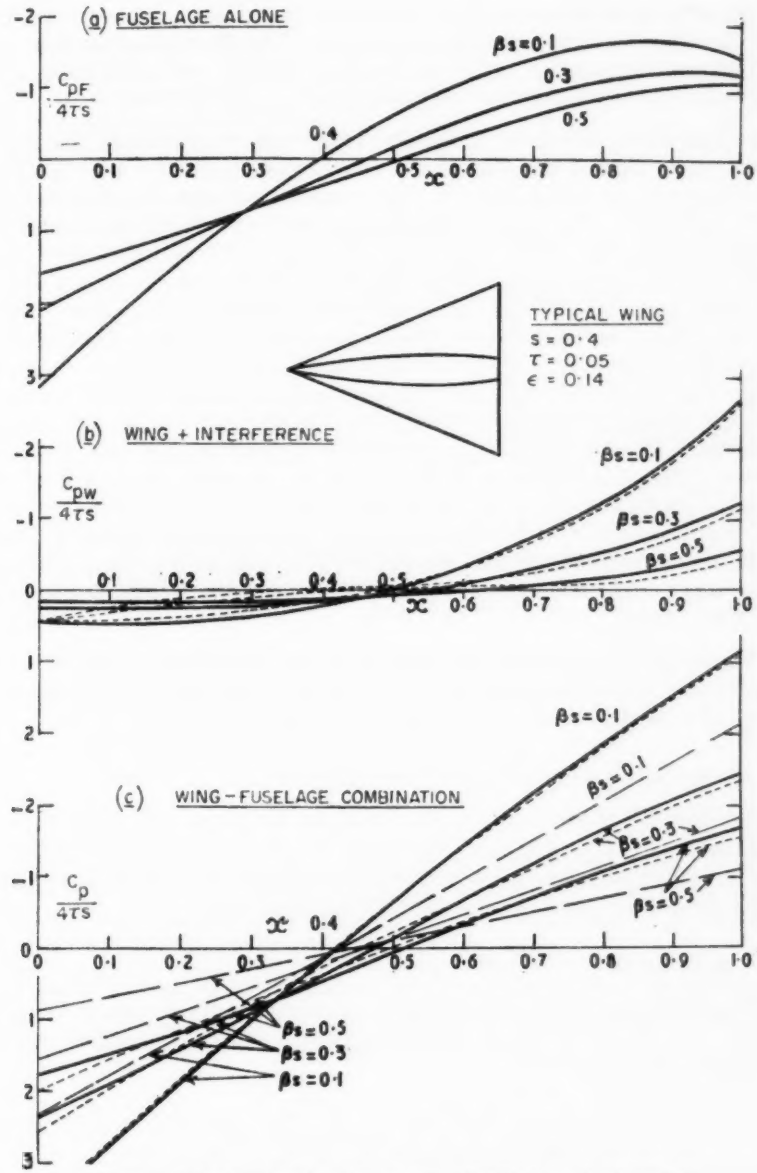

FIGURE 7. Wing-fuselage junction pressure distributions: $\lambda = \frac{1}{2}$, $a = 1{\cdot}4$.

—— —— —— Gross wing alone (centre section)

– – – – – Approximate method (equation (81))

The ratio of the base area of the fuselage to its maximum cross-sectional area takes the values 0, 0·309 and 0·666 respectively. The three examples with $\lambda = \frac{1}{2}$ thus represent combinations with relatively large fuselages and small wings, while those with $\lambda = \frac{1}{4}$ have fuselage and wings more nearly equal in volume.

In spite of the differences in relative fuselage and wing volumes, the general features of the pressure distributions are very similar for the two cases $\lambda = \frac{1}{2}$ and $\lambda = \frac{1}{4}$. The parabolic fuselages are, of course, familiar and were originally investigated by Lighthill[6]. The pressure distributions for the fuselages alone show two principal features: the suction peak aft of the position of maximum radius, which moves rearwards and decreases in magnitude as the Mach number increases, and the rapid recompression following this suction peak, leading for the pointed bodies ($a = 1$) to a logarithmic singularity in the pressure at the rear end.† The additional pressure due to the wing and interference is small compared with that due to the fuselage over the forward half of the wing-fuselage junction, but towards the rear it shows a strong negative gradient which helps to counteract the compression due to the fuselage. For the combinations with pointed fuselages ($a = 1{\cdot}0$), there is still a resultant compressive gradient over the rear 25 per cent, which is more severe for the larger fuselage ($\lambda = \frac{1}{2}$). For the combinations having the largest base area ($a = 1{\cdot}4$), on the other hand, the adverse gradients produced by the fuselage are small and the overall pressure shows a strong favourable (negative) gradient up to the trailing edge. The combinations with $a = 1{\cdot}2$ are naturally intermediate between these two extremes.

The pressure distributions, according to slender-wing theory, along the centre sections of the gross wings alone are also shown for comparison; it is seen that the addition of a fuselage causes a considerable modification in all cases.

6.3. Pressure Along the Top of the Fuselage

Equation (55) of Section 4 has been evaluated for the two cases with a sharp-ended fuselage ($a = 1$, $\lambda = \frac{1}{2}$ and $\frac{1}{4}$). The results are shown in Fig. 8. It will be seen that the pressure variation round the fuselage is everywhere quite small compared with the general pressure level, at least in this particular case.

6.4. The Approximate Method of Section 5

The method has been applied to the present example for the case $\lambda = \frac{1}{4}$, which represents the smaller of the two types of fuselage considered. For this wing the root pressure distribution is[7]

$$\frac{C_{pw}^{(0)}}{4\tau s} = -\frac{2}{\pi}\left[(1-3x)\log\left(\tfrac{1}{2}\beta s - x\right)\right] \quad . \quad . \quad . \quad (80)$$

†Lighthill[6] points out that this singularity is simply a defect of slender-body theory and would not occur in a more complete potential-flow theory or, of course, in practice; but some recompression of this type does occur for pointed bodies, becoming less severe (as indicated by the theory) for bodies with blunt ends.

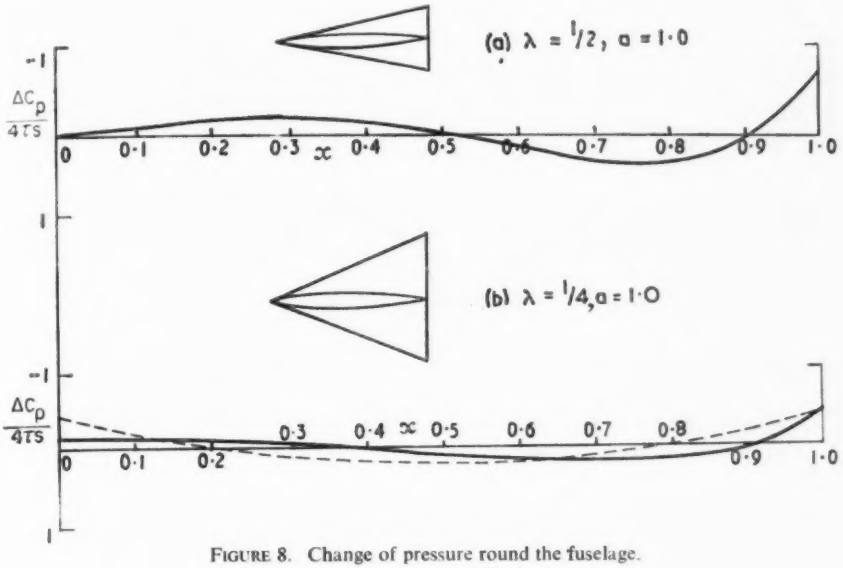

FIGURE 8. Change of pressure round the fuselage.
$\Delta C_p = C_p$ (top) $- C_p$ (junction).
— — — — — Approximate theory.

From equation (64) it is found that, at the junction,

$$\frac{C_{pI}}{4\tau s} = -\frac{8\lambda}{\pi}\left[\left\{1-3x\left(1+\frac{1}{a}\right)+\frac{6x^2}{a}\right\}\log\left[4\beta s\lambda\left(1-\frac{x}{a}\right)\right]-x\left(1+\frac{3}{a}\right)+\right.$$
$$\left.+\frac{7x^2}{a}-\tfrac{1}{2}x\frac{(a-1)}{(a-x)}\right] \qquad (81)$$

The results are plotted in Figs. 5, 6 and 7 for comparison with the more accurate calculations of Section 6.2. It will be seen that the agreement is good over most of the fuselage length and that even near the apex, where R_1 increases to $\frac{1}{2}$, the general shape of the overall pressure distribution is well predicted.

A similar comparison with regard to the change of pressure round the fuselage is made in Fig. 8. In this case ($\lambda = \frac{1}{4}$, $a = 1{\cdot}0$) z_0 is a constant multiple of R so that the last term in equation (66) vanishes and we have simply

$$\Delta C_p \simeq -\frac{1}{\pi} S_{WF}'' \log 2.$$

The agreement with the more accurate equation (55) is again quite satisfactory, although, since the value of ΔC_p given by (55) is itself everywhere small, the *shape* of the curve is not very well predicted by the approximate theory; but the actual numerical difference between the two results never exceeds τs, and this is as good as for the pressure at the wing-fuselage junction.

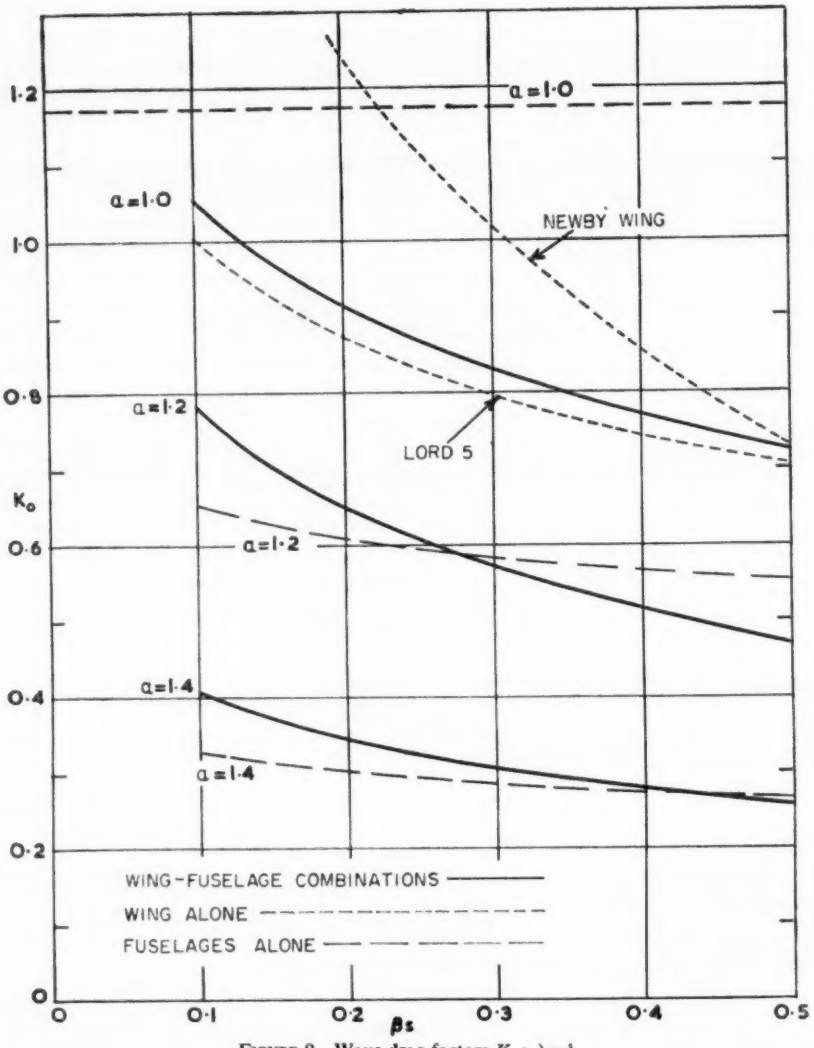

FIGURE 9. Wave drag factors K_0: $\lambda=\frac{1}{2}$.

6.5. Overall Wave Drag

The appropriate extension of the Ward-Lighthill slender-body theory[1] to wing-fuselage combinations of the general type considered in this paper is given in Ref. 4. This method has been applied to the present example, and the results, in the form of the factor (*cf.* Ref. 8)

$$K_0=\frac{\pi}{128}\frac{D}{qV^2}, \quad . \quad . \quad . \quad . \quad . \quad . \quad (82)$$

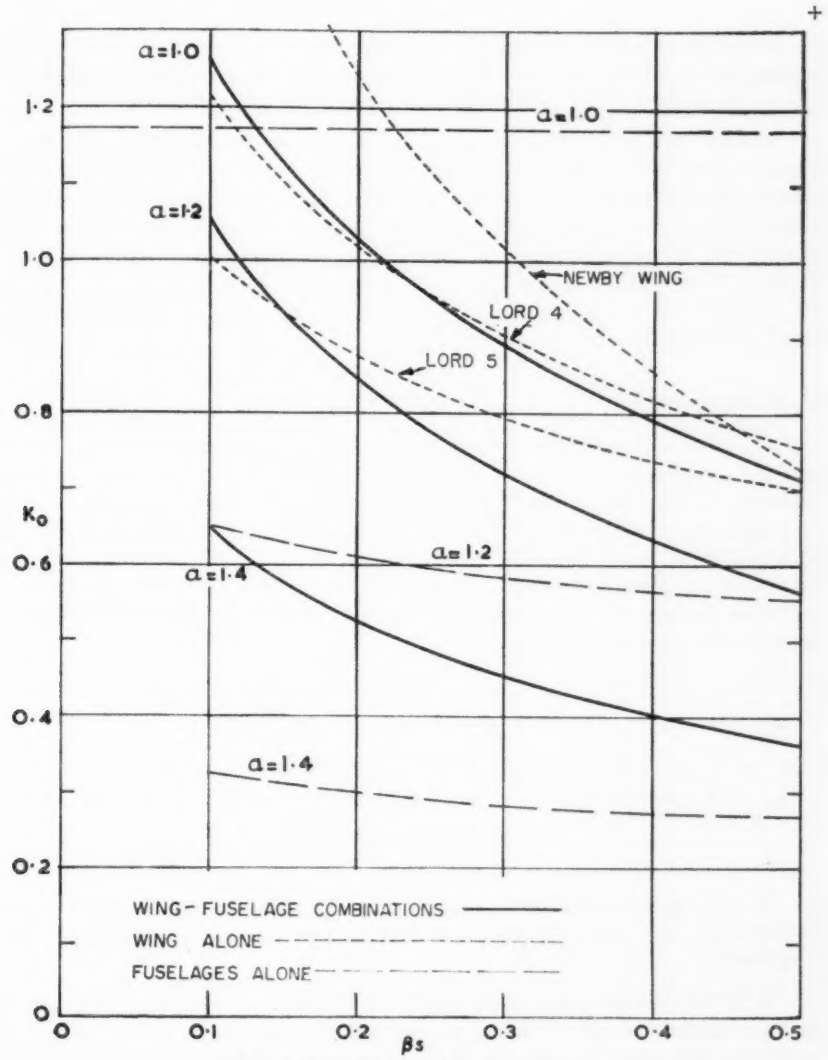

FIGURE 10. Wave drag factors K_0: $\lambda = \frac{1}{4}$.

are shown plotted against βs in Figs. 9 ($\lambda = \frac{1}{2}$) and 10 ($\lambda = \frac{1}{4}$). For comparison we have also included values of K_0 for the three fuselages ($a = 1{\cdot}0$, $1{\cdot}2$ and $1{\cdot}4$) alone, and for some typical wings alone: the gross wing used in this example ("Newby" wing[7]) and Lord's[5] wings 4 and 5. It will be seen that in both cases ($\lambda = \frac{1}{2}$ and $\frac{1}{4}$) the combinations with fuselages pointed at both ends ($a = 1{\cdot}0$) have drag factors considerably lower than for the gross wing alone; for the combination with the larger fuselage ($\lambda = \frac{1}{2}$) the values are close to Lord's wing 5 while with the smaller fuselage ($\lambda = \frac{1}{4}$) they are close to Lord's wing 4. These low values are largely due to

the favourable interference produced by the compression near the rear of the fuselage acting on the backward facing surface of the wing; since this compression will not be so large in practice, the drag results may be over-optimistic.

In both these cases the drag factors are also lower than for the corresponding fuselage alone over a wide range of values of βs, but this is no longer true for combinations with blunt-based fuselages ($a=1{\cdot}2$ and $1{\cdot}4$); the combinations with the larger fuselages ($\lambda=\frac{1}{2}$) have values of K_0 very similar to the fuselages alone, while with the smaller fuselages ($\lambda=\frac{1}{4}$) the values of K_0 are considerably higher. Blunting the base of the fuselage causes in all cases a considerable reduction in K_0; whether any practical use can be made of this depends on the extent to which such a base could be incorporated into the engine design.

7. Conclusions

The method described in the present paper provides a means of calculating the pressure distribution and wave drag in supersonic flow for a wide class of symmetrical wing-fuselage combinations at zero lift. For the method to be strictly applicable, the wings should be "thin" in transverse cross section, both in themselves and relative to the fuselage. It is now known that in practice the first of these conditions can often be relaxed; it remains to be seen how far this is possible with regard to the second. If the wing is *not* thin relative to the fuselage, it might be desirable to replace the equations

$$S_W(x)=4\int_R^\sigma z_W(x,\eta)\,d\eta$$

$$S_{WF}(x)=4\int_0^R z_W(x,\eta)\,d\eta$$

by the appropriate exact expressions, taking into account the curvature of the fuselage inside the wing, although it is unlikely that this would affect the accuracy significantly.

A further generalisation of the method would be to combinations in which the fuselage extends ahead of the wing root leading edge; these would present no additional difficulties provided that the overall area distribution remained sufficiently smooth. It might also be useful in estimating sting interference for all-wing models in which a sting of circular cross section is blended into the wing shape near the trailing edge.

The principal results of the paper can be summarised as follows.

7.1. Overall Pressure Distribution

The pressure coefficient is given by equations (11) to (15) in the form $C_{pF}+C_{pW}$, where C_{pF} is the contribution of the fuselage alone (equation (12)) and C_{pW} is the

contribution of the wing and interference effects (equations (13) and (15)). For a general position on the wing there are two integrals in equation (15) which have not been evaluated explicitly; it is suggested that this could best be done by purely numerical methods.

7.2. Wing-Fuselage Junction Pressures

Along the wing-fuselage junction, C_{pW} is given by equations (36) or (36*a*), which are valid for wings of quite general shape; if the wing thickness distribution is known as a polynomial $\Sigma a_n(x)\eta^n$ in η, the function $G(x)=\Sigma G_n(x)$ can be obtained from equation (37). Explicit formulae for $C_{pW}|_J$ for wings of rhombic or parabolic cross section are given by equations (44) and (50) respectively.

When the ratio R_1 of the fuselage radius to the local semi-span is fairly small, a considerable simplification may be made and the following formula results:—

$$C_p|_J = C_{pF} + C_{pW}^{(0)} - C_{pI}, \qquad . \quad . \quad . \quad . \quad (78)$$

where C_{pF} is the pressure on the fuselage alone (equation (35)), $C_{pW}^{(0)}$ is the pressure along the centre line on the gross wing alone (equation (62)), and C_{pI} is the interference pressure given by

$$C_{pI} \simeq -\frac{1}{\pi}\left[4(z_0R)''\log\left(\frac{2\beta R}{x}\right) + F_{WF} - 4R\frac{d}{dx}\left\{\frac{(z_0R)'}{R}\right\}\right]; \qquad . \quad (64a)$$

this is valid for a wing of general thickness distribution, and will be particularly valuable if the pressure $C_{pW}^{(0)}$ due to the gross wing alone is already known.

7.3. Pressure Along the Top of the Fuselage

The change of pressure round the fuselage, from the wing junction to the top, is given by equation (54) in general; for wings with rhombic or parabolic cross sections this takes the form (55) or (56) respectively. The corresponding approximation when R_1 is small is given by equation (66). In the examples considered in Section 6, this change of pressure was relatively small in all cases.

7.4. Example

A simple example has been considered in Section 6, consisting of a "Newby" wing[7] combined with a parabolic body of revolution (which may have a blunt base). The drag results (Figs. 9 and 10) show favourable interference between the wing and the fuselage; this is due to the compression near the wing trailing edge produced by the fuselage (*see* Figs. 2-7). When the fuselage is pointed at the rear the theoretical pressure distributions have a spurious singularity there which may invalidate the drag results, but when the fuselage is blunt the pressure gradients are favourable over almost the whole of the wing and so could be realised in practice.

ACKNOWLEDGMENTS

The work described was done as part of the research programme of the Aerodynamics Division, National Physical Laboratory, and is published by permission of the Director of the Laboratory.

The computations involved in this paper were made by Mrs. S. M. Bocutt and Miss R. A. Buckthorpe.

REFERENCES

1. LIGHTHILL, M. J. The Wave Drag at Zero Lift of Slender Delta Wings and Similar Configurations. *Journal of Fluid Mechanics*, Vol. 1, p. 337, September 1956.

2. BYRD, P. F. Theoretical Pressure Distributions for Some Slender Wing-Body Combinations at Zero Lift. N.A.C.A. T.N. 3674, April 1956.

3. BREBNER, G. G. A Method for Calculating the Velocity Distribution on a Thin Slender Wing Combined with a Cylindrical Body of Revolution. R.A.E. Technical Note Aero. 2652, December 1959.

4. LOCK, R. C. Theoretical Pressure Distribution and Wave Drag at Zero Lift at Supersonic Speeds for Slender Delta Wings having Fuselages of Circular Cross-Section. A.R.C. 21,973, May 1960.

5. LORD, W. T. and BREBNER, G. G. Supersonic Flow Past Narrow Wings with "Similar" Cross-Sections at Zero Lift. R.A.E. Technical Note Aero. 2509, August 1957.

6. LIGHTHILL, M. J. Supersonic Flow Past Bodies of Revolution. R. & M. 2003, January 1945.

7. WEBER, J. Slender Delta Wings with Sharp Edges at Zero Lift. R.A.E. Technical Note Aero. 2508, A.R.C. 19,549, May 1957.

8. KÜCHEMANN, D. Some Considerations of Aircraft Shapes and Their Aerodynamics for Flight at Supersonic Speeds. *Proceedings of the Second International Congress of the Aeronautical Sciences*, Zürich, September 1960. To be published.

The Axial Decay and Radial Spread of a Supersonic Jet Exhausting into Air at Rest

J. H. FRAUENBERGER* and J. G. FORBISTER†

SUMMARY: The distribution of total pressure, stagnation temperature and gas velocity is determined for the subsonic region of a supersonic jet emerging from a solid propellant rocket motor into air at rest. Measurements of Pitot pressures in the supersonic flow region have shown that the flow follows the axis of an inclined nozzle within the order of accuracy of the measurements. Nozzle cone angle, and probably the expansion ratio, affect the jet distribution significantly.

1. Introduction

Knowledge of the effect of the jet from a rocket motor on remote surfaces such as the control surfaces of a missile, the launcher, the launching aircraft or other structure is often desirable for design purposes. Some firings of a standard solid propellant rocket motor were arranged to provide information for estimating effects of this kind. Total pressures and total temperatures were measured at a number of positions in the jet. Velocities of the gas-air mixture have been computed from these measurements.

Investigations on free subsonic jets (length of core, quantity of entrained air, and decay of velocity) have been made by Kuethe[1] and Wuest[2]. The present investigation into the axial decay and radial spread of a supersonic jet exhausting into still air considers both the early supersonic régime and the later subsonic jet.

NOTATION

a velocity of sound

a' critical velocity of sound

c gas velocity (ft./sec.)

d diameter (in.)

$\gamma = c_p/c_v$, ratio of specific heats

$M^* = c/a'$, Mach number

*Now in Germany
†Atomic Weapons Research Establishment, Aldermaston } Formerly Rocket Propulsion Department, Westcott.

Received December 1960.

$M = c/a$, Mach number

m mass flow rate

P pressure (lb./in.^{2} absolute)

p pressure (lb./in.^{2} gauge)

$P\star$ Pitot pressure (lb./in.^{2} absolute)

$p\star = (P\star - P_A)$, Pitot pressure (lb./in.^{2} gauge)

R gas constant

r radius (in. or ft.)

T temperature (°K)

x distance of point of consideration from nozzle exit (in. or ft.)

Suffixes

G gas

A air

c combustion chamber

0 stagnation value

m gas-air mixture

e nozzle exit

t nozzle throat

2. The Development of the Jet

Before describing and discussing the tests and their results it may be of some interest to consider the development of the gas stream and the use of Pitot tubes for measurements of total pressures in supersonic and subsonic flows from a purely theoretical aspect and to give a general picture of the results.

2.1. Pressure Measurement by a Pitot Tube

On placing a Pitot tube into a jet stream of supersonic velocity c, a compression shock will form ahead of it and a sudden change in pressure, velocity and density of the gas will occur. The measured pressure $P\star$ (pressure after the shock at the stagnation point) is less than the reservoir or total pressure P_0 corresponding to the velocity c. In a subsonic stream the Pitot tube measures the total pressure.

When the total pressure, P_0, of the supersonic flow is known, the Mach number is given by the formula

$$\frac{P\star}{P_0} = M\star^2 \left[\frac{1 - M\star^2 \left(\frac{\gamma - 1}{\gamma + 1} \right)}{1 - \frac{1}{M\star^2} \left(\frac{\gamma - 1}{\gamma + 1} \right)} \right]^{1/(\gamma - 1)}.$$

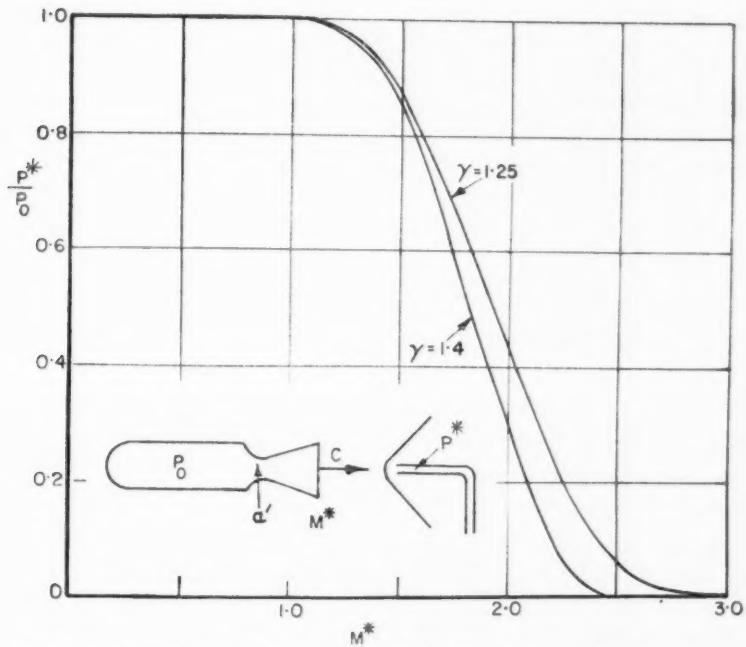

FIGURE 1. Dependence of P^*/P_0 on the Mach number M^* for $\gamma=1{\cdot}25$ and $\gamma=1{\cdot}4$.

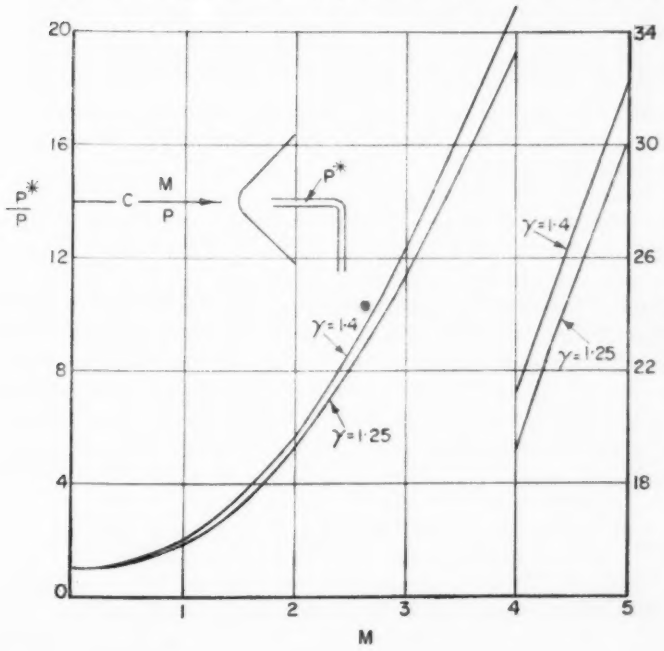

FIGURE 2. Dependence of P^*/P on the Mach number M for $\gamma=1{\cdot}25$ and $\gamma=1{\cdot}4$.

In this formula $M^{\star}=c/a'$ is the Mach number related to the critical velocity of sound a', and γ is the ratio of the specific heats of the gas. This relation is convenient for the early supersonic flow from a nozzle before shocks develop, where the total pressure is equal to the chamber pressure of the rocket motor, that is $P_0=P_c$. Elsewhere in the flow knowledge of the free stream static pressure, P, is required to determine the Mach number, which is then given by

$$\frac{P^{\star}}{P}=\frac{\left(\frac{\gamma+1}{2}M^2\right)^{\gamma/(\gamma-1)}}{\left[\frac{2\gamma}{\gamma+1}M^2-\left(\frac{\gamma-1}{\gamma+1}\right)\right]^{1/(\gamma-1)}} \qquad \text{for } M\geqslant 1$$

$$\frac{P^{\star}}{P}=\left(\frac{\gamma-1}{2}M^2+1\right)^{\gamma/(\gamma-1)} \qquad \text{for } M\leqslant 1$$

where $M=c/a$ is the Mach number related to the local velocity of sound.

The dependence of $M^{\star}$ on $P^{\star}/P_0$ and of M on $P^{\star}/P$ for $\gamma=1{\cdot}25$ and $\gamma=1{\cdot}4$ are shown in Fig. 1 and Fig. 2 respectively.

No other measurement than $P^{\star}$ has been made in the work described in this report, which is mainly concerned with the flow some distance from the nozzle. It is assumed that the static pressure in the subsonic portion of the jet is equal to the atmospheric pressure.

2.2. The Influence of an Under-Expanded Nozzle on the Pressure Distribution in the Jet Stream

For a parallel jet leaving an under-expanded two-dimensional nozzle and expanding into still air, Prandtl[3] gives a wave diagram which is reproduced in Fig. 3. In this simple case the jet, as it flows from the nozzle, expands and contracts between the pressures P_1 and P_3 where

$$\frac{P_1}{P_2}=\frac{P_2}{P_3}\,.$$

P_1 is the initial stream pressure and P_2 is ambient pressure. In practice, this simple cyclic flow would gradually break down owing to the development of shock waves and mixture with the surrounding air.

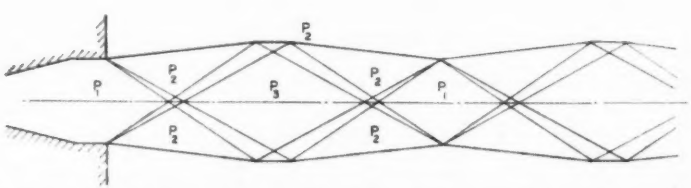

FIGURE 3. Wave diagram of supersonic jet from under-expanded parallel nozzle.

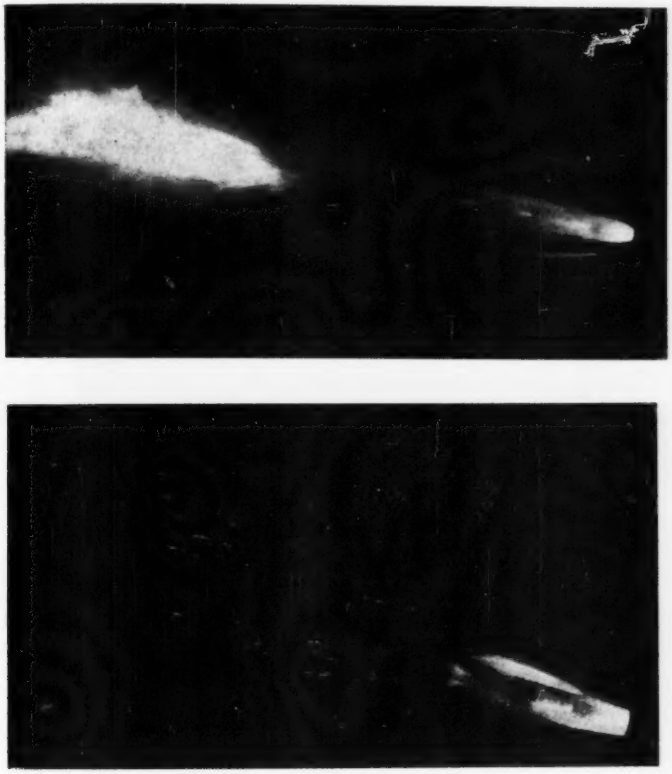

(*a*)

(*b*)

FIGURE 4. Jets from under-expanded (*a*) and fully expanded (*b*) nozzles.

The flow from an under-expanded axially symmetrical parallel or conical nozzle will also have alternate regions of high and low pressure with, however, a more complex pattern of shock waves. A large number of detailed photographs of the air flow from conical nozzles with various expansion ratios and cone angles have been taken by Fraser and Rowe.[4] Photographs taken in the course of the present work are shown in Figs. 4 and 5. Fig. 4(*a*) shows the jet from the under-expanded nozzle and the periodic shock zones of decreasing intensity are clearly visible. Similarly, Fig. 4(*b*) shows the weaker shock zones in the jet from a fully expanded conical nozzle. In this case the shocks are not so strong, but nevertheless do exist, because the flow from the conical nozzle is not parallel and because of viscosity effects.

2.3. GENERAL STRUCTURE OF THE JET

A jet leaving a nozzle at initially supersonic velocity contains along its axis the gradually narrowing core of the original gas stream surrounded by an annular region

(*a*) 38·75 in. from under-expanded nozzle.

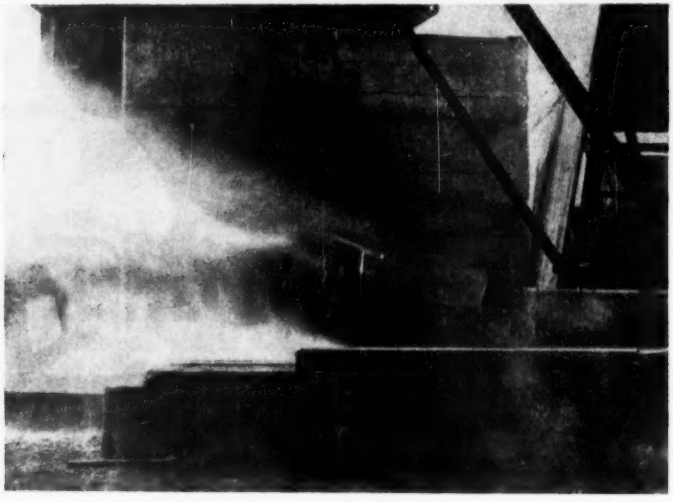

(*b*) 23·5 in. from fully expanded nozzle.

FIGURE 5. Pressure measurement in jets from under-expanded and fully expanded nozzles.

where gas and entrained air have intermixed. As mixing extends across the cross section, temperature and velocity fall and further mixture of air with gas and already entrained air takes place at subsonic speed (Fig. 6).

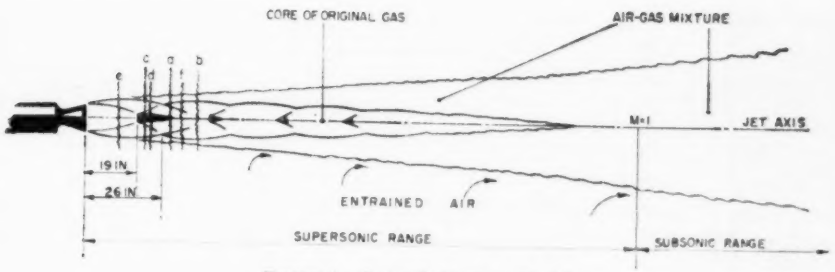

FIGURE 6. General structure of a jet.

It will be assumed for the subsonic portion of the jet that the static pressure equals the ambient pressure. Since, at the beginning of the subsonic portion, M equals unity, the supersonic Pitot tube formula will reduce to

$$\frac{P\star}{P} = \left(\frac{\gamma+1}{2}\right)^{\gamma/(\gamma-1)}.$$

For $\gamma = 1{\cdot}25$ (which is an average value for the products of combustion of our motor), $P\star = 1{\cdot}8P$ and for air, $P\star = 1{\cdot}893P$. Assuming a static pressure of one atmosphere and that the product gases are air rich by the time they reach the subsonic region, the subsonic portion begins with a Pitot pressure of 27·5 lb./in.^{2} absolute.

If the gases leaving the nozzle are fuel rich, afterburning is likely to occur, which may have some influence on the physical properties of the mixture.

3. Test Apparatus

The solid propellant motor used in the present experiments burned for some 2·5 seconds at a chamber pressure p_c of 1,000 to 1,100 lb./in.^{2}, as can be seen in Fig. 7. The mean mass flow rate was 33 lb./sec. Assuming a chamber pressure of 1,030 lb./in.^{2} absolute and a gas temperature of 2,473°K, the exit velocity for isentropic expansion to atmospheric pressure is 7,380 ft./sec. at a gas temperature of 1,055°K. The gas composition is shown in Table I.

Owing to the arrangement of the test bed, and to reduce interference between the jet and the ground, inclined nozzles were used on the motor. Nozzles having inclinations of 15°, 11° and 7·5° were selected from a range of existing types. The 7·5° nozzle restricted the range for the measurements to a distance of some 40 ft. from

TABLE I
GAS COMPOSITION IN MOTOR

Component	H_2O	CO_2	CO	H_2	OH	H	N_2	NO
Percentage by volume	20	8·96	43·39	15·23	0·30	0·12	12·26	0·01

Pressure = 70 atmospheres Temperature = 2473 K

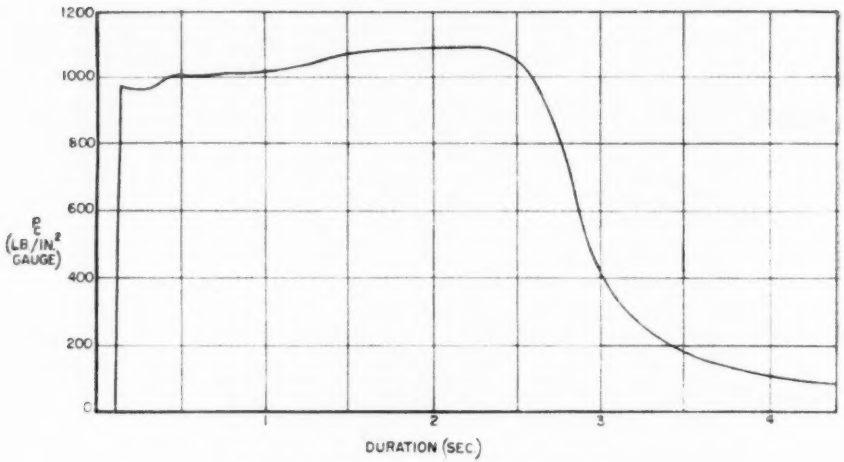

FIGURE 7. Pressure-time record for motor.

the exit plane for reasonably symmetrical entrainment of air, assuming a cone angle for the jet of 20° (Fig. 8). The 15° and 11° nozzles were used for measurements in the supersonic and the earlier part of the subsonic regions respectively.

In most of the experiments nozzles having an included angle of 30° were used, but some tests were made with nozzles of 15° included angle for comparative purposes. All had a throat diameter of 2·55 in. and most had a ratio of exit area to throat area of 4:1, *i.e.* they were under-expanded, giving an exit pressure of 41 lb./in.² absolute. Some nozzles with an expansion ratio of 7·7:1, however, were used; these were almost fully expanded, with an exit pressure of 16·3 lb./in.² absolute. The corresponding Mach numbers M at the nozzle exits were 2·69 and 3·22 respectively.

Pressure measurements in the jet were made by Pitot tubes and two types proved reliable and able to withstand the gas temperatures after some development. One was the water-cooled tube shown in Fig. 9(*a*), consisting of the Pitot tube itself within a larger supporting tube which allowed water to flow down the annular space for cooling purposes. The other consisted of a plate (Fig. 9(*b*)), drilled with 5 or 16 holes according to the size of the jet. These were employed in the supersonic region. In the sonic and subsonic region single tubes, as described but uncooled, were secured at 8 in. intervals on the vertical portion of an instrument carriage (Fig. 9(*c*)) that could be inclined at different angles in accordance with the inclination of the motor nozzle. The single tubes were provided with hemispherical heads of diameter six times the bore of the internal tube; likewise the plate type had a rounded front edge, the plate thickness being six times the bore of the holes. No attempt was made to move these devices during a firing, either radially across or axially along the jet, owing to the short duration of each firing and the slightly changing chamber pressure.

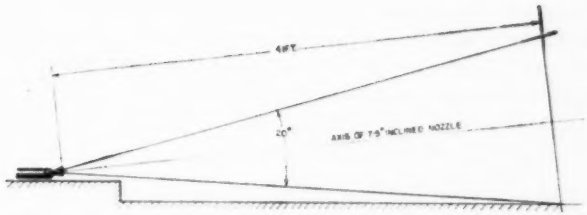

FIGURE 8. Spread of jet from a 7·5° inclined nozzle assuming a jet angle of 20°.

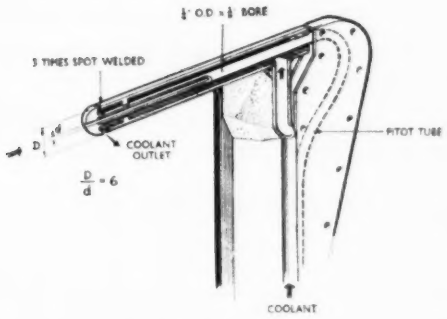

(a.) WATER-COOLED PITOT TUBE

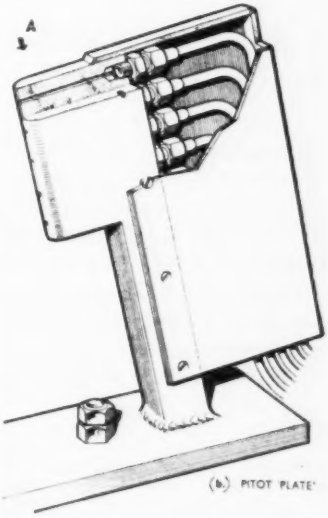

(b.) PITOT PLATE

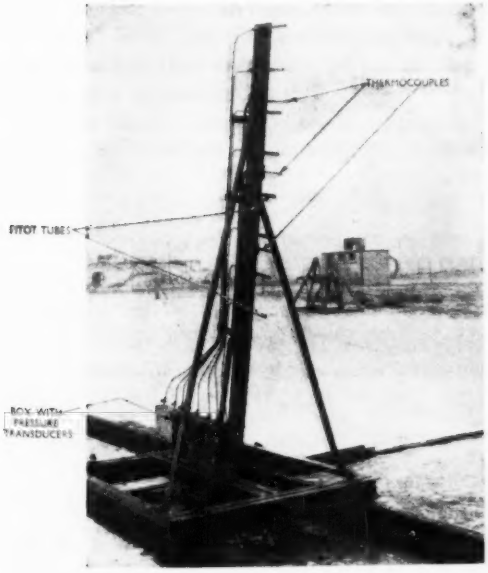

(c.) TEST ARRANGEMENT FOR LONG-DISTANCE MEASUREMENTS

FIGURE 9. Measuring arrangements.

The Pitot tubes were aligned optically with the motor nozzle. A hollow Tufnol body, which contained a weak light source giving a beam through two fine orifices, was machined to fit in the nozzle; by rotating this body the errors of manufacture were eliminated and the jet axis could be located in relation to the Pitot tubes to within $\frac{1}{4}^{\circ}$. The alignment was liable to changes during the run in accordance with the extent of erosion of the nozzle.

The pressures were recorded electronically (Miller recorder) by means of a strain-gauge pressure transducer, consisting of a short elliptical tube with strain gauges bonded to each end of the major and minor axes. On pressurisation of the tube the resistance of one pair of gauges increases and that of the other decreases; the gauges were connected to a Wheatstone bridge to give the maximum sensitivity.

Temperatures were measured by chromel-alumel and platinum-platinum/rhodium thermocouples fixed between the Pitot tubes (Fig. 9(*c*)).

In addition to the instrumentation, cinéfilms of the rocket jet were taken by a high speed camera remotely operated at 24 or 48 frames per second.

4. Measurements in the Region of Supersonic Flow

4.1. General

The values of the Pitot pressures were taken from the records at times corresponding to a pressure of 1,030 lb./in.^{2} absolute (1,015 lb./in.^{2} gauge) in the chamber, because conditions were steady at this pressure for about $\frac{1}{2}$ second. All these pressures are plotted in Figs. 10, 11 and 12 and their values on the axis are given in Table II. In general the results confirm the cyclic nature of the flow in the supersonic region. The variation of Pitot pressure across a section of the jet has two forms which alternate along the jet. In one the Pitot pressure is high at the axis and falls rapidly towards the boundary of the jet. This corresponds to a high static pressure at the axis falling to ambient pressure at the boundary. In the other case the Pitot pressure is low at the axis, rises to a maximum near the boundary and falls

TABLE II

MEASURED PITOT PRESSURES ALONG THE AXES OF JETS EMERGING FROM UNDER-EXPANDED AND ALMOST FULLY EXPANDED NOZZLES

Both Nozzles: included angle = 30°, combustion chamber pressure, P_c = 1030 lb./in.^{2} absolute

Under-Expanded Nozzle

area ratio = 4 : 1, calculated Pitot pressure at nozzle exit, P^* = 373 lb./in.^{2} absolute

Distance from nozzle x (in.)	28·5	38·75	104·5	109·5	157
Pressure p^* (lb./in.^{2} gauge)	180	51 59 52	77·3	75	23

Fully Expanded Nozzle

area ratio = 7·7 : 1, calculated Pitot pressure at nozzle exit, P^* = 210 lb./in.^{2} absolute

Distance from nozzle x (in.)	12	23·5	24	32·5	84·5
Pressure p^* (lb./in.^{2} gauge)	30	297	330	120	125

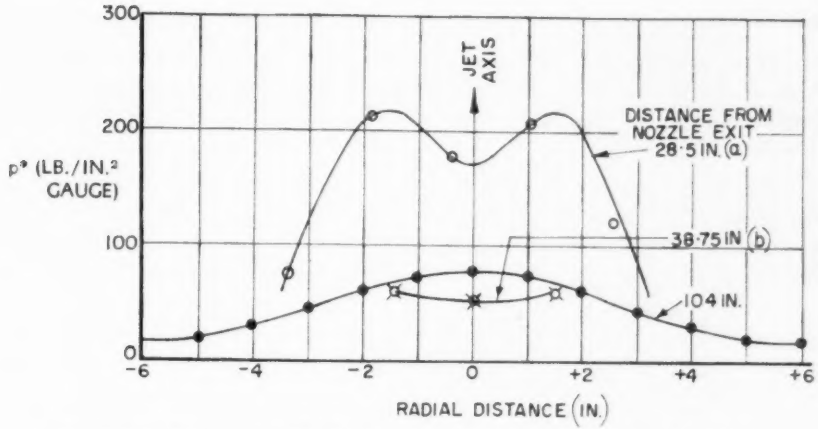

FIGURE 10. Pitot pressure distribution across the jet from under-expanded nozzle.

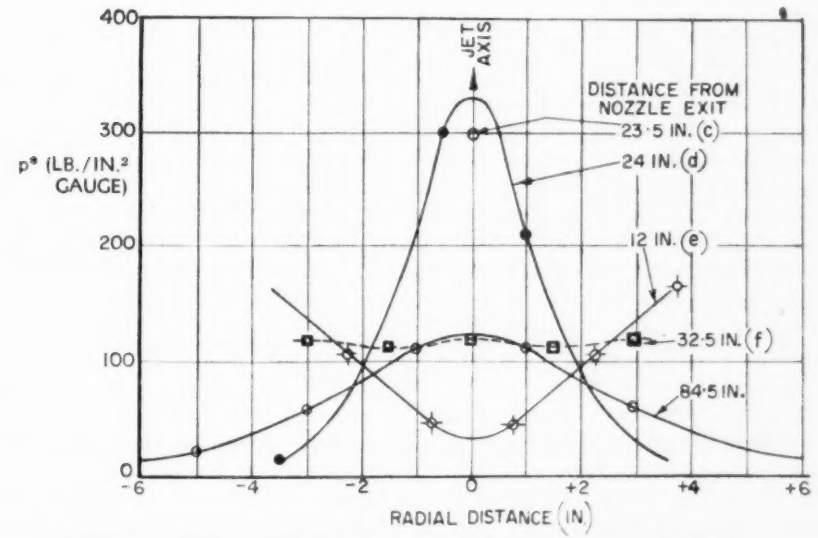

FIGURE 11. Pitot pressure distribution across the jet from fully expanded nozzle.

sharply to ambient pressure. This corresponds to a low static pressure at the axis rising to atmospheric pressure at the boundary. The levels of the Pitot pressure fall from cycle to cycle due to losses caused by shocks and mixing with air.

Referring back to Fig. 4(*a*), the jet from an under-expanded nozzle with a cone angle of 30° may be seen. The expansion of the flow from the nozzle exit is clearly shown and the shock zones correspond to regions of high pressure on the axis of the jet. (Compare Fig. 4(*b*) for the jet from a correctly expanded nozzle.)

4.2. Effect of the Nozzle Exit Cone Angle

Measurements of the pressure distribution across the rocket jet were made at a distance of 104 in., or 41 throat diameters, from the nozzle exit, using under-expanded nozzles with exit cone angles of 30° and 15°. The nozzles were inclined upwards at 15°.

The results are plotted in Fig. 12, where position is measured from the axis of the nozzle. They show that the jet follows the axis of the inclined nozzle to the accuracy of the experiments, say within $\pm\frac{1}{4}°$ ($\pm\frac{1}{2}$ in. at 104 in.). To this accuracy the cone angle of the nozzle does not affect the deflection of the jet.

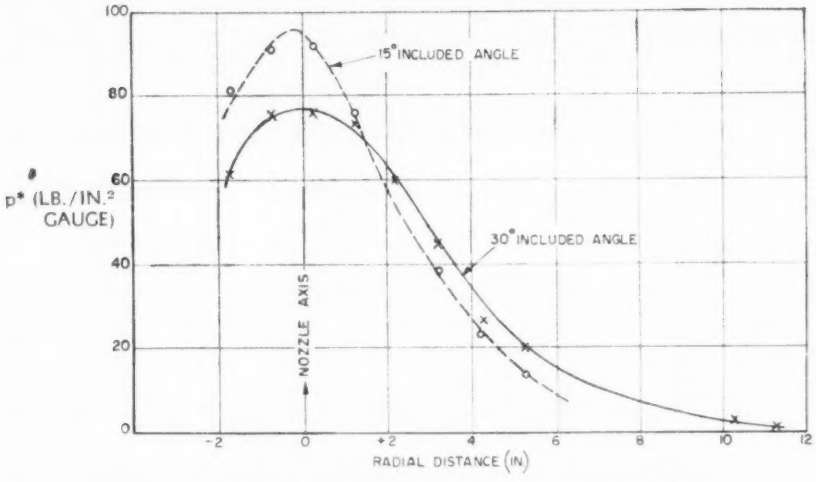

FIGURE 12. Pressure distribution across the jet from under-expanded nozzle with different included angles. Pressure at 104 in. from nozzle.

The smaller nozzle cone angle does, however, result in a more concentrated jet at this distance. The Pitot pressure (gauge) falls to half its peak value on the axis at radial distances of 2·5 in. and 3·5 in. for cone angles of 15° and 30° respectively. Radial distances from the axis may be expressed more conveniently as angular deflections from the axis referred to a centre at the exit of the nozzle. Then the angular deflections, for which the Pitot pressure is one half of its peak value on the axis at 104 in. distance, are $1\frac{1}{2}°$ and 2° for the nozzles with cone angles of 15° and 30° respectively.

4.3. The Flow Near the Nozzle and the Effect of Nozzle Expansion Ratio

For comparative purposes extensions were welded to the expansion cones of some nozzles to give an area ratio of 7·7, which corresponds to about full expansion for a chamber pressure of 1,000 lb./in.² The effect of area expansion ratio will be

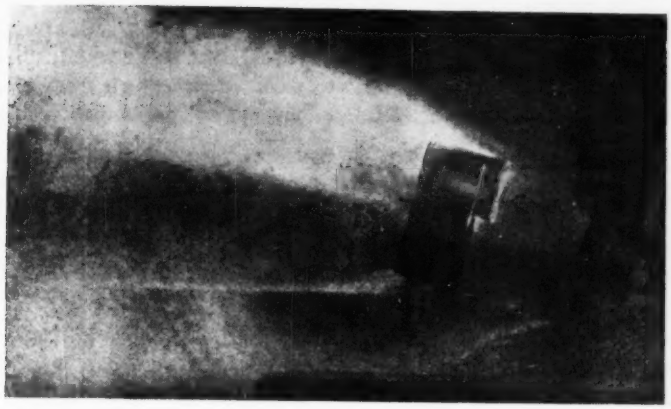

FIGURE 13. Pressure measurement 12 in. from fully expanded nozzle.

greatest in the initial portion of the jet, so measurements of Pitot pressure were made in the early supersonic portion of jets from nozzles having a cone angle of 30° and area ratios of both 4 and 7.7.

The results for the flow from the under-expanded and fully expanded nozzles are given in Figs. 10 and 11 respectively. The letters (*a*) to (*f*) refer to different distances from the nozzle exit; they are also shown in Fig. 6 which presents the general structure of a jet emerging from an under-expanded nozzle. It should be noted that the scale in Fig. 6 is approximately true only for the first and second wave of the jet. The pressure distribution 12 in. from the exit of the fully expanded nozzle (Fig. 13) is shown in Fig. 11. There are no shocks in the flow before this point so that the total temperature and pressure are known. The Pitot pressure, therefore, determines the flow at this section completely. The Pitot pressure of about 30 lb./in.^{2} gauge on the axis at this distance indicates a static pressure of about 2 lb./in.^{2} absolute and this is very close to the value 3 lb./in.^{2} absolute corresponding to conical flow from the nozzle. Based on the static pressure of 2 lb./in.^{2}, the gas velocity is 8,235 ft./sec. ($M=4{\cdot}5$). The flow from the under-expanded nozzle is similar (Fig. 10). The steep and variable pressure gradient across the flow did not permit of accurate determination of the spread of the jet in this region of the flow. The spread from the under-expanded nozzle is, however, comparatively slow, amounting to about ± 12 in. at 104 in. from the nozzle. This is $\pm 6{\cdot}5°$.

5. Measurements in the Region of Subsonic Flow

5.1. General

All tests for measuring pressures and temperatures in the subsonic region were made with under-expanded nozzles of 30° included angle. The beginning of the subsonic portion was estimated from the results to be at a distance of 17 ft. from the nozzle. All Pitot pressures were taken from the records at a time when the chamber

pressure in the motor was 1,030 lb./in.^{2} absolute. As previously stated, cinéfilms at 24 and 48 frames per second were taken of many of the firings. In all cases afterburning occurred intermittently and appeared as a short flame within the range of 13 to 20 ft. from the nozzle. The flame was recorded on a single frame about once every five frames (Fig. 14). The thermocouples did not respond to oscillations of

FIGURE 14. Intermittent afterburning during a firing.

this frequency and the temperature record was smooth, indicating a value between the temperature with afterburning and that without afterburning. The recorded temperature would consequently be heavily weighted towards the value for no afterburning by a factor of at least five.

Assuming no afterburning and no heat losses by conduction and radiation, we have

$$m_G c_{pG} T_G + m_A c_{pA} T_A = (m_G + m_A)\, c_{pm} T_m,$$

where c_p is the specific heat at constant pressure and the suffixes are defined in the Notation. Hence it is possible to correlate a certain mixture ratio and value of γ to a measured stagnation temperature; the gas velocity can be computed using

$$c = \sqrt{\left\{2g \left(\frac{\gamma}{\gamma - 1}\right) R_m T_m \left[1 - \left(\frac{P}{P\star}\right)^{(\gamma-1)/\gamma}\right]\right\}}.$$

5.2. Axial Decay

The pressures, temperatures and velocities along the axis of the jet are shown in Fig. 15. In the non-dimensional scales used for the same gas properties in Fig. 16 any reference to the conditions at the under-expanded nozzle was avoided by taking the throat diameter d_t, throat velocity c_t, motor pressure P_c and motor temperature T_0; the average air temperature was $+10°C$.

5.3. Radial Decay

At each distance from the nozzle indicated in Fig. 15, Pitot pressures and temperatures were measured at a number of distances from the axis of the subsonic jet by Pitot tubes and thermocouples mounted on a stand, illustrated in Fig. 9(*c*). Individual observations have not been reproduced but have been analysed assuming that the radial decay in the subsonic jet is a function of the angle from the axis of the nozzle only and is independent of the distance from the nozzle.

The angular displacements at which the pressure, temperature and velocity fall to 3/4, 1/2, 1/4 and 1/10 of their values on the axis are given in Table III

on p. 146. Complete diagrams of the axial and radial decay of temperature, pressure and velocity are given in Fig. 17.

5.4. Comparison with Another Investigation

While this paper was being prepared a report became available of an American investigation in which an experimental study was conducted of the spreading and axial decay of free supersonic jets exhausting into quiescent air. Supersonic heated-air jets and three types of solid propellant rockets were used, the Mach number M varying between 1·4 and 3·53. In the following comparison only the three solid motors will be considered.

The nozzles were of the convergent-divergent type with included angles of the exit cone of 30° to 60°, exit diameters of 2·0 to 2·59 in. and Mach numbers of 2·82 to 3·53. Although not actually stated, it will be assumed that the nozzles were fully expanded and that the ratio of specific heats was 1·25. The maximum distance at which measurements were made was 26 ft. approximately.

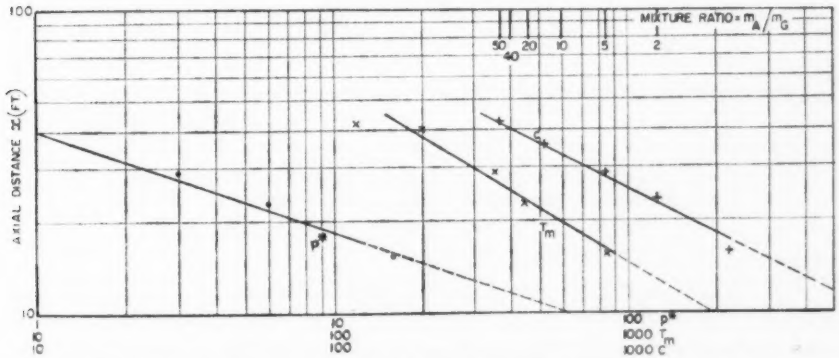

FIGURE 15. Pitot pressure p^* (lb./in.^{2} gauge), stagnation temperature T_m (°C) and velocity c (ft./sec.) along the axis.

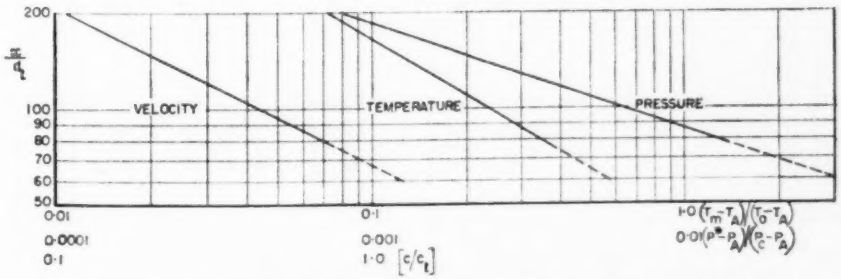

FIGURE 16. Pitot pressure, stagnation temperature and velocity along the axis expressed in non-dimensional ratios.

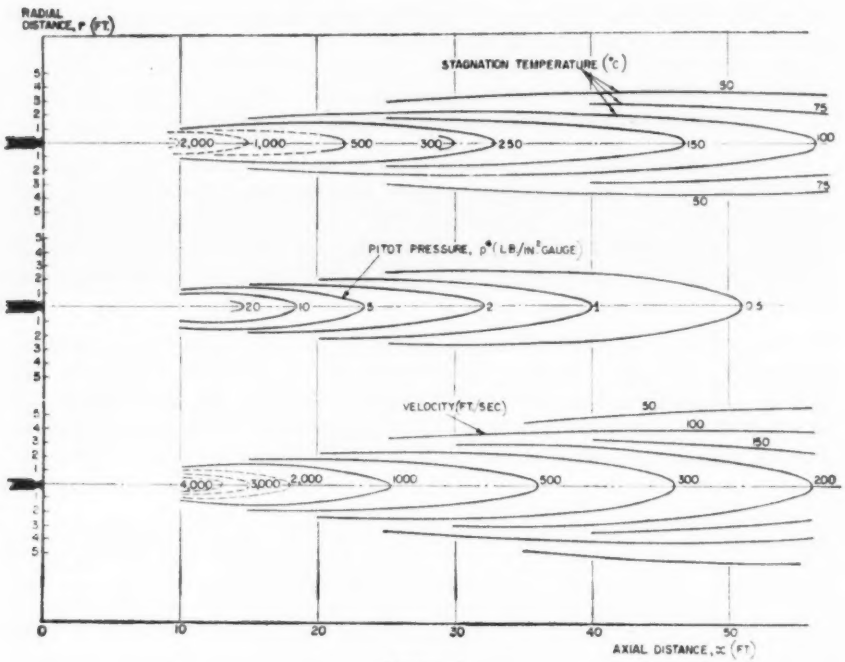

FIGURE 7.

Top diagram: Distribution of stagnation temperature in jet stream.
Middle diagram: Distribution of Pitot pressure in jet stream.
Lower diagram: Distribution of velocity in jet stream.

The results of Ref. 5 indicate lengths of the supersonic jets (varying between 6·25 and 9 ft.) which are much smaller than that from the motor used for the present work (for which it is 17 ft.) and that the axial pressure and temperature decay starts much earlier; *e.g.* at a distance of $x = 26{\cdot}5$ ft. our measured pressure is about 12 times and our temperature is about 5 times larger than the respective values of rocket *A* ($M = 3{\cdot}53$) in Figs. 18 and 19.

TABLE III

THE ANGULAR DISPLACEMENT FROM THE JET AXIS FOR GIVEN DECAY RATIOS OF TEMPERATURE, PRESSURE AND VELOCITY IN THE REGION OF SUBSONIC FLOW FROM AN UNDER-EXPANDED NOZZLE

Decay Ratio	*Temperature*	*Pressure*	*Velocity*
	Angular Displacements		
3/4	1·8°	1·7°	2°
1/2	3·5°	3·2°	4°
1/4	5·2°	4·7°	6°
1/10	6·4°	5·8°	7·15°

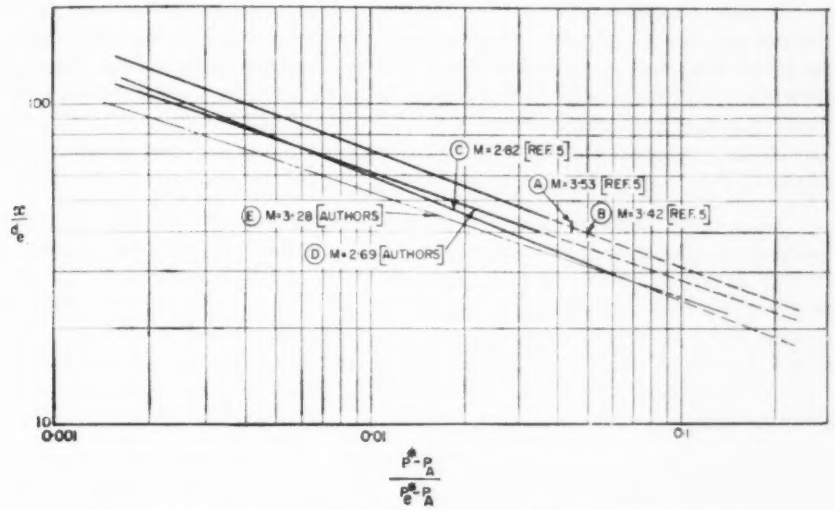

FIGURE 18. Pitot pressure along the axis compared with values from Ref. 5.

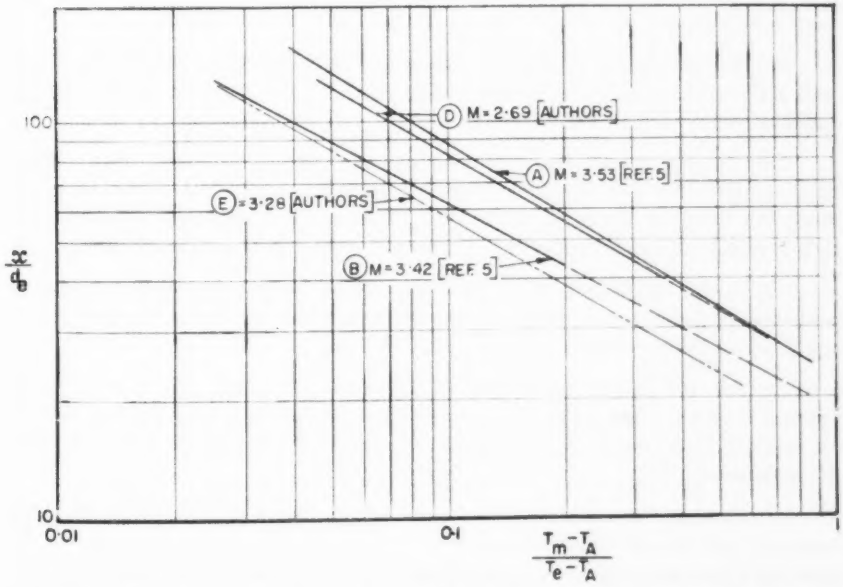

FIGURE 19. Stagnation temperature along the axis compared with values from Ref. 5.

A more adequate comparison of the axial pressure and temperature decay in the subsonic jet can be made by introducing non-dimensional parameters. Since the throat diameters of the rockets mentioned are not known, the values found in the present work have been recalculated in terms of the ratio of distance from the nozzle to nozzle exit diameter x/d_e. The results are plotted as curves *D* in Figs. 18 and 19; the pressure at the exit is 41 lb./in.² absolute and $M=2{\cdot}69$ at the exit. The results of Ref. 5 are plotted as curves *A* ($M=3{\cdot}53$), *B* ($M=3{\cdot}42$) and *C* ($M=2{\cdot}82$).

When comparing these curves it should be noted that curve *D* applies to an under-expanded nozzle of cone angle 30°, whereas *A*, *B* and *C* apply (by inference) to fully expanded nozzles of cone angles 50°, 60° and 30° respectively. If the results of curve *D* are replotted in terms of the theoretical exit diameter for full expansion to atmospheric pressure ($p=14{\cdot}7$ lb./in.² absolute and $M=3{\cdot}28$), curves *E* of Figs. 18 and 19 are obtained. It is clear that the results are not compatible. Further experiments are necessary to establish the effects of nozzle expansion ratio and cone angle.

(Curve *C* has been omitted from Fig. 19 since, in contrast to the curves for rockets *A* and *B*, this rocket produced a jet with spontaneous afterburning, which shifted the temperature scale downstream.)

6. Conclusions

(*i*) Observations in the supersonic flow unaffected by disturbances from the exit of a conical nozzle (included angle 30°, area ratio 7·7:1) are consistent with very nearly conical or "source" flow at the exit plane of the nozzle.

(*ii*) The flow from a nozzle of area ratio 4:1 inclined at 15° from the motor axis follows the axis of the nozzle within $\pm\frac{1}{4}°$. This is true for nozzles having included angles of 15° and 30°.

(*iii*) The flow from a nozzle of area ratio 4:1 with 15° included angle is more concentrated than that from one with 30° included angle. At about 40 throat diameters from the nozzle the Pitot pressure falls off to one half its value on the axis at angular displacements of $1\frac{1}{2}°$ for the 15° cone and 2° for the 30° cone.

(*iv*) In the region of subsonic flow the total pressure, stagnation temperature and velocity decay logarithmically along the axis. The results for the motor used are given non-dimensionally in Fig. 16.

(*v*) For the motor (with under-expanded nozzle) used, the total pressure (gauge), stagnation temperature (above ambient temperature) and velocity fall off to one half their values on the axis at angular displacements of 3·2°, 3·5° and 4° respectively.

(*vi*) From the few measurements made in the region of supersonic flow and from comparison with the results of Ref. 5, it is clear that the angle of the nozzle cone, the expansion ratio of the nozzle relative to expansion to atmospheric pressure, as well as the combustion chamber pressure and temperature, affect significantly the distribution of pressure, temperature and velocity throughout the exhaust jet.

ACKNOWLEDGMENTS

This paper is based on work done at the Rocket Propulsion Department, Westcott and is published by permission of the Director. The illustrations are Crown Copyright.

REFERENCES

1. KUETHE, A. M. Investigation of the Turbulent Mixing Region Formed by a Jet. *Journal of Applied Mechanics*, Vol. 2, *A*-87, 1935.

2. WUEST, W. Turbulente Mischungsvorgaenge in zylindrischen und kegeligen Fangduesen. *V.D.I.Zeitschrift*, Vol. 92, 35, 1000, 1950.

3. PRANDTL, L. *Essentials of Fluid Dynamics*. Blackie, London, 1952.

4. FRASER, R. P. and ROWE, P. N. The Design of Supersonic Nozzles for Rockets. Imperial College of Science, Report No. JRL 28, October 1954.

5. ANDERSON, A. R. and JOHNS, F. R. Characteristics of Free Supersonic Jets Exhausting into Quiescent Air. *Journal of the American Rocket Society*, Vol. 25, 1, 13, 1955.

Compression Tests on Thin-Walled Cylinders

M. HOLMES, B.Sc., Ph.D., A.M.I.C.E.

(Department of Civil Engineering, University of Bristol)

SUMMARY: The paper describes compression tests on eight thin-walled cylinders of 3 ft. diameter and 0·035 in. wall thickness made of aluminium alloy plate. The lengths of the cylinders were either 6 ft. or 9 ft. Three of the cylinders were tested under axial compression up to buckling failure, and the initial buckling load, failing load and mode of buckling were observed. A further three cylinders were similarly tested, but these cylinders were subjected to internal pressure before applying the compressive load. The internal pressure had a twofold strengthening effect on these cylinders. Firstly, it induced a tensile pre-stress along the axis of the cylinder and, secondly, it resulted in the value of the compressive stress at which buckling occurred being greater than the buckling stress value for the unpressurised cylinders. The six cylinders were tested in a manner which allowed the end face of each cylinder to rotate about a diametral axis. A parallel platen device was used in testing the last two cylinders (in an unpressurised condition) which restrained rotation of the end faces of the cylinders. These tests enabled the effect of end restraint to be studied, and also enabled measurements of load-carrying capacity at large axial deflections to be made. The initial buckling loads, failing loads and modes of buckling observed in the tests were compared with existing large deflection theory.

1. Introduction

It is well known that thin tubes in compression commonly buckle in one of two modes; for very thin tubes, diamond pattern buckles (more or less elastic) form with their diagonals longitudinally and circumferentially disposed, while for rather thicker tubes circumferential wrinkles (plastic) arise to form circumferential corrugations. It is also generally known that the compression loads at which such deformations occur are substantially below (roughly one third of) the buckling loads predicted by small deflection theory.

The production of accurate thin tube for missile purposes has made available thin-walled cylinders with diameter/thickness ratios higher than hitherto practicable; this, with the possibility of, and current interest in, pressurisation of such tubes, rendered compression experiments on thin large cylinders very desirable.

By arrangement with Mr. H. B. Howard of the Ministry of Supply (now Ministry of Aviation), eight 3 ft. diameter tubes, some 6 ft. long and some 9 ft. long, were specially constructed by Saunders-Roe Ltd. This paper describes the tests carried out on these cylinders in the Department of Civil Engineering of the Univer-

Received February 1961.

TABLE I

Specimen	*End Condition*	*Length* (ft.)	*Internal Pressure* (lb./in.²)		*Buckling Load* (tons)		
			at top	*at bottom*	*Total*	*Taken by water pressure*	*Taken by cylinder*
1	ball	6	0	0	7·9	0	7·9
2	ball	6	0	0	5·9	0	5·9
3	ball	6	28·4	31·0	28·8	12·9	15·9
4	ball	9	0	0	5·2	0	5·2
5	ball	9	20·7	24·6	25·4	9·4	16·0
6	ball	9	8·1	12·0	15·8	3·7	12·1
7	platen	6	0	0	8·6	0	8·6
8	platen	8·5	0	0	6·5	0	6·5

sity of Bristol. A large testing frame available in the laboratories there was specially modified for the purpose and a brief description of this is included.

The large deflection theory of thin tubes in compression, initiated by von Kármán and by Leggett in the early part of the Second World War, has since been developed in the United States to apply to pressurised as well as unpressurised thin cylinders. At the end of this paper the results of the tests described here are compared with the predictions of this theory.

Table I shows the main results obtained during the testing of the specimens and the photographs of Fig. 1 illustrate the types of buckling failure which were observed.

NOTATION

R radius of cylinder

L length of cylinder

t wall thickness

P internal pressure

E modulus of elasticity

f_{cr} buckling stress for internal pressure p

$f_{cr}' = f_{cr}(R/Et)$

f_{cr0} buckling stress for internal pressure $p = 0$

$f_{cr0}' = f_{cr0}(R/Et)$

$p' = (p/E)(R/t)^2$

2. Description of Specimens

The specimens were all formed from L-70 aluminium alloy in 20 s.w.g. sheet. The 6 ft. long specimens were manufactured with one longitudinal lap-welded seam.

(*a*) Specimen 1. Failed at 7·9 tons, pressure zero.

(*b*) Specimen 6. Failed at 15·8 tons, pressure 8·1 lb./in.².

(*c*) Specimen 5. Failed at 25·4 tons, pressure 20·7 lb./in.².

(*d*) Specimen 3. Failed at 28·8 tons, pressure 28·4 lb./in.².

FIGURE 1.

For the 9 ft. specimens, circumferential lap welds were used to join three 3 ft. sections, the longitudinal seams in each section being staggered. In manufacture one of the 9 ft. specimens was damaged; after cutting away the damaged section the finished specimen was 8 ft. 6 in. long.

Each specimen was fitted with end rings formed by bending a length of angle section to a suitable radius. One leg of this angle section was riveted to the cylinder and the other leg was bolted to a 3 ft. 6 in. × 3 ft. 6 in. × ½ in. steel end-plate. During testing, both the steel end-plates were backed by a 3 ft. 6 in. × 3 ft. 6 in. × 4 in. reinforced concrete slab and a layer of cement mortar was applied between the slab and steel end-plates to ensure overall contact. The various features described can be seen in the photographs of Fig. 1.

3. Testing Frame

The specimens were tested in a large frame in the Civil Engineering Laboratories at Bristol University. Essentially this testing frame is a strong structural framework built up from standard steel sections. A clear space 20 ft. high × 12 ft. square is provided in the framework for the accommodation of test specimens. At the base of the framework are beams which may be adjusted to support any desired test specimen. Load is applied to a specimen by a single 100-ton hydraulic ram and the framework is so designed that this ram may be placed in any desired position, either in elevation or plan, within the framework.

Load measurements are not taken directly from the ram pressure, because of the relatively high frictional forces which exist in the ram. Instead, loads are measured by an Elliott (electrical resistance) Load Cell placed in series with the ram.

4. Parallel Platen Device

Specimens 1–6 were tested with a ball-and-socket joint between the loading ram and the reinforced concrete backing slab. In testing Specimens 7 and 8 it was desired to prevent rotation of the end faces of the specimens; consequently a parallel platen device was used for load application. This device consists of a tubular guide, 7 in. diameter and 18 in. long, which is held rigidly under the loading ram by beams connecting into the structure of the testing frame. Through this guide passes a solid circular shaft, of the same diameter as the guide, with a mushroom end of 24 in. diameter. Load is thus applied from the loading ram through the shaft with its mushroom end to the concrete backing slab of the specimen. In this way rotation of the end face of the specimen is prevented. The parallel platen device is illustrated in Fig. 2.

5. Application of Internal Pressure

It has been mentioned already that some of the cylinders were tested under axial compression with internal hydrostatic pressure. The method by which this pressure was applied and measured is illustrated in Fig. 3.

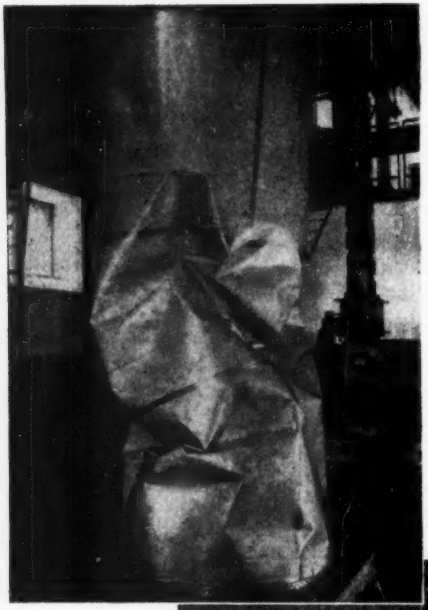

(*a*) Specimen 8. Parallel platen test.

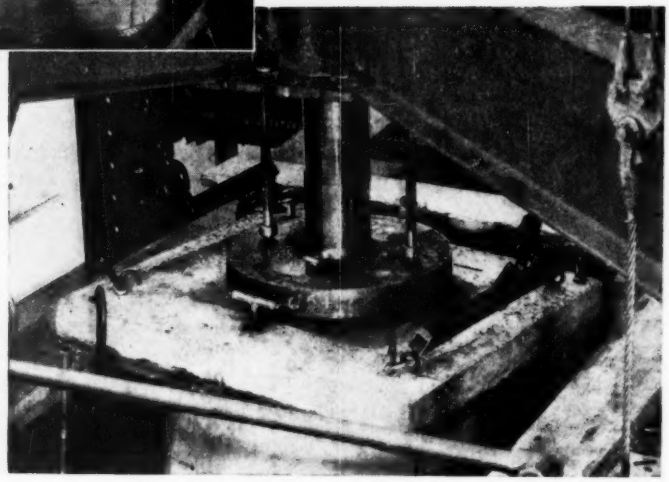

(*b*) Parallel platen device.

FIGURE 2.

As there was a considerable leakage of water at the welded seams and the end-plates, a procedure had to be adopted to keep the pressure constant during the test. Valve *A* was set to give a supply from the mains which just exceeded the losses due to leakage; this setting of valve *A* was left unaltered during the course of the test. During the test, water was bled from the system through the fine control valve *B*, so that the levels in the mercury manometer at *C* and *D* remained constant. In this way the pressure in the cylinder could be maintained within ± 2 per cent of the desired value during the entire course of a test.

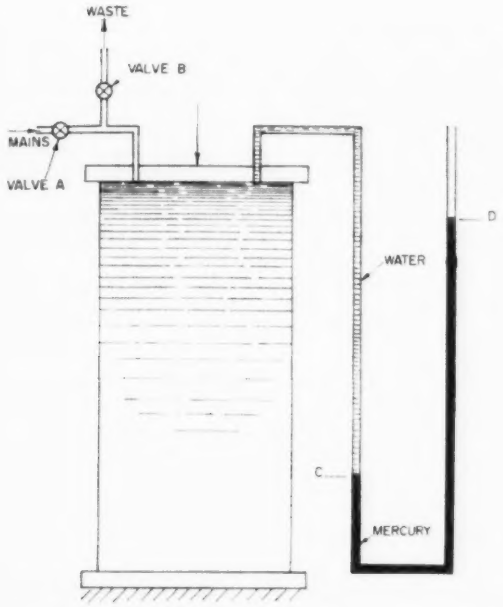

FIGURE 3. Pressure system.

The use of water as a pressurising agent meant that there was a variation in pressure from the top to the bottom of a test cylinder. This was considered preferable to the use of air and the consequent dangers of a blow out.

6. Test Procedure

Before beginning the loading tests, measurements were made of the cylinder wall irregularities; where appropriate, these measurements were repeated after the application of internal pressure.

In carrying out tests in which internal pressure was to be applied, the full pressure was applied first, then the axial compressive load was applied and increased in small increments up to failure. For some, but not all, of the test cylinders, measurements of the longitudinal shortening of the cylinder were made. Readings were taken with 1/1000 in. dial gauges across the four corners of the end-plates; thus both the average longitudinal shortening and the rotation of the end-plates could be determined.

Observations through a theodolite, on a vertical line drawn on the surface of a cylinder, showed that the line remained vertical up to and beyond failure, thus indicating the absence of any torsional effects.

7. Test Results

The main test results have already been given in Table I. Further details are given in Table II.

TABLE II

Specimen	*Pressure* (lb./in.^{2})	*Buckling Load* (tons)	*Size of Buckles* (in.) (circumferential × longitudinal)	*Remarks*
1	0	7·9	13×13	Buckles at 7·9 tons; second loading buckles at 4·6 tons, third at 4· 2 tons.
2	0	5·9	13×13	Buckles could be heard forming at 2·8 and 5·4 tons. Load fell off at 5·9 tons.
3	28·4–31·0	28·8	πD× 2	Plastic bulge formed slowly. Load fell off sharply at 28·8 tons.
4	0	5·2	13×13	Buckles could be heard forming at 2·7, 4·6, 5·2 tons. Load fell off at 5·2 tons.
5	20·7–24·6	25·4	9× 3	Plastic buckles formed slowly. Load fell off sharply at 25·4 and 15·8 tons respectively.
6	8·1–12·0	15·8	9× 4	
7	0	8·6	13×13	Buckles at 7·1, 8·1, 8·6 tons. Load fell off at 8·6 tons.
8	0	6·5	13×13	Buckles at 3·6, 5·8, 6·5 tons. Load fell off at 6·5 tons.

At a load of 7·9 tons, Specimen 1 buckled suddenly and noisily, with a marked fall off in the applied load. With the load steady at this lower level, existing buckles disappeared and new ones formed at other locations. On removal of the applied load the buckles apparently disappeared completely, but a close inspection revealed some permanent deformation at points corresponding to the corners of the diamond buckles. As shown in Table II, on applying the load a second and third time, lower values were obtained for the buckling load.

The modes of failure for the other unpressurised tests (Specimens 2 and 4) were generally similar to Specimen 1. However, in both these later tests, isolated buckles were heard and seen to form at very low applied loads. The formation of these premature buckles did not seem to affect the load-carrying capacity of the specimens to any marked extent, so that loading was continued until a sharp fall-off in load, accompanied by an extensive buckle pattern, occurred. Details of the loads at which buckles formed are given in Table II, and the load/deflection curves for Specimens 1 and 2 are shown in Figs. 4 and 5. These figures show that the load/deflection characteristics of Specimens 1 and 2 were very different from each other.

It has already been mentioned that the buckles in Specimen 1 substantially disappeared when the applied load was removed; in the case of Specimen 2 the buckles largely remained when the applied load was released. Some time later, however, when the end-plates were unbolted, the buckles in Specimen 2 suddenly "jumped out," leaving only small permanent deformations corresponding to the corners of the diamond buckles. Specimen 4 was given a considerable axial deflection after failure and the diamond buckle pattern was permanently formed in the walls of the cylinder.

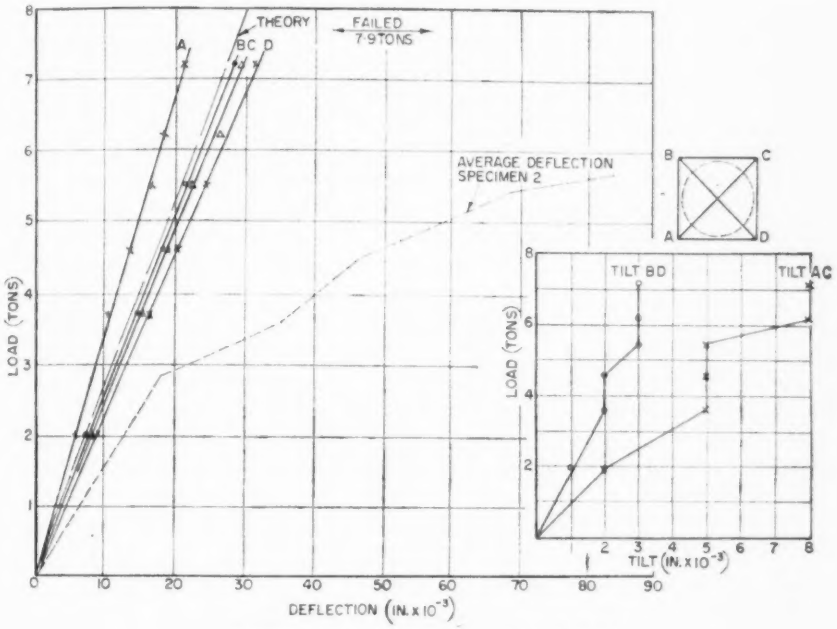

FIGURE 4. Specimen 1, unpressurised, 6 ft.

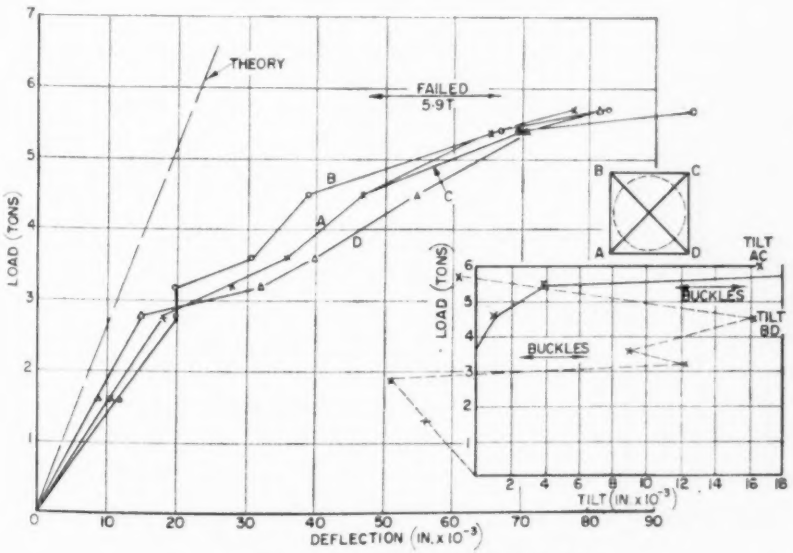

FIGURE 5. Specimen 2, unpressurised, 6 ft.

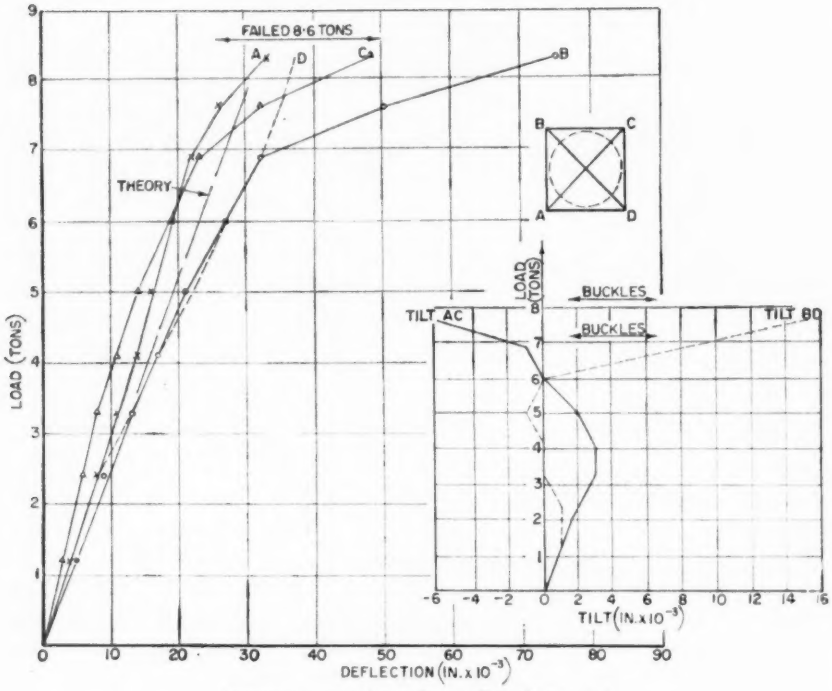

FIGURE 6. Specimen 7, parallel platen, 6 ft.

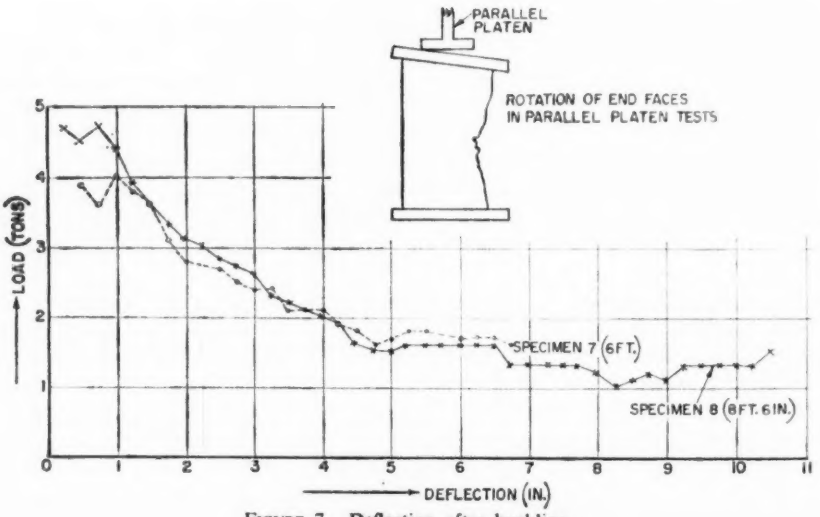

FIGURE 7. Deflection after buckling.

In contrast to the unpressurised tests, the buckles which occurred during the pressurised tests (Specimens 3, 5 and 6) formed slowly. The first evidence of the formation of buckles came in a greater tendency for the internal pressure to increase due to decreasing volume; the rate at which water was being bled from the system had to be increased to maintain a constant internal pressure. At this stage the buckles could be seen to be increasing their depth in the radial direction, although their plan size remained sensibly constant. When the buckling loads recorded in Table II had been attained, a sharp falling off in applied load accompanied by a rise in internal pressure was observed. The buckles which formed in these pressurised tests remained almost unchanged after the removal of both the applied load and the end-plates.

Specimens 7 and 8 were tested in an unpressurised condition by applying the compressive load through the parallel platen device. The general behaviour and mode of failure of these specimens was very similar to that already described for the unpressurised specimens loaded through a ball joint. The load/deflection curves for Specimen 7, taken up to failure, are shown in Fig. 6, and Fig. 7 shows the load/deflection curves for Specimens 7 and 8, taken beyond failure up to a maximum longitudinal deflection of 10 in. The appearance of the specimens at large longitudinal deflection may be seen in the photograph of Fig. 2.

It had been expected that the parallel platen device would prevent all rotation of the end faces of Specimens 7 and 8; however, this proved not to be the case. The end faces of these specimens did rotate, as the applied load was increased, resulting in the specimens being eccentrically loaded as the point of contact between the parallel platen and the concrete backing slab shifted from the axis of the cylinders. This can be seen in the photograph of Fig. 2, and is illustrated diagrammatically in Fig. 7.

It has been mentioned earlier that measurements were made of the cylinder wall irregularities; a typical sample of the results obtained from such measurements is shown in Fig. 8. These measurements were taken at one-inch intervals along

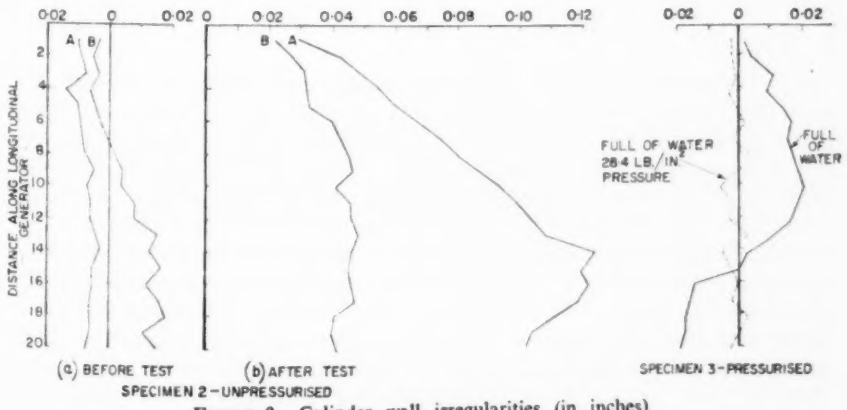

FIGURE 8. Cylinder wall irregularities (in inches).

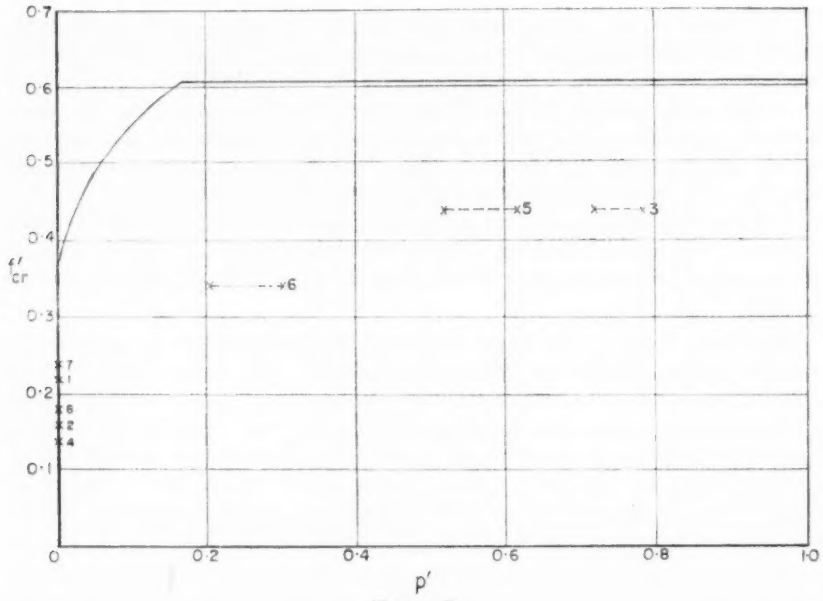

FIGURE 9.

selected longitudinal generators (*A* and *B*), using a 1/1000 in. dial gauge mounted on a slide which moved along a rigid steel straight edge. The results shown in Fig. 8 indicate that, before test, Specimen 2 had maximum wall irregularities of ±0·020 in.; after buckling under zero internal pressure and removal of load, this figure could be ±0·130 in. The results shown for Specimen 3 indicate a very significant reduction in wall irregularities due to the application of internal pressure.

The results of subsidiary tests carried out to determine material properties are recorded in Appendix I.

8. Theory

The small deflection theory put forward by Southwell[1], gives a value for f_{cr0}' of 0·605 (for a material having a Poisson's ratio value of 0·3). Leggett[2], and others, confirmed the value for f_{cr0}' of 0·605 for small deflections, but showed that the stress after buckling, when the deflections are large, corresponds to a value of f_{cr0}' much lower than 0·605. Lo[3], extending the large deflection theory to include the effects of internal pressure, obtained a theoretical relationship connecting f_{cr}' and p'. This theoretical relationship is plotted in Fig. 9, together with the experimental results; the two p' values shown for each test correspond to the pressure at the top and bottom of the cylinder. On this analysis $f_{cr0}' = 0{\cdot}376$ and $f_{cr}' = 0{\cdot}605$ for $p > 0{\cdot}17$. It will be seen that a line drawn through the experimental points would be approximately parallel to the theoretical line but offset some distance from it. This kind of observation led Fung and Sechler[4] to suggest that Lo's result should be plotted in the form $(f_{cr}' - f_{cr0}')$ against p', and this curve is shown in Fig. 10.

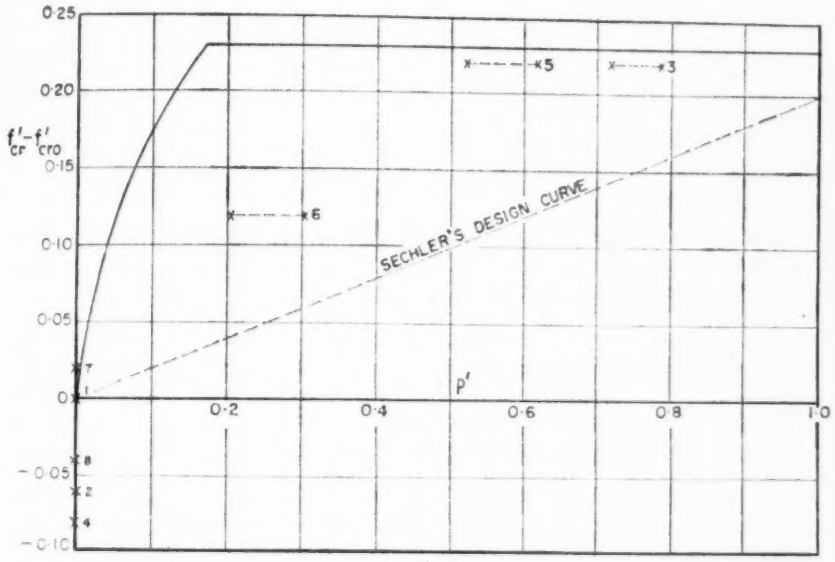

FIGURE 10.

The experimental points on Fig. 10 were plotted using the relationship

$$(f_{cr}'-f_{cro}')_{exp}=(f_{cr}')_{exp}-0{\cdot}22 \quad . \quad . \quad . \quad . \quad (1)$$

The value of $f_{cro}'=0{\cdot}22$ was derived from the following empirical relationship obtained by Kanemitsu and Nojima[5]:—

$$f_{cro}'=(R/t)\,[9\,(t/R)^{1{\cdot}6}+0{\cdot}16\,(t/L)^{1{\cdot}3}] \quad . \quad . \quad . \quad (2)$$

This gives a value $f_{cro}'=0{\cdot}22$ for both the 6 ft. and 9 ft. cylinders. By using relation (1), it is apparent that better agreement between experimental and predicted results is shown in Fig. 10 than in Fig. 9.

9. Discussion of Results and Conclusions

The results of the five unpressurised tests show a considerable variation in the buckling stress, the experimental values of f_{cro}' being between 0·14 and 0·24, with an average value of 0·19; these compare with a value of 0·22 from Kanemitsu and Nojima's empirical relationship (equation (2)).

There is some evidence suggesting that the scatter of the test results was due to the magnitude of the cylinder wall irregularities. This experimental evidence is summarised as follows:—

(*a*) Table III shows the average wall irregularity obtained from measurements of at least 100 points on the surface of each cylinder. It will be seen that high wall irregularity is associated with relatively low failing loads. The actual readings from which the average wall irregularities were derived are shown in Appendix II.

TABLE III

Specimen	*End Condition*	*Average Wall Irregularity* (1/1000 in.)	*Failing Load* (tons)
2	ball	11	5·9
4	ball	33	5·2
7	platen	7	8·6
8	platen	13	6·5

(*b*) Test results from Specimen 1 show that for successive loadings the failing load was 7·9, 4·6, 4·2 tons. This indicates that each successive loading increased the wall irregularities and hence decreased the subsequent failing load.

(*c*) Figures 4 and 5 illustrate the large variation in load/deflection characteristics between Specimens 1 and 2. A relatively small deflection per unit load is seen to be associated with a relatively high failing load. Large deflections will occur where wall irregularities are high, as axial shortening due to bowing of the cylinder walls will be superimposed onto the shortening due to direct axial strain.

The parallel platen was imperfect in so far as it allowed some relative rotation of the end faces of the specimens to take place, resulting in an eccentricity of loading tending to restore the end faces to their parallel positions. The following results, however, show an increase in strength of the parallel platen tests over the ball-ended tests:—

average failing load, three ball-ended tests $= 6{\cdot}3$ tons,

average failing load, two parallel-platen tests $= 7{\cdot}6$ tons.

By pressurising the cylinders, the wall irregularities were reduced and, in addition, the buckle pattern at failure was considerably changed. The results show that, as well as the pre-tensioning effect of pressurisation, there was also a very considerable increase in buckling stress caused by the applied internal pressure. Fig. 10 shows that, for internal pressures corresponding to $p' > 0{\cdot}5$, large deflection theory accurately predicts the failing load of the specimens; the agreement for Specimen 6 where $p' < 0{\cdot}5$ is not very satisfactory.

The size of the buckles that arose in the unpressurised tests is of interest. These had diagonal dimensions (*i.e.* semi-wave lengths) of about 13 in., whereas classical linear theory indicates a value of about 2·7 in. Thus the experimental buckles were nearly five times this theoretical size. This result is qualitatively similar to that obtained by Robertson[6], but in his tests the ratio was only about two. The change in buckle size and shape due to pressurisation is generally similar to that observed by Fung and Sechler[4].

ACKNOWLEDGMENT

The work described in this paper was carried out under the general supervision of Professor Sir Alfred Pugsley, for whose advice and interest the author wishes to express his gratitude.

References

1. Southwell, R. V. On the General Theory of Elastic Stability. *Phil. Trans. Roy. Soc.* A, Vol. 213, 1914.
2. Leggett, D. M. A. and Jones, R. P. N. The Behaviour of a Cylindrical Shell under Axial Compression when the Buckling Load has been Exceeded. R. & M. 2190, 1942.
3. Lo, H., Crate, H. and Schwartz, E. B. Buckling of Thin-Walled Cylinder under Axial Compression and Internal Pressure. N.A.C.A. Report 1027, 1951.
4. Fung, Y. C. and Sechler, E. E. Buckling of Thin-Walled Circular Cylinders under Axial Compression and Internal Pressure. *Journal of the Aeronautical Sciences*, Vol. 24, 1957.
5. Kanemitsu, S. and Nojima, H. Axial Compression Tests of Thin Circular Cylinders. M.S. Thesis, Guggenheim Aeronautical Laboratory, California Institute of Technology, 1939.
6. Robertson, A. The Strength of Tubular Struts. *Proc. Roy. Soc.*, A, Vol. 121, p. 558, 1928.

Appendix I

The following material properties and dimensions were measured from Specimen 1.

Diameter	$=36$ in.
Wall thickness	$=0{\cdot}035$ in.
Ultimate tensile stress	$=30{\cdot}9$ tons/in.^{2}
0·1 per cent proof stress	$=20{\cdot}4$ tons/in.^{2}
Modulus of elasticity	$=4{,}670$ tons/in.$^2=10{\cdot}5\times10^6$ lb./in.^{2}
Cross-sectional area	$=3{\cdot}96$ in.^{2}

Appendix II

The actual readings from which the average wall irregularities quoted in the paper were derived are given in Table IV. Their derivation is illustrated by Fig. 11.

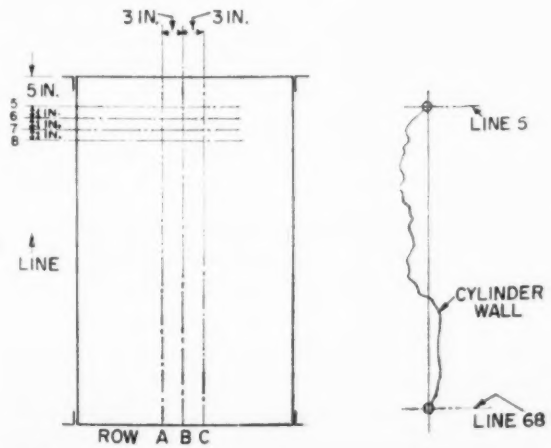

Figure 11. Cylinder wall irregularities.

TABLE IV

AVERAGE WALL IRREGULARITIES

+ Outward − Inward

Line	*Specimen* 2 (6 ft. long)			*Specimen* 4 (9 ft. long)			*Specimen* 7 (6 ft. long)			*Specimen* 8 (8 ft. 6 in. long)		
	Row			Row			Row			Row		
	A	B	C	A	B	C	A	B	C	A	B	C
5	0	0	0	0	0	0	0	0	0	0	0	0
10	−10	− 3	+ 9				− 1	+ 1	+ 1			
11	− 9	− 5	+14				− 1	+ 1	+ 1			
12	− 8	− 3	+13				− 2	+ 4	+ 5			
13	−14	− 6	+12				− 2	+ 4	+ 5			
14	−10	− 4	+13				− 4	+ 4	+ 8			
15	− 9	− 3	+13				− 5	+ 5	+ 8			
16	− 9	− 1	+14				− 8	+ 7	+ 8			
17	− 8	+ 1	+13				− 8	+ 7	+ 8			
18	− 5	+ 4	+14				− 8	+ 8	+ 9			
19	− 7	+ 4	+15				− 8	+ 9	+10			
20	− 6	+ 8	+16	− 1	+ 6	+ 1	− 9	+10	+10	−23	−21	−10
21	− 6	+ 7	+14	+ 1	+ 9	+ 4	− 9	+10	+10	−24	−21	− 9
22	− 4	+14	+17	+ 5	+ 9	+ 5	− 8	+10	+10	−25	−19	− 6
23	− 3	+13	+18	+13	+16	+10	− 9	+10	+13	−24	−17	− 4
24	− 5	+16	+14	+15	+19	+ 8	− 9	+10	+14	−26	−12	− 2
25	− 5	+12	+16	+18	+22	+12	− 9	+10	+14	−28	−10	− 2
26	− 6	+16	+18	+18	+26	+13	− 9	+ 9	+12	−26	− 7	0
27	− 6	+17	+13	+23	+30	+17	− 8	+ 6	+10	−26	− 4	+ 1
28	− 6	+11	+12	+27	+31	+20	−10	+ 6	+10	−26	− 3	+ 1
29	− 7	+15	+16	+28	+33	+23	−10	+ 6	+10	−27	+ 1	+ 3
30	− 6	+12	+18	+29	+35	+22	− 9	+ 6	+ 8	−24	0	+ 4
31	− 7	+13	+18	+31	+37	+24	−10	+ 7	+ 6	−25	+ 6	+ 8
32	− 9	+15	+13	+38	+35	+26	−11	+ 4	+ 5	−22	+ 6	+ 9
33	−12	+11	+15	+41	+35	+26	−11	+ 4	+ 5	−22	+ 8	+11
34	−14	+14	+13	+45	+35	+31	−11	+ 2	+ 3	−25	+ 8	+11
35	−17	+14	+12	+50	+34	+28	− 9	+ 3	+ 2	−18	+11	+13
36	−19	+13	+14	+35	+43	+35	− 9	+ 3	+ 2	−18	+13	+14
37				+30	+43	+39				−16	+14	+15
38				+24	+49	+38				−16	+13	+13
39				+17	+52	+35				−15	+13	+13
40				+10	+57	+34				−13	+11	+16
41				+11	+58	+35				−11	+11	+15
42				+20	+55	+34				−12	+10	+14
43				+24	+55	+34				−10	+ 9	+15
44				+30	+54	+34				− 7	+10	+11
45				+23	+52	+33				− 6	+ 8	+ 8
46				+27	+49	+33				− 5	+ 8	+ 6
47				+30	+45	+30				− 4	+ 3	+ 2
48				+31	+46	+31						
49				+34	+44	+32						
50				+28	+43	+32						
51				+26	+38	+29						
52				+23	+35	+29						
53				+24	+40	+25						
54				+21	+28	+21						
55				+17	+23	+17						
56				+ 9	+20	+16						
57				+ 4	+14	+ 8						
58				+ 4	+13	+ 5						
59				+ 6	+ 9	+ 4						
68	0	0	0	0	0	0	0	0	0	0	0	0
	Average = 11/1000 in.			Average = 33/1000 in.			Average = 7/1000 in.			Average = 13/1000 in.		

Mass Transfer Cooling in a Boundary Layer

D. G. HURLEY

(Aeronautical Research Laboratories, Australian Defence Scientific Service)

SUMMARY: Previous theoretical work on mass transfer cooling is reviewed and it is shown that this may be complemented by similar solutions that occur when the velocity outside a two-dimensional boundary layer varies as some power of the distance from the front stagnation point. The case of stagnation point flow with constant wall temperature is investigated in some detail, under the assumption that the temperature differences are everywhere small compared with the absolute temperature. Calculations on an analogue computer, supplemented by an investigation of the asymptotic behaviour, are used to determine the boundary layer development and heat transfer rates when the coolant is hydrogen, helium, steam or carbon dioxide. It is found that, on a mass flow basis, hydrogen reduces the heat transfer rate most and that steam is the next most effective of the substances investigated.

1. Introduction

The interest in mass transfer cooling has increased recently because it is a promising method of reducing the surface temperatures of high speed aircraft, missiles and satellites re-entering the earth's atmosphere.

In mass transfer cooling a foreign gas is emitted from the surface of the body and diffuses through the boundary layer, thus affecting its development and the heat transfer rate. The emission can arise from the evaporation of a liquid, the sublimation of the surface material or from the injection of a foreign gas through holes in the surface.

Extensive theoretical work on this topic has been reported for the case when the molecular weights of the emitted gas and that in the external stream are the same, and this is summarised in Ref. 1. Analytical investigations of the more general problem appear to have been confined to the case when the Mach number in the external stream is constant* and the emitted gas is a light one, either hydrogen or helium (*e.g. see* Ref. 3).

In the present paper it is shown that this work may be complemented by similar solutions that occur when the velocity outside a two-dimensional boundary layer varies as some power of the distance from the front stagnation point. The case

*When this work was nearly completed the author's attention was drawn to Ref. 2, which deals with the effect of helium injection on the heat transfer near a stagnation point in axisymmetric flow.

Received January 1961.

of stagnation point flow with constant wall temperature is then investigated in some detail, under the assumption that the temperature differences are everywhere small compared with the absolute temperature.

NOTATION

A constant (*see* equation (49))

$a = mM\phi_{\rho w}$ (*see* equation (57))

B constant (*see* equation (49))

$b = mMS_\infty$ (*see* equation (58))

C constant (*see* equations (17) and (49))

C_1, C_2, C_3, C_4 constants (*see* equations (44) and (48))

C_p specific heat at constant pressure

D constant (*see* equation (51))

D_{12} coefficient of binary diffusion

E constant (*see* equation (54))

F constant (*see* equation (57))

f non-dimensional stream function, $= \dfrac{\rho_\infty \psi}{(\rho_\infty \mu_\infty u_\infty x)^{1/2}}$

$g = \dfrac{1}{\phi_\rho} f - \dfrac{1}{S_\infty \phi_\rho} \dfrac{d\phi_\rho}{d\eta}$

$G = g - \eta + \delta$

$h = g + mM$ (*see* Section 6.5)

H_T stagnation enthalpy in external stream

k coefficient of thermal conductivity

$l = \phi_\rho - \phi_{\rho w}$ (*see* Section 6.5)

$m = m_2/m_1$

m_1, m_2 molecular weight of foreign gas and air respectively

M' mass flow per unit area of surface per unit time

M mass flow parameter, $= M' \left[\dfrac{x}{\rho_\infty \mu_\infty u_\infty}\right]^{1/2}$

n constant (*see* equation (17))

(Nu) Nusselt number, $= \dfrac{Qx}{k_\infty (T_\infty - T_w)}$

p pressure

(Pr) Prandtl number

Q heat transfer per unit area of surface per unit time

r see equation (62)

R (in Sections 2 and 3 only) universal gas constant

R (elsewhere) Reynolds number, $=\rho_\infty u_\infty x/\mu_\infty$

S Schmidt number, $=\nu/D_{12}$

T temperature

u component of fluid velocity in direction Ox

v component of fluid velocity in direction Oy

w mass fraction of foreign gas, $=\rho_1/\rho$

x distance measured along surface from stagnation point

y distance measured normal to surface from wall

δ constant (*see* equation (39))

η non-dimensional distance normal to surface, $=y\left[\frac{\rho_\infty u_\infty}{\mu_\infty x}\right]^{1/2}$

$\theta=\phi_\rho-1$

μ coefficient of viscosity

ν kinematic viscosity

$\xi=\eta-\delta$ (*see* equation (39))

ρ fluid density

$\phi_C, \phi_{C12}, \phi_{D12}=C_p/C_{p\infty}$, C_{p1}/C_{p2}, $D_{12}/D_{12\infty}$, respectively

$\phi_k, \phi_{k12}=k/k_\infty$, k_1/k_2, respectively

$\phi_T, \phi_\mu, \phi_\rho=T/T_\infty$, μ/μ_∞, ρ/ρ_∞ respectively

$\phi_{\mu 12}=\mu_1/\mu_2$

ψ stream function

Suffixes

1 denotes foreign component in binary mixture

2 denotes primary component in binary mixture (air)

∞ denotes value at outer edge of the boundary layer

w denotes values at wall.

2. Boundary Layer Equations

The development of a two-dimensional boundary layer, on a surface through which a foreign gas is being ejected, is considered. When conditions are steady the equations which determine the fluid motion, temperature and concentration of foreign gas are equations (1)-(6) which follow.*

*Equations (1) to (5) are identical with those given on pp. 456-7 of Ref. 4, except that the sign of the second to last term in the energy equation is misprinted in that reference.

Continuity:

$$\frac{\partial}{\partial x}(\rho u)+\frac{\partial}{\partial y}(\rho v)=0. \quad . \quad . \quad . \quad . \quad (1)$$

Diffusion:

$$\rho u\frac{\partial w}{\partial x}+\rho v\frac{\partial w}{\partial y}=\frac{\partial}{\partial y}\left[D_{12}\rho\frac{\partial w}{\partial y}\right]. \quad . \quad . \quad . \quad . \quad (2)$$

Momentum:

$$\rho u\frac{\partial u}{\partial x}+\rho v\frac{\partial u}{\partial y}=-\frac{\partial p}{\partial x}+\frac{\partial}{\partial y}\left[\mu\frac{\partial u}{\partial y}\right] \quad . \quad . \quad . \quad . \quad (3)$$

$$\text{and} \quad \partial p/\partial y=0. \quad . \quad . \quad . \quad . \quad (4)$$

Energy:

$$\rho uC_p\frac{\partial T}{dx}+\rho vC_p\frac{\partial T}{\partial y}=u\frac{\partial p}{\partial x}+\frac{\partial}{\partial y}\left(k\frac{\partial T}{\partial y}\right)$$

$$+\rho D_{12}(C_{p1}-C_{p2})\frac{\partial w}{\partial y}\frac{\partial T}{\partial y}+\mu\left(\frac{\partial u}{\partial y}\right)^2 \quad . \quad (5)$$

State:

$$\frac{p}{\rho}=RT\left[\frac{1}{m_2}+\left(\frac{1}{m_1}-\frac{1}{m_2}\right)w\right]. \quad . \quad . \quad . \quad (6)$$

In these equations x and y are distances measured around the surface from the front stagnation point and normal to the surface respectively, and u and v are the velocity components in these directions. ρ, μ, C_p, T and k are the density, coefficient of viscosity, specific heat at constant pressure, temperature and coefficient of thermal conductivity of the gas mixture respectively; w is the mass fraction of the foreign gas, D_{12} the coefficient of diffusion, p the pressure, C_{p1} and C_{p2} the specific heat of the foreign gas and air respectively, m_1 and m_2 their molecular weights and R is (in this section and in Section 3) the universal gas constant.

In general the physical properties D_{12}, μ, C_p and k will depend on both w and T, and C_{p1} and C_{p2} on T alone. Subsidiary equations defining these dependences are needed to render the six main equations soluble for ρ, u, v, w, p and T.

It is noted that the diffusion equation as stated does not involve the assumption that w is small and that, in the energy equation, account is taken of the energy transfer that arises from diffusion processes.

3. Boundary Conditions

When the foreign gas is ejected through holes in the surface, the mass rate per unit area, M', at which it is transported by both convection and diffusion, may be considered to be prescribed.

Thus, the boundary conditions at $y=0$ are as follows:—

(*i*) $$\rho v w - D_{12}\rho \frac{dw}{dy} = M'. \quad . \quad . \quad . \quad . \quad . \quad . \quad (7)$$

(*ii*) The rate per unit area at which air is transported is zero. Thus

$$\rho v (1-w) + D_{12}\rho \frac{\partial w}{\partial y} = 0. \quad . \quad . \quad . \quad . \quad (8)$$

Addition of equations (7) and (8) gives

$$\rho v = M', \quad . \quad . \quad . \quad . \quad . \quad . \quad (9)$$

which, when substituted into equation (7), gives

$$-D_{12}\rho \frac{\partial w}{\partial y} = M'(1-w). \quad . \quad . \quad . \quad . \quad (10)$$

(*iii*) The tangential velocity component is zero, so that

$$u = 0. \quad . \quad . \quad . \quad . \quad . \quad . \quad (11)$$

(*iv*) The wall temperature is prescribed, so that

$$T = T_w, \quad . \quad . \quad . \quad . \quad . \quad . \quad (12)$$

where suffix "w" denotes values at the wall $y=0$.

It will be assumed that the heat transfer rate per unit area of surface, Q, is given by

$$Q = k_w \left(\frac{\partial T}{\partial y}\right)_w . \quad . \quad . \quad . \quad . \quad . \quad (13)$$

When the mass transfer arises from evaporation or sublimation, M' is not known and an extra boundary condition relating it to the conditions at the wall must be satisfied. Thus the solutions for these cases may be obtained from the ones when M' is prescribed, which are considered later, by selecting those solutions which satisfy this additional condition.

For all cases the boundary conditions at the outer edge of the boundary layer are the same and are, as $y \longrightarrow \infty$,

$$\left.\begin{aligned} u &\longrightarrow u_\infty \\ \rho &\longrightarrow \rho_\infty \\ \text{and} \quad T &\longrightarrow T_\infty \end{aligned}\right\}, \quad . \quad . \quad . \quad . \quad . \quad (14)$$

Suffix ∞ denotes values at the outer edge of the boundary layer. u_∞ and T_∞ must satisfy Bernoulli's equation, which may be written

$$C_{p\infty}T_\infty + \tfrac{1}{2}u_\infty^2 = H_T, \qquad . \quad . \quad . \quad (15)$$

where H_T is the stagnation enthalpy in the external stream.

At the outer edge of the boundary layer, $w = 0$, so that equation (6) gives

$$\frac{p_\infty}{\rho_\infty} = \frac{RT_\infty}{m_2} .$$

Combining this with equation (6) gives, in virtue of equation (4),

$$\phi_T\phi_\rho\,[1 + (m-1)\,w] = 1, \qquad . \quad . \quad . \quad . \quad (16)$$

where $\phi_T = T/T_\infty$, $\phi_\rho = \rho/\rho_\infty$ and $m = m_2/m_1$.

4. Similar Solutions

It would appear that similar solutions of the compressible boundary layer equations may only be obtained under one of the following three conditions:—

(*i*) That the Mach number of the external stream is constant.

(*ii*) That the property values of the gas are assumed to obey certain simple laws: *e.g.* $\mu \propto T$ and the Prandtl number, (Pr), is unity (*see* Ref. 5).

(*iii*) That the Mach number of the external stream is small compared to unity.

If condition (*i*) is satisfied, then similar solutions may also be found to equations (1) to (6) of Section 2, which include the effects of mass transfer[3].

In the present paper it will be assumed that condition (*iii*) is satisfied, that the wall temperature is constant and that the velocity outside the boundary layer is given by

$$u_\infty = Cx^n, \qquad . \quad . \quad . \quad . \quad . \quad . \quad (17)$$

where C and n are constants.

Equation (15) may now be replaced by

$$p_\infty + \tfrac{1}{2}\rho_\infty u_\infty^2 = \text{constant} \qquad . \quad . \quad . \quad . \quad (18)$$

and $T_\infty = \text{constant}$.

Equation (1) is satisfied by introducing a stream function, ψ, such that

$$\left.\begin{aligned} \rho u &= \rho_\infty\,\partial\psi/\partial y \\ \text{and } \rho v &= -\rho_\infty\,\partial\psi/\partial x \end{aligned}\right\} . \qquad . \quad . \quad . \quad (19)$$

Let $$\eta = y\left[\frac{\rho_\infty u_\infty}{\mu_\infty x}\right]^{1/2} \quad . \quad . \quad . \quad . \quad . \quad . \quad (20)$$

and $$f = \frac{\rho_\infty \psi}{(\rho_\infty \mu_\infty u_\infty x)^{1/2}} \quad . \quad . \quad . \quad . \quad . \quad . \quad (21)$$

and suppose that f is a function of η only, so that

$$\left.\begin{aligned} u &= \frac{u_\infty}{\phi_\rho}\frac{df}{d\eta} \\ \text{and} \quad v &= -\frac{u_\infty}{\phi_\rho R^{1/2}}\left[\frac{n-1}{2}\,\eta\frac{df}{d\eta} + \frac{n+1}{2}\,f\right]. \end{aligned}\right\} \quad . \quad (22)$$

where the Reynolds number $R = \rho_\infty u_\infty x/\mu_\infty$.

The assumption that the Mach number is small enables the first and last terms on the right-hand side of equation (5) to be neglected so that, using equations (17) to (22), equations (2), (3) and (5) become, respectively,

$$-\frac{n+1}{2}\,f\frac{dw}{d\eta} = \frac{1}{S_\infty}\frac{d}{d\eta}\left[\phi_{D12}\,\phi_\rho\frac{dw}{d\eta}\right] \quad . \quad . \quad . \quad . \quad (23)$$

$$\frac{n}{\phi_\rho}\left(\frac{df}{d\eta}\right)^2 - \frac{(n+1)}{2}\,f\frac{d}{d\eta}\left(\frac{1}{\phi_\rho}\frac{df}{d\eta}\right) = n + \frac{d}{d\eta}\left[\phi_\mu\frac{d}{d\eta}\left(\frac{1}{\phi_\rho}\frac{df}{d\eta}\right)\right] \quad . \quad . \quad (24)$$

and $$-(Pr)_\infty\frac{(n+1)}{2}\,f\phi_C\frac{d\phi_T}{d\eta} = \frac{d}{d\eta}\left(\phi_k\frac{d\phi_T}{d\eta}\right) + \frac{(Pr)_\infty}{S_\infty}\phi_{D12}\,\phi_\rho\,(\phi_{C12}-1)\frac{dw}{d\eta}\frac{d\phi_T}{d\eta} \quad (25)$$

where $S_\infty = \nu_\infty/D_{12\infty}$, $\phi_{D12} = D_{12}/D_{12\infty}$, $\phi_\mu = \mu/\mu_\infty$,

$(Pr)_\infty = \mu_\infty C_{p\infty}/k_\infty$, $\phi_C = C_p/C_{p\infty}$ and $\phi_{C12} = C_{p1}/C_{p2}$.

The boundary conditions, equations (9) to (12) and (14), become, at $\eta = 0$,

$$\left.\begin{aligned} \frac{n+1}{2}\,f &= -M \\ -M\,(1-w) &= \frac{\phi_{D12}\phi_\rho}{S_\infty}\frac{dw}{d\eta} \\ df/d\eta &= 0 \\ \text{and} \quad \phi_T &= \phi_{Tw} \end{aligned}\right\} \quad . \quad . \quad . \quad . \quad (26)$$

where $M = M'\left[\frac{x}{\rho_\infty \mu_\infty u_\infty}\right]^{1/2}$ is the mass flow parameter, and, as $\eta \longrightarrow \infty$,

$$\left.\begin{aligned} df/d\eta &\longrightarrow 1 \\ \phi_\rho &\longrightarrow 1 \\ \text{and} \quad \phi_T &\longrightarrow 1 \end{aligned}\right\} \quad . \quad . \quad . \quad . \quad . \quad . \quad (27)$$

For the four equations (16) and (23) to (25) to be soluble for f, w, ϕ_ρ and ϕ_T, subsidiary equations are needed which define the dependence of the property values ϕ_{D12}, ϕ_μ and ϕ_{C12} on w and ϕ_T.

5. Stagnation Point Flows for Small Temperature Differences

For the present it will be assumed that the temperature differences are everywhere small compared with the absolute temperature, so that equation (16) simplifies to

$$\phi_\rho [1+(m-1)w]=1. \quad . \quad . \quad . \quad . \quad . \quad . \quad (28)$$

It will also be assumed that

$$u_\infty = Cx, \quad . \quad . \quad . \quad . \quad . \quad . \quad (29)$$

which is valid near a stagnation point where the heat transfer problem is particularly severe.

By equations (28) and (29), equation (23) becomes

$$\frac{f}{\phi_\rho^2}\frac{d\phi_\rho}{d\eta} = \frac{-1}{S_\infty}\frac{d}{d\eta}\left(\frac{1}{\phi_\rho}\frac{d\phi_\rho}{d\eta}\right), \quad . \quad . \quad . \quad . \quad (30)$$

it being assumed that ϕ_{D12} is unity, an assumption that is well satisfied for all gases since D_{12} is nearly independent of concentration.

It is convenient to define a new function g by the relation

$$g = \frac{1}{\phi_\rho} f - \frac{1}{S_\infty \phi_\rho}\frac{d\phi_\rho}{d\eta}, \quad . \quad . \quad . \quad . \quad . \quad . \quad (31)$$

so that equation (30) becomes

$$g\frac{d\phi_\rho}{d\eta} = -\frac{1}{S_\infty}\frac{d^2\phi_\rho}{d\eta^2}. \quad . \quad . \quad . \quad . \quad . \quad . \quad (32)$$

Differentiation of equation (31) gives, using equation (30),

$$\frac{dg}{d\eta} = \frac{1}{\phi_\rho}\frac{df}{d\eta}. \quad . \quad . \quad . \quad . \quad . \quad . \quad (33)$$

From equations (29), (31) and (33), it follows that equations (22), (24) and (25) become equations (34)-(36) which follow.

$$\left.\begin{aligned} u &= u_\infty \frac{dg}{d\eta} \\ v &= -\frac{u_\infty}{R^{1/2}}\left[g + \frac{1}{S_\infty \phi_\rho}\frac{d\phi_\rho}{d\eta}\right] \end{aligned}\right\} \quad . \quad . \quad . \quad . \quad . \quad (34)$$

$$\left(\frac{dg}{d\eta}\right)^2 - \frac{d^2g}{d\eta^2}\left(g + \frac{1}{S_\infty \phi_\rho}\frac{d\phi_\rho}{d\eta}\right) = \frac{1}{\phi_\rho} + \frac{1}{\phi_\rho}\left[\frac{d}{d\eta}\left(\phi_\mu \frac{d^2g}{d\eta^2}\right)\right] \quad . \quad . \quad (35)$$

and $$\phi_k \frac{d^2\phi_T}{d\eta^2} + \frac{d\phi_T}{d\eta}\left[\frac{d\phi_k}{d\eta} + (Pr)_\infty \phi_\rho \phi_C \left(g + \frac{1}{S_\infty \phi_\rho}\frac{d\phi_\rho}{d\eta}\right) + \frac{(Pr)_\infty (1-\phi_{C12})}{S_\infty (m-1)\phi_\rho}\frac{d\phi_\rho}{d\eta}\right] = 0. \quad (36)$$

The boundary conditions (26) and (27) become, at $\eta = 0$,

$$\left.\begin{aligned} g &= -mM \\ d\phi_\rho/d\eta &= MS_\infty(m\phi_\rho - 1) \\ dg/d\eta &= 0 \\ \phi_T &= \phi_{Tw} \end{aligned}\right\} \quad . \quad . \quad . \quad . \quad . \quad (37)$$

and, as $\eta \longrightarrow \infty$,

$$\left.\begin{aligned} dg/d\eta &\longrightarrow 1 \\ \phi_\rho &\longrightarrow 1 \\ \phi_T &\longrightarrow 1 \end{aligned}\right\} \quad . \quad . \quad . \quad . \quad . \quad . \quad (38)$$

The assumption that the temperature differences are small compared to the absolute temperature enables the dependence of the property values ϕ_μ, ϕ_k and ϕ_{C12} on ϕ_T to be ignored. Thus equations (32) and (35) do not involve ϕ_T and may be solved for g and ϕ_ρ. Once their solution is known, equation (36) may be solved for ϕ_T.

6. Solution of Diffusion and Momentum Equations

The solutions of equations (32) and (35) were investigated by using an approximate method and also by calculations on an analogue computer. Since each approach involves a knowledge of the asymptotic behaviour this will be investigated first.

6.1. Asymptotic Behaviour

G, ξ and θ are defined by the relations

$$\left.\begin{aligned} g &= \eta - \delta + G \\ \xi &= \eta - \delta \\ \text{and} \quad \phi_\rho &= 1 + \theta \end{aligned}\right\} \quad . \quad . \quad . \quad . \quad . \quad . \quad (39)$$

where δ is the constant which is such that, for η large, G is small (*see* the first of boundary conditions (38)).

Substitution from equation (39) into equations (32) and (35) gives, respectively,

$$\frac{d^2\theta}{d\xi^2} = -S_\infty (\xi + G) \frac{d\theta}{d\xi} \quad . \quad . \quad . \quad . \quad . \quad (40)$$

and

$$\frac{d^3G}{d\xi^3} + \xi \frac{d^2G}{d\xi^2} - 2\frac{dG}{d\xi} = \theta + \left(\frac{dG}{d\xi}\right)^2 - G\frac{d^2G}{d\xi^2} - \frac{1}{S_\infty(1+\theta)} \frac{d\theta}{d\xi} \frac{d^2G}{d\xi^2} - \\ - \frac{\theta^2}{1+\theta} - \frac{1}{1+\theta} \frac{d\phi_\mu}{d\xi} \frac{d^2G}{d\xi^2} + \frac{1-\phi_\mu+\theta}{1+\theta} \frac{d^3G}{d\xi^3} \quad . \quad (41)$$

In equation (40), G is neglected compared to ξ, so that the equation becomes

$$\frac{d^2\theta}{d\xi^2} = -S_\infty \xi \frac{d\theta}{d\xi} \quad . \quad . \quad . \quad . \quad . \quad (42)$$

In equation (41) it is supposed that G, θ, $(1-\phi_\mu)$ and their derivatives are small and only terms of the first order are retained. Thus the equation becomes

$$\frac{d^3G}{d\xi^3} + \xi \frac{d^2G}{d\xi^2} - 2\frac{dG}{d\xi} = \theta. \quad . \quad . \quad . \quad (43)$$

Equation (42) may be integrated to give

$$\frac{d\theta}{d\xi} = C_1 \, e^{-S_\infty \xi^2/2} \quad . \quad . \quad . \quad . \quad . \quad (44)$$

where C_1 is a constant.

Hence $$\theta = \phi_\rho - 1 = -\frac{\pi^{1/2} C_1}{2^{1/2} S_\infty^{1/2}} \operatorname{erfc} \frac{S_\infty^{1/2} \xi}{2^{1/2}} + C_2, \quad . \quad . \quad . \quad . \quad . \quad (45)$$

where $$\operatorname{erfc} x = \frac{2}{\pi^{1/2}} \int_x^\infty e^{-t^2} \, dt$$

and C_2 is a constant, which is not taken to be zero at this stage, although this implies that the second of boundary conditions (38) is not satisfied.

From equation (45), equation (43) can be written

$$\frac{d^3G}{d\xi^3} + \xi \frac{d^2G}{d\xi^2} - 2\frac{dG}{d\xi} = -\frac{\pi^{1/2}}{2^{1/2} S_\infty^{1/2}} C_1 \operatorname{erfc} \frac{S_\infty^{1/2} \xi}{2^{1/2}} + C_2. \quad . \quad (46)$$

Differentiating this equation twice gives

$$\frac{d^5G}{d\xi^5} + \xi \frac{d^4G}{d\xi^4} = -C_1 S_\infty \xi \, e^{-S_\infty \xi^2/2} \quad . \quad . \quad . \quad . \quad (47)$$

It follows that, when $s_\infty \neq 1$,

$$\frac{d^4G}{d\xi^4} = -\frac{C_1 S_\infty}{1-S_\infty} e^{-S_\infty \xi^2/2} + \text{constant} \times e^{-\xi^2/2},$$

which may be integrated three times to give

$$\frac{dG}{d\xi} = \frac{u}{u_\infty} - 1$$

$$= \frac{C_1 2^{1/2}\pi^{1/2}}{S_\infty^{1/2}(1-S_\infty)} i^2 \operatorname{erfc} \frac{S_\infty^{1/2}\xi}{2^{1/2}} - \frac{C_2}{2} + C_3 i^2 \operatorname{erfc} \frac{\xi}{2^{1/2}} + C_4(\xi^2+1), \quad . \quad (48)$$

where $i^n \operatorname{erfc} x = \int_x^\infty i^{n-1} \operatorname{erfc} t \, dt$,

with $i^0 \operatorname{erfc} x = \operatorname{erfc} x$, and C_3 and C_4 are constants. If the first of boundary conditions (38) is satisfied, then C_2 and C_4 are zero.

When $S_\infty = 1$,

$$\frac{d^4G}{d\xi^4} = -\frac{C_1}{2}\xi^2 e^{-\xi^2/2} + \text{constant} \times e^{-\xi^2/2},$$

so that the asymptotic behaviour is not very different from that when $S_\infty \neq 1$ and will not be considered further herein.

6.2. Property Values

Equations (32) and (35) were solved on the A.R.L. analogue computer for a range of values of M when the ejected gas was hydrogen, helium, steam or carbon dioxide; but, before considering these solutions, the property values used in the calculations, and also in the subsequent solution of equation (36), will be discussed. They are given in Table I.

The values of μ_1, k_1 and D_{12} for the gases under consideration were obtained from Refs. 6 and 7 for a pressure of one atmosphere and a temperature of 0°C, except for steam*. These values were used to give values of $\phi_{\mu 12}$, ϕ_{k12} and S_∞ for each gas, where

$$\phi_{\mu 12} = \mu_1/\mu_2 \quad \text{and} \quad \phi_{k12} = k_1/k_2.$$

*For steam the property values, and also the reference property values of air, were evaluated at 100°C, except that, in evaluating $\phi_{\mu 12}$, μ_2 was erroneously taken as the coefficient of viscosity of air at 0°C. This gave a value of 0·743 for μ_1/μ_2. According to Ref. 8 (Table 2V-3) the value of this ratio with both quantities evaluated at 100°C is 0·605. It is believed that the effects of this error are small.

TABLE I
PROPERTY VALUES

Property	*Hydrogen*	*Helium*	*Steam*	*Carbon Dioxide*
m	14·48	7·328	1·608	0·658
S_∞	0·216	0·254	0·600	0·957
$\varphi_{\mu 12}$	0·4927	1·077	0·743	0·802
A	0·4145	1·0	0·3203	1·3817
B	1·1708	0	0·6797	–0·3817
C	–0·5845	0	0	0
φ_{k12}	7·13	6·23	0·7663	0·614
ϕ_{C12}	14·13	5·17	2·005	0·829
$(Pr)_\infty$	0·72	0·72	0·72	0·72
Range of M	0 to 0·4	0 to 0·6	0 to 1·0	0 to 1·6

Reference 6 also gives the variation with concentration of the coefficient of viscosity of a mixture of hydrogen and air and of a mixture of oxygen and carbon dioxide. It was found that, in the former case, the values could be closely approximated to by

$$\phi_\mu = A + B\phi_\rho + C\phi_\rho^2, \quad . \quad . \quad . \quad . \quad . \quad (49)$$

the relationship between ϕ_ρ and w being given by equation (28). The values of A, B and C are given in Table I. In the latter case a linear approximation was found to be satisfactory. In view of this, and because of the dearth of other experimental results, it was assumed that a linear formula could also be used for mixtures of air and carbon dioxide and of air and steam. The values of the constants A and B were chosen to give the correct values of ϕ_μ for pure air and pure foreign gas and are included in Table I. The coefficients of viscosity of helium and air were considered to be sufficiently close for it to be assumed that the viscosity of a mixture of them is independent of concentration.

For mixtures of hydrogen and air and of helium and air, the formulae given in Refs. 3 and 2 were used respectively to give the dependence of ϕ_k on ϕ_ρ. For mixtures of steam and air and of carbon dioxide and air, the variation of ϕ_k with ϕ_ρ is much smaller and the simple formula

$$\phi_k = 1 + \frac{m(\varphi_{k12} - 1)(1 - \phi_\rho)}{m - 1}$$

was used. This formula gives the correct values of ϕ_k for pure air and pure foreign gas, when $\phi_\rho = 1/m$ (*see* equation (28)).

6.3. Calculations on the Analogue Computer

The calculations on the analogue computer were commenced at $\eta = 0$ with prescribed starting values for g, $dg/d\eta$, $\phi_\mu d^2g/d\eta^2$, ϕ_ρ and $d\phi_\rho/d\eta$. The starting values of the first two functions were obtained from the first and third of equations (37). The other starting values were determined as follows.

(*i*) Starting values of ϕ_ρ and $\phi_\mu\, d^2g/d\eta^2$ were guessed and the second of equations (37) was solved for $d\phi_\rho/d\eta$.

(*ii*) The solution curve of $dg/d\eta$ for these starting values was then obtained. In general it was found that, for large values of η, $dg/d\eta$ tended to either $\pm\infty$ at a rate which appeared to be consistent with the last term in equation (48). The starting value of $\phi_\mu\, d^2g/d\eta^2$ was then adjusted until the divergence of $dg/d\eta$ towards $\pm\infty$ was delayed to as large a value of η as possible.

(*iii*) The solution curve of ϕ_ρ was then obtained. In general it was found that, for η large, ϕ_ρ tended to a constant other than one in accordance with equation (45).

(*iv*) The starting value of ϕ_ρ was then adjusted to a value that was estimated to be such that, for η large, ϕ_ρ would tend to one. A new starting value of $d\phi_\rho/d\eta$ was obtained from the second of equations (37).

Procedures (*ii*), (*iii*) and (*iv*) were then repeated in turn until a solution was obtained that satisfied the two boundary conditions at $\eta=\infty$ with acceptable accuracy.

Typical solution curves that were obtained in the final stages of calculation for the case of helium injection with $M=0{\cdot}3$ are shown in Fig. 1. The figure shows the effect of making a small change to the starting value of $\phi_\mu\, d^2g/d\eta^2$, keeping the starting values of the other functions the same.

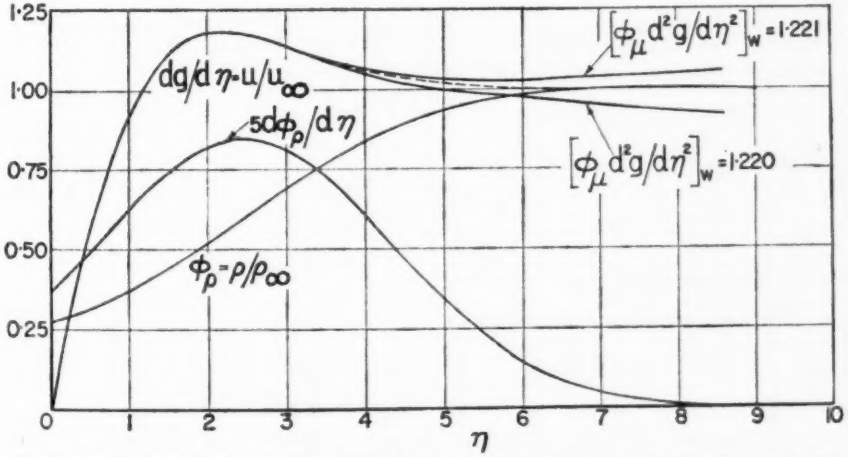

FIGURE 1. Typical solution curves obtained on an analogue computer showing the effect of a small change in the starting value of $\phi_\mu\, d^2g/d\eta^2$, keeping the starting values of ϕ_ρ, $d\phi_\rho/d\eta$, g and $dg/d\eta$ the same. Helium injection, $M=0{\cdot}3$.

The values of ϕ_ρ (and $d\phi_\rho/d\eta$) are not affected and it is seen that the boundary condition at $\eta=\infty$ on ϕ_ρ is satisfied accurately (to within approximately 0·001).

The values of $dg/d\eta$ are affected little for $\eta<3$, but for $\eta>3$ the two curves diverge, one tending to $+\infty$ and the other to $-\infty$. Thus the correct starting value of $\phi_\mu\, d^2g/d\eta^2$ can be determined very accurately, but the correct values for $dg/d\eta$ for $\eta>3$ are left in doubt. It was found that these values could be determined with acceptable accuracy by using the knowledge of the asymptotic behaviour of the solution (*see* Section 6.1). The values of $dg/d\eta$ obtained in this way are shown by the dotted curve in Fig. 1.

This instability in the values of $dg/d\eta$ for η large is typical. It became more pronounced as M was increased and imposed an upper limit on the value of M for which solutions could be obtained for a particular gas.

The results obtained on the analogue computer, corrected for η large, as already explained, are given in Figs. 2, 3 and 4.

6.4. Exact Solutions for Special Cases

Equations (32) and (35) may be solved exactly for two special cases:—

(*i*) for M small

and (*ii*) for $m=1$ and M arbitrary.

In both cases ϕ_ρ and ϕ_μ may be taken as unity in equation (35) so that it becomes

$$\left(\frac{dg}{d\eta}\right)^2 - g\frac{d^2g}{d\eta^2} = 1 + \frac{d^3g}{d\eta^3}\,, \qquad . \quad . \quad . \quad (50)$$

which is the familiar equation for the non-dimensional stream function for stagnation-point boundary-layer flow, solutions of which are available.

For M small, equation (32) is solved for ϕ_ρ to give

$$\phi_\rho - 1 = D\int_\infty^\eta \exp\left(-S_\infty \int_0^\xi g(t)\,dt\right) d\xi, \qquad . \quad . \quad (51)$$

where D is a constant.

From this equation it follows that

$$\lim_{M\to 0}\left[\frac{\rho-\rho_w}{\rho_\infty-\rho_w}\right] = \frac{\displaystyle\int_0^\eta \exp\left(-S_\infty\int_0^\xi g(t)\,dt\right)d\xi}{\displaystyle\int_0^\infty \exp\left(-S_\infty\int_0^\xi g(t)\,dt\right)d\xi}. \qquad . \quad . \quad (52)$$

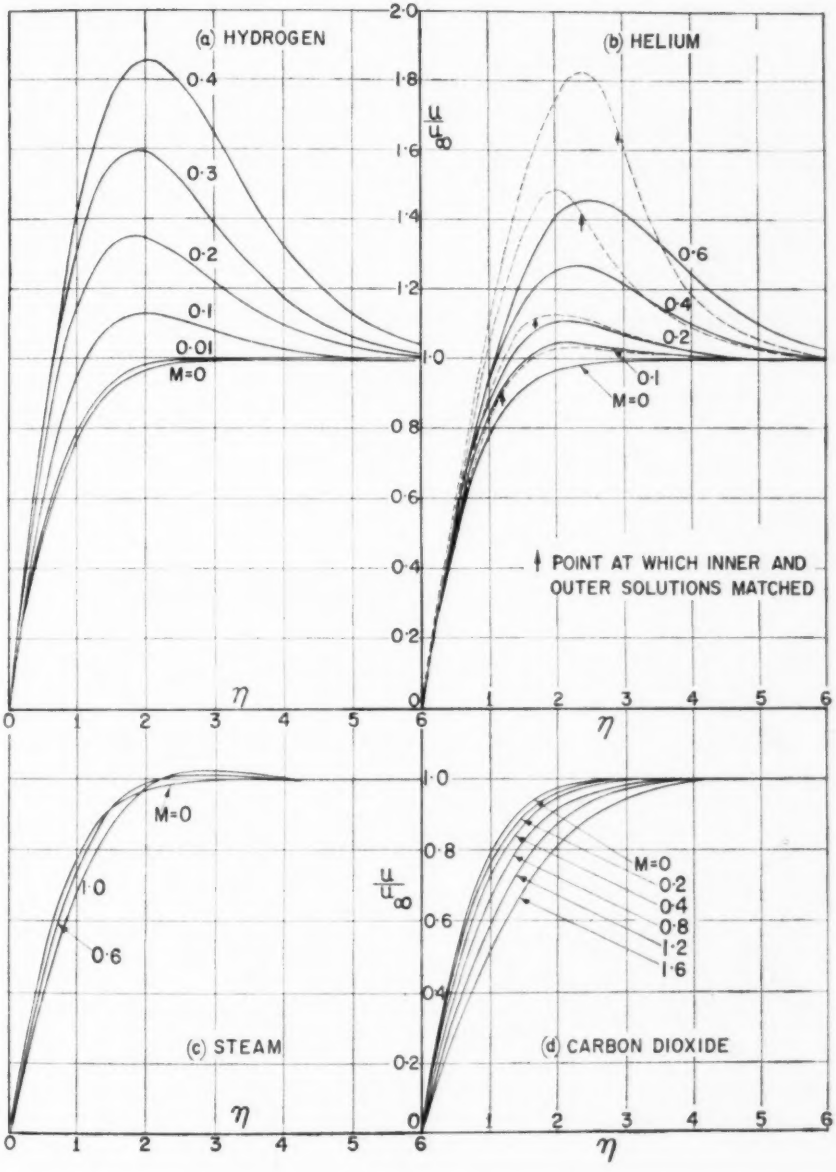

FIGURE 2. Boundary layer velocity profiles for injection of various gases.

———— Analogue solutions.

— — — — Approximate solutions (*see* Section 6.5).

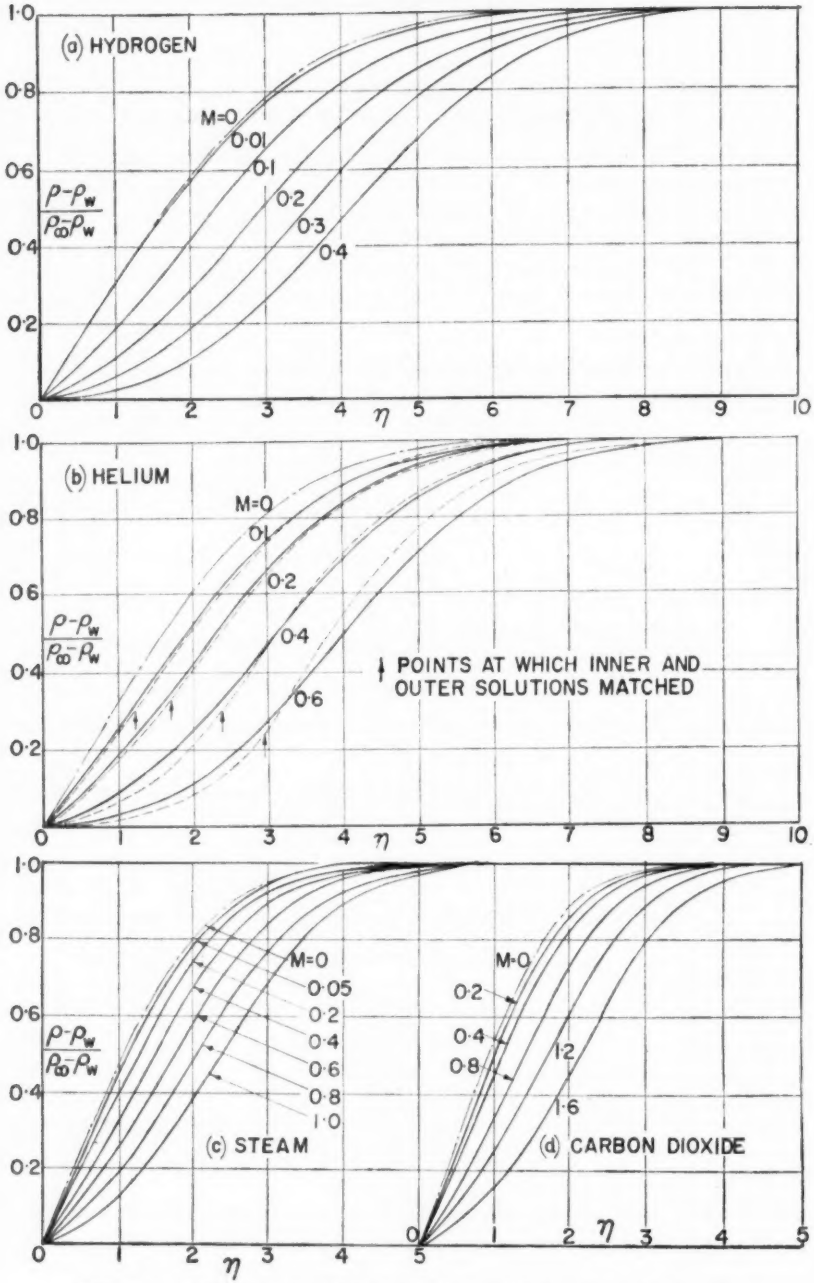

FIGURE 3. Boundary layer density profiles for injection of various gases.
———— Analogue solutions.
—·—·— Exact solution for limit $M \to 0$.
— — — — Approximate solutions (*see* Section 6.5).

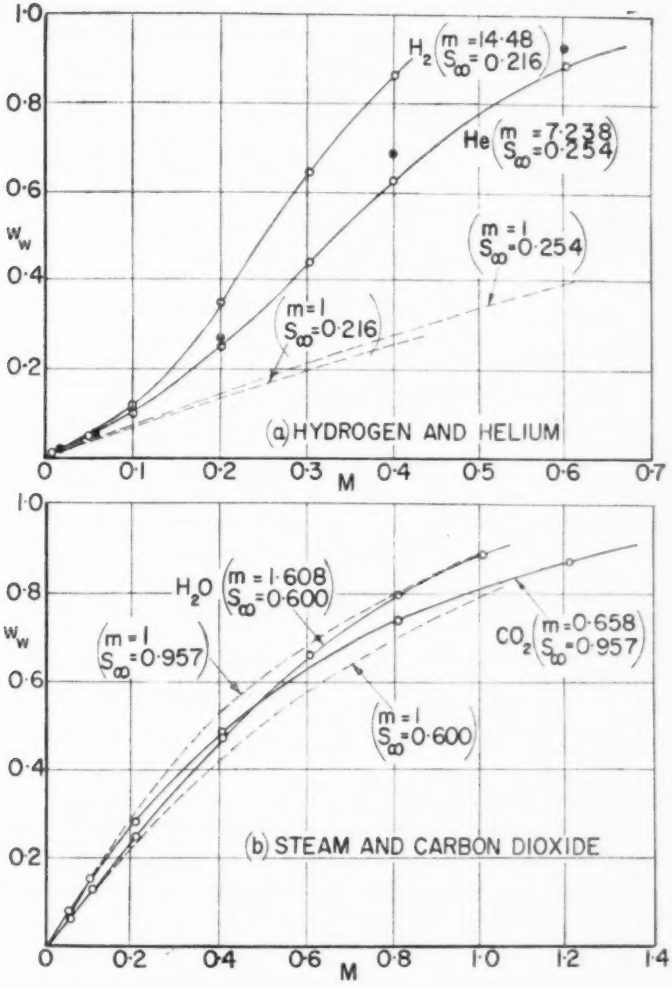

FIGURE 4. Variation of concentration at wall with mass injection parameter for injection of various gases.

—O— Analogue solutions.

— — — — Exact solutions for $m = 1$.

● Approximate theory for helium injection (*see* Section 6.5).

The values of g for zero fluid injection were obtained from Ref. 9, and equation (52) was evaluated for the values of S_∞ appropriate to the gases being considered. The results are included in Fig. 3.

For $m=1$ and M arbitrary, equation (28) is used to transform equation (32) into one for w, the limit $m \longrightarrow 1$ being taken after the transformation. Thus

$$\frac{d^2w}{d\eta^2} + S_\infty g \frac{dw}{d\eta} = 0, \quad . \quad . \quad . \quad . \quad . \quad . \quad (53)$$

the solution of which is

$$w = E \int_\infty^\eta \exp\left(-S_\infty \int_0^\xi g(t)\, dt \right) d\xi, \quad . \quad . \quad (54)$$

where E is a constant. Boundary conditions (37) yield, at $\eta=0$,

$$\left.\begin{aligned} g &= -M \\ dw/d\eta &= -MS_\infty (1-w) \\ \text{and} \quad dg/d\eta &= 0 \end{aligned}\right\} \quad . \quad . \quad . \quad . \quad . \quad (55)$$

From the second of these, and from equation (54), it follows that

$$w_w = \frac{MS_\infty \int_0^\infty \exp\left(-S_\infty \int_0^\xi g(t)\, dt \right) d\xi}{1 + MS_\infty \int_0^\infty \exp\left(-S_\infty \int_0^\xi g(t)\, dt \right) d\xi} \quad . \quad . \quad . \quad (56)$$

where w_w is the concentration at the wall.

The solutions of equation (50), subject to boundary conditions (55), are given in Ref. 10. These, together with the same values of S_∞ as used in the analogue calculations, were substituted into equation (56) to give the dependence of w_w on M. The results are included in Fig. 4.

6.5. Approximate Method of Solution when $\phi_\mu \equiv 1$

An approximate method of solving equations (32) and (35) when $\phi_\mu \equiv 1$ was also investigated. It consists of matching, at a point within the boundary layer, the asymptotic solution derived in Section 6.1 with a solution which is valid near the wall. For η small, put

$$g = -mM + h$$

$$\text{and} \quad \phi_\rho = \phi_{\rho w} + l.$$

It is supposed that h, l and their derivatives are small and only terms which are of the first order in these quantities are retained in equations (32) and (35).

Thus these equations become, respectively,

$$\frac{d^2l}{d\eta^2} = mMS_\infty \frac{dl}{d\eta}$$

and $$\frac{d^3h}{d\eta^3} - mM\phi_{\rho w}\frac{d^2h}{d\eta^2} + 1 = 0.$$

The solution of these equations which satisfies boundary conditions (37) is

$$g = -mM + h = -mM + F(1 + a\eta - e^{a\eta}) + \frac{\eta^2}{2a} \quad . \quad . \quad . \quad (57)$$

and $$\phi_\rho = \phi_{\rho w} + l = \frac{1}{m} + \left(\phi_{\rho w} - \frac{1}{m}\right) e^{b\eta}, \quad . \quad . \quad . \quad (58)$$

where $a = mM\phi_{\rho w}$, $b = mMS_\infty$, and F is a constant.

From equations (45) and (48), the asymptotic solution which satisfies boundary conditions (38) is

$$\phi_\rho = 1 - \frac{\pi^{1/2}C_1}{2^{1/2}S_\infty^{1/2}} \operatorname{erfc} \frac{S_\infty^{1/2}\xi}{2^{1/2}} \quad . \quad . \quad . \quad . \quad . \quad . \quad (59)$$

and $$g = \xi - \frac{2\pi^{1/2}}{S_\infty(1 - S_\infty)} C_1 i^2 \operatorname{erfc} \frac{S_\infty^{1/2}\xi}{2^{1/2}} - 2^{1/2}C_3 i^2 \operatorname{erfc} \frac{\xi}{2^{1/2}} \quad . \quad (60)$$

It is supposed that this solution is valid for $\xi > 0$, *i.e.* for $\eta > \delta$ (*see* equation (39)), and that the solution given by equations (57) and (58) is valid for $\eta < \delta$. In matching the solutions at $\eta = \delta$, there are five disposable constants, δ, $\phi_{\rho w}$, C_1, C_3 and F. These were determined by requiring ϕ_ρ, $d\phi_\rho/d\eta$, g, $dg/d\eta$ and $d^2g/d\eta^2$ to be continuous at $\eta = \delta$.

The boundary layer velocity and density profiles were calculated for helium injection using the property values given in Table I. The results are compared with the corresponding analogue ones in Figs. 2, 3 and 4. The comparison provides a check on the accuracy of the approximate theory, as in both sets of calculations ϕ_μ was taken to be unity.

7. Solution of Energy Equation

The energy equation (36) can be written in the form

$$\frac{d^2\phi_T}{d\eta^2} + r(\eta)\frac{d\phi_T}{d\eta} = 0, \quad . \quad . \quad . \quad . \quad (61)$$

where $$r(\eta) = \frac{1}{\phi_k}\left[\frac{d\phi_k}{d\eta} + (Pr)_\infty \phi_\rho \phi_c \left(g + \frac{1}{S_\infty \phi_\rho}\frac{d\phi_\rho}{d\eta}\right) + \frac{(Pr)_\infty}{S_\infty}\frac{(1 - \phi_{c12})}{(m-1)\phi_\rho}\frac{d\phi_\rho}{d\eta}\right] \quad . \quad (62)$$

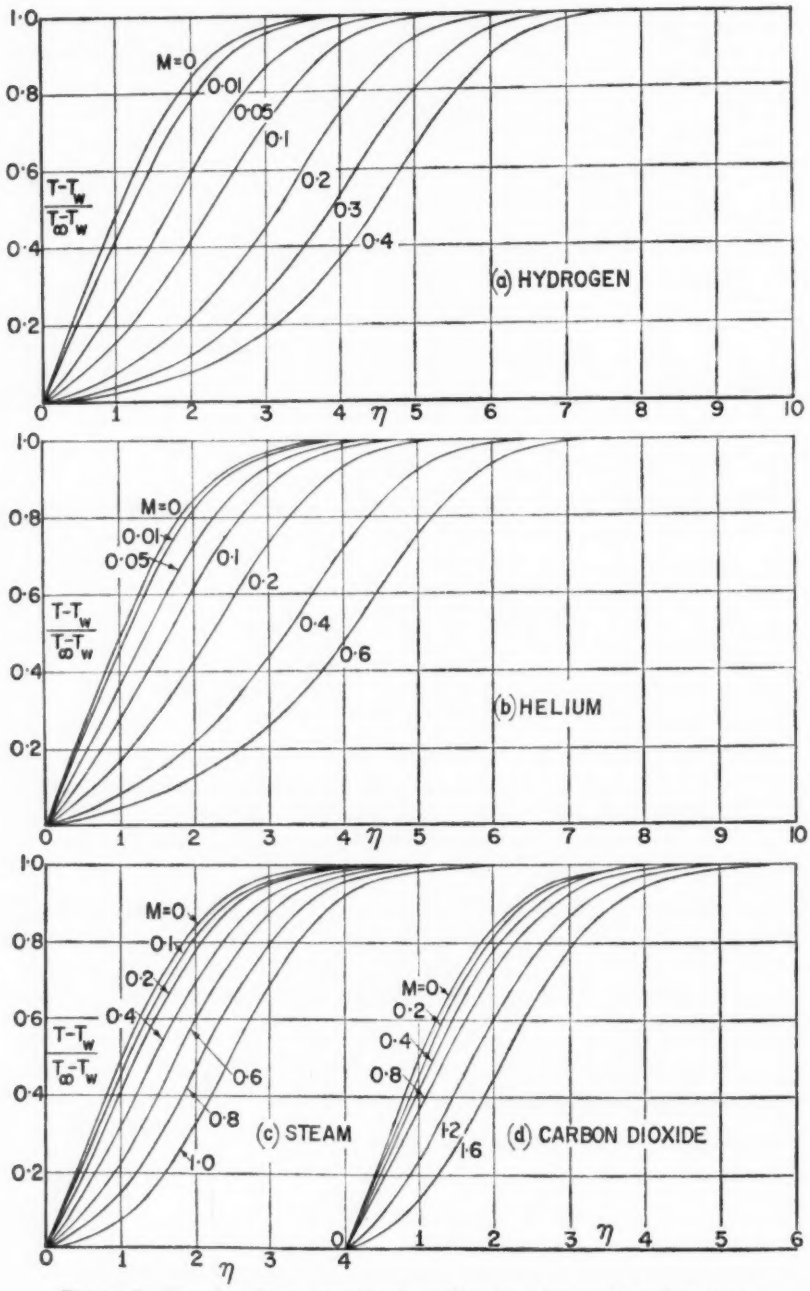

FIGURE 5. Boundary layer temperature profiles for injection of various gases.

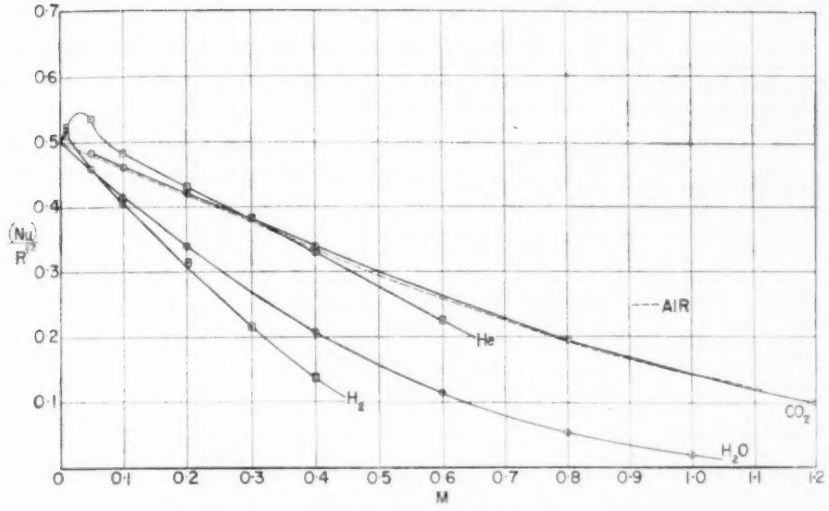

FIGURE 6. Variation of heat transfer rate with mass injection parameter for various gases.

The solution of equation (61) which satisfies the boundary conditions (37) and (38) can be expressed in the form

$$\frac{T-T_w}{T_\infty-T_w}=\frac{\int_0^\eta \exp\left(-\int_0^\xi r(t)\,dt\right)d\xi}{\int_0^\infty \exp\left(-\int_0^\xi r(t)\,dt\right)d\xi} \quad . \quad . \quad . \quad . \quad . \quad (63)$$

The Nusselt number, (Nu), is defined by

$$(Nu)=\frac{Qx}{k_\infty(T_\infty-T_w)} \quad . \quad . \quad . \quad . \quad . \quad . \quad (64)$$

and it follows from equations (13), (20) and (63) that

$$\frac{(Nu)}{R^{1/2}}=\frac{\phi_{kw}\,(dT/d\eta)_w}{T_\infty-T_w}=\frac{\phi_{kw}}{\int_0^\infty \exp\left(-\int_0^\xi r(t)\,dt\right)d\xi} \quad . \quad . \quad (65)$$

Equations (62), (63) and (65) were evaluated numerically, using the results of the analogue calculations, and the resulting values are given in Figs. 5 and 6.

8. Discussion of Results

To test the accuracy of the analogue computer, the values of u/u_∞ that were obtained for $M=0$ are compared in Fig. 7 with the exact values obtained from Ref. 9. The agreement is seen to be satisfactory.

The boundary layer velocity and density profiles are shown in Figs. 2 and 3. A number of their features can be accounted for in terms of the asymptotic solution derived in Section 6.1. For each of the gases under consideration, $S_\infty < 1$ (*see* Table I), so that it follows from equations (45) and (48) that, for η large,

$$\left.\begin{aligned} \frac{u}{u_\infty} &\simeq 1 + \frac{C_1 2^{1/2}\pi^{1/2}}{S_\infty^{\,1/2}(1-S_\infty)}\, i^2\,\mathrm{erfc}\,\frac{S_\infty^{\,1/2}(\eta-\delta)}{2^{1/2}} \\ \text{and}\quad \phi_\rho &\simeq 1 - \frac{C_1\pi^{1/2}}{2^{1/2}S_\infty^{\,1/2}}\,\mathrm{erfc}\,\frac{S_\infty^{\,1/2}(\eta-\delta)}{2^{1/2}} \end{aligned}\right\} \quad . \quad . \quad . \quad (66)$$

Thus the density and velocity profiles will be thicker the smaller the value of S_∞. This feature is apparent in the figures.

When $m > 1$ the densities within the boundary layer will be less than the free-stream density. Thus, from equations (66), C_1 will be positive and the maximum value of u/u_∞ will exceed unity. Fig. 2 shows this feature and that it is more pronounced the larger the values of m and M.

Figure 4 gives the dependence of w_w on M for the various gases and includes results derived by the method of Section 6.4 for $m=1$ and the same values of S_∞ as used in the analogue calculations. It is seen that for the light gases it is essential to take the correct value of m to obtain reliable values of w_w. If it is assumed that $m=1$, then the predicted values of w_w are too small, particularly for the larger values of M. For the heavier gases, the assumption that $m=1$ leads to smaller, although significant, errors in w_w.

Figure 4 also shows that, for all values of M, w_w increases with S_∞ for m fixed ($=1$). This is to be expected as an increase in $S_\infty = \nu_\infty/D_{12\infty}$ corresponds to a decrease in the diffusion coefficient $D_{12\infty}$.

The results obtained for helium by the approximate theory described in Section 6.5 are included in Figs. 2, 3 and 4. The points in the boundary layer where the outer and inner solutions were matched are indicated. Fig. 2 shows that the approximate theory gives unreliable values of u/u_∞ for the larger values of M. A possible reason for this is that the assumption in the approximate theory that u/u_∞ is small over the inner portion of the boundary layer does not hold.

The values of $(\rho-\rho_w)/(\rho_\infty-\rho_w)$ given by the approximate method are seen to be in closer agreement with the analogue results (Fig. 3), as are the values of w_w (Fig. 4).

The temperature profiles are shown in Fig. 5 and a noticeable feature is the progressive decrease in the temperature gradient at the wall as M is increased.

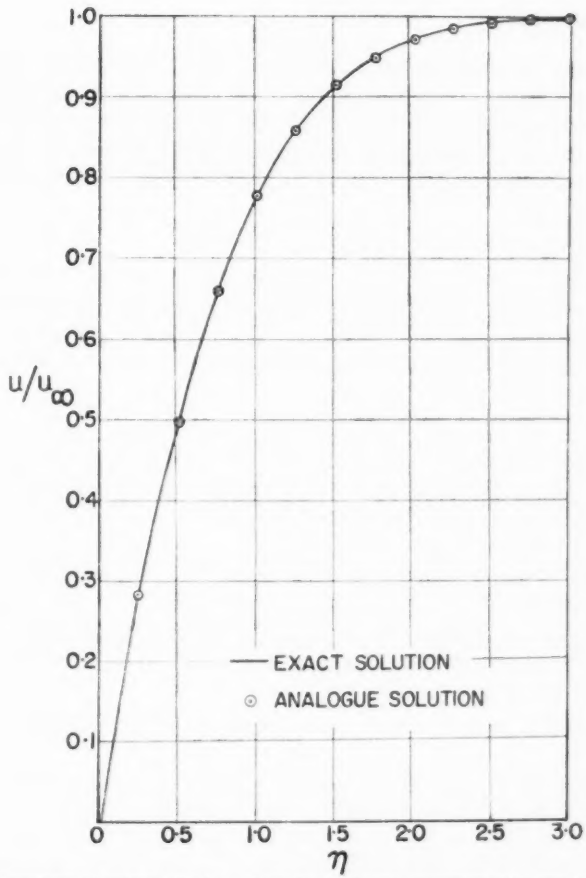

FIGURE 7. Comparison of values of u/u_∞ given by analogue computer with exact values. $M=0$.

The values of $(Nu)/R^{1/2}$ are given in Fig. 6, which includes results for air injection obtained from Ref. 10, corrected to a Prandtl number of 0·72. Two factors determine the value of $(Nu)/R^{1/2}$. These are the thermal conductivity of the gas in contact with the wall and the temperature gradient there (*see* equation (65)). Both steam and carbon dioxide have lower thermal conductivities than air (*see* Table I) so that in these cases both the thermal conductivity and the temperature gradient decrease as M is increased. Thus, so does $(Nu)/R^{1/2}$. Hydrogen and helium, however, have thermal conductivities considerably larger than air, so that for these gases the thermal conductivity at the wall increases steadily as M is increased. Fig. 6 shows that this effect outweighs the effect of decreasing temperature gradient for small values of M. Thus $(Nu)/R^{1/2}$ increases with M at first and then decreases.

The figure shows that the ejection of hydrogen reduces the heat transfer rate the most, and that steam is the next most effective of the substances investigated.

9. Possible Extension

The effects of ionisation and dissociation of the ejected gas have not been considered in the present investigation. Since a very large quantity of heat is absorbed in these processes, it seems likely that account should be taken of them in determining the best substance to use for mass transfer cooling. It may prove practicable to extend the present method of analysis to include these effects.

Acknowledgments

Acknowledgment is made to the Chief Scientist, Australian Defence Scientific Service, Department of Supply, Melbourne, for permission to publish this paper. Acknowledgment is also made to Messrs. D. E. Hatton and M. B. Mackey for setting up the equations on the analogue computer and to Dr. W. W. Wood for helpful discussions.

References

1. Hartnett, J. P. and Eckert, E. R. G. Mass-Transfer Cooling in a Laminar Boundary Layer with Constant Fluid Properties. *Transactions of the American Society of Mechanical Engineers*, Vol. 79, p. 247, February 1957.
2. Hoshigaki, H. and Smith, H. J. Axisymmetric Stagnation Point Mass-Transfer Cooling. Lockheed TR LMSD-48381, 1959.
3. Eckert, E. R. G., Schneider, P. J., Hayday, A. A. and Larson, R. M. Mass-Transfer Cooling of a Laminar Boundary Layer by Injection of a Light Weight Foreign Gas. *Jet Propulsion*, Vol. 28, p. 34, January 1958.
4. Eckert, E. R. G. and Drake, R. M. *Heat and Mass Transfer*. Second Edition. McGraw-Hill, 1959.
5. Stewartson, K. Correlated Incompressible and Compressible Boundary Layers. *Proc. Roy. Soc.* A 200, p. 84, December 1949.
6. *International Critical Tables*. McGraw-Hill, 1926-30.
7. Smith, J. W. Effect of Diffusion Fields on the Laminar Boundary Layer. *Journal of the Aeronautical Sciences*, Vol. 21, p. 154, March 1954.
8. Gray, D. E. (Editor). *American Institute of Physics Handbook*. McGraw-Hill, 1957.
9. Goldstein, S. (Editor). *Modern Developments in Fluid Dynamics*. Oxford University Press, 1938.
10. Brown, W. B. and Donoughe, P. L. Tables of Exact Laminar Boundary-Layer Solutions when the Wall is Porous and Fluid Properties are Variable. N.A.C.A. T.N. 2479, September 1951.

The Elastic Stress Concentration Factors in Shouldered Shafts

PART I: Shafts Subjected to Torsion

I. M. ALLISON

(*Department of Civil and Municipal Engineering, University College, London*)

SUMMARY: The photoelastic "stress freezing" technique has been employed to evaluate the elastic stress concentration factors associated with the fillet blend radius in a number of shouldered shafts. The full range of practical sizes of blend radius and depth of shoulder has been examined. Comprehensive results for the shaft subjected to torsion, pure bending and axial load are given in this (Part I) and in two subsequent papers (Parts II and III).

The accuracy of the graphs of stress concentration factors is better than six per cent. Comparison has been made with the existing theoretical and experimental results for each mode of loading. The results of an investigation into the limiting value of the stress concentration factor (for a particular shoulder radius) as the depth of the shoulder is increased to infinity are included in Part III.

1. Introduction

A designer is often required to choose a suitable blend radius at a change in the section of a cylindrical shaft which may be subjected to large static or alternating loads. Although other considerations, such as the notch sensitivity of the shaft material in the case of alternating load, may influence the design, a knowledge of the elastic stress concentration factors (s.c.f.) associated with different root radii is of considerable aid in the selection of the most suitable radius for a particular purpose. This applies especially in examples, such as a locating shoulder, where it is an advantage to use the smallest possible root radius.

Theoretical and experimental stress concentration factors associated with a number of particular blend radii are available, but the information from different sources is conflicting and it does not cover the full range of practical dimension parameters.

The investigation described in this series of three papers forms part of a programme initiated by the Structures Committee of the Royal Aeronautical Society in order to provide complete information about the peak elastic stresses associated with a number of different types of geometric stress raiser. In particular, the present

Received January 1961.

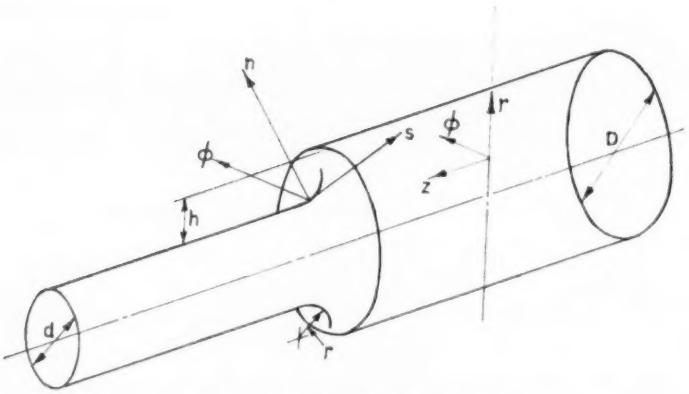

FIGURE 1. Shouldered shaft notation.

work is intended to provide systematic data for the full range of shaft diameters and shoulder root radii which would be likely to occur in practice. Tests covering this range of size parameters were carried out for three different forms of applied load, namely, torsion, bending and axial load, and each of these will be described separately. Since much of the experimental procedure is common to all the forms of loading, a general description of the method is presented first. The problem involves a three-dimensional stress system and has been approached by the photoelastic "stress-freezing" technique.

NOTATION (*See* Fig. 1)

D	large diameter of shaft
d	small diameter of shaft
r	shoulder radius
h	shoulder depth (thus $D=d+2h$)
r, ϕ, z	cylindrical polar co-ordinates
z	axis of shaft
P, Q, R	principal stresses
p, q, r	directions of principal stresses
n	direction of the normal to the shaft surface
$\widehat{ss}$	normal stress tangential to the surface in a direction s
$\widehat{s\phi}$	cross-radial shear stress acting on the plane of the cross section

The stress concentration factors are based on the nominal stress in the smaller diameter of the shouldered shaft. The factor K used throughout this paper is therefore defined as

$$K = \frac{\text{peak stress in the component}}{\text{maximum stress in a shaft of the smaller diameter under the same loading conditions}}.$$

2. Method of Tests

2.1. Manufacture and Loading of Models

The range of photoelastic models tested is shown in Table I.

TABLE I

	$h/D=0{\cdot}05$ $d/D=0{\cdot}9$	0·1 0·8	0·2 0·6	0·25 0·5	0·3 0·4	0·4 0·2	0·475 0·05	
$h/r=$								
0·5	×	×						
1·0	×	×	×			×		8 in. long models
2·0		×	×					
3·0	NP	×				×		
4·0	NP		×			×		
5·0				T				
6·67			×					10 in. long models
7·5					×			
15·0					×			
95·0							×	

T Torsion test only.
NP Photoelastic test not practicable.

The models were machined from oversize cylindrical castings of Araldite B, hot-setting resin, and an annealing cycle was carried out both before and after rough machining. An accuracy of $\pm 0{\cdot}002$ in. was maintained in the dimensions of the finished models, and the initial casting stress was never permitted to exceed one fringe per inch (*i.e.* about 3 per cent of the peak stress).

With the exception of the shaft having dimensions specified by the parameters $h/r=95$, $h/D=0{\cdot}475$, all the models were made from single castings, the overall dimensions being chosen so that the end effects of the loading system should not disturb the fringe pattern in the vicinity of the shoulder.

The minimum convenient size of shoulder root radius which may be examined photoelastically is limited to 0·05 in., giving, for the particular model just mentioned, values of $D=10$ in. and $d=0{\cdot}5$ in. for the larger and smaller diameters of the shaft respectively. It was known to be impossible to make such a model from one casting and still maintain the initial stress level below one fringe per inch.

Each of the models of this type was made from two castings, the manufacture and subsequent loading cycle being as described in Section 6.

In the original programme, models having dimension parameters $h/r=3$, $h/D=0{\cdot}05$ and $h/r=4$, $h/D=0{\cdot}05$ were specified. However, in these cases the choice of $D=1{\cdot}5$ in. gives values of r of 0·025 in. and 0·0188 in. respectively. It was decided that these shoulder radii were too small to be produced sufficiently accurately or to permit accurate measurements of the s.c.f., and the results for these models were obtained by extrapolation of the graphs.

A special loading frame which had been used in a previous part of the programme[1] was available for loading the models, which could be subjected to tension, compression, bending or torsion by using different arrangements of links and dead weights.

2.2. Peak Stress Measurement

After freezing, slices were cut from the models and placed in an immersion fluid, having the same refractive index as Araldite, for examination in a standard photoelastic bench. The peak stress was found to lie on the surface of the shaft and its magnitude was obtained for all types of loading by using the method outlined in the following paragraph.

The stress difference was measured at a number of points in the slice below the shaft surface and the peak stress was obtained by graphical extrapolation to the point of maximum stress on the boundary. It is necessary to adopt this extrapolation method because of the difficulty in locating the photoelastic "fringe" on the extreme boundary. The presence of a "time-edge stress," owing to the absorption of water in the surface of the photoelastic model, presents further difficulties in the accurate measurement of the surface stress. Optical measurements made using the Sénarmont method gave the extrapolated value of the boundary stress to an accuracy of 0·5 fringes per inch, while the position of points on the model was measured with a travelling microscope to an accuracy of $\pm 0{\cdot}001$ in. Measurements could not be made within less than 0·01 in. of the boundary, owing to the curvature of the shaft surface, and the extrapolation over this distance is estimated to give an accuracy in the peak stress measurement of ± 4 per cent.

2.3. Measurement of Nominal Stress

No attempt was made to measure the load applied to the model, the maximum stress in the smaller diameter of shaft being obtained in the uniform stress region lying between the disturbances caused by the shoulder and the loading pins. This method had two advantages in that it provided a check that the end conditions were not affecting the stress distribution around the concentration and it also dispensed with the necessity for finding the fringe value for each model. The maximum uniform stress was measured to an accuracy of ± 2 per cent, giving an overall accuracy of ± 6 per cent for the final s.c.f.

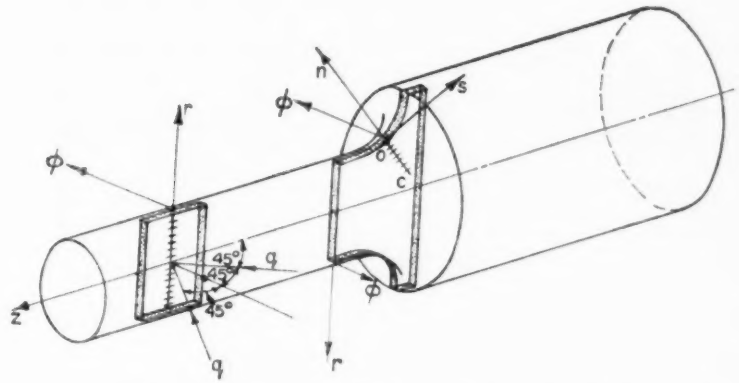

FIGURE 2. Slices cut from the frozen photoelastic models.
The direction of viewing q is inclined at 45° to the plane of the slice for the torsion models and is perpendicular to the plane of the slice for the tension and the bending models.

3. Torsion Tests

3.1. Stress Pattern in Torsion

The maximum stress on any cross section of the shaft is the $\widehat{s\phi}$ shear stress at the surface. This shear stress may be represented by principal stresses P and Q, lying in the tangent plane to the surface and inclined at 45° to the axis of the shaft such that $P = -Q$ (Fig. 2).

3.2. Peak Stress Measurement

The peak surface stress may be obtained from any longitudinal slice containing a diameter of the shaft (Fig. 2). The slice was cut by hand and its surface was finished with fine emery paper. To measure the true principal stress difference it is necessary to view the slice obliquely at an angle of 45° to the normal direction. For convenience the slice was rotated in a model holder until OC, the normal to the boundary passing through the peak of the concentration, coincided with the microscope traverse. Observations were then made at $+45°$ and at $-45°$ to obtain $(P-R)$ and $(Q-R)$, the tensile and compressive principal differences, respectively. A similar series of observations was made for O', the corresponding concentration on the opposite boundary of the slice, and the mean of the two tensile and two compressive results was plotted in fringes per inch against the distance from the shaft surface, the resulting curve being extrapolated to obtain the boundary stress. Taking the numerical mean of the four results eliminates the initial error in setting up the slice, any bending induced by the loading system and the time edge-stress effect. A typical extrapolation is shown in Fig. 3.

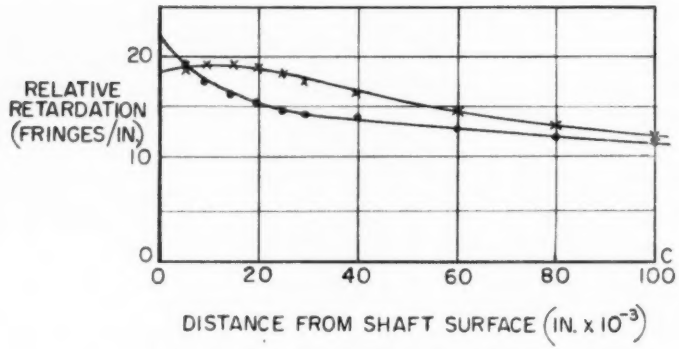

FIGURE 3. Typical torsion test results.
Relative retardation through an axial slice, along the line OC,
for oblique viewing at angles of incidence of $+45°$ and $-45°$.
× View at $+45°$ (tensile principal stress).
● View at $-45°$ (compressive principal stress).

3.3. UNIFORM STRESS MEASUREMENT

Measurements of the relative retardation on the principal planes, which are inclined at $+45°$ and $-45°$ to the plane of a longitudinal slice, were made at points along a diameter of the shaft. The results were plotted and extrapolated to the surface to obtain the maximum principal stress in the smaller diameter of the shouldered shaft.

3.4. RESULTS

Initially graphs of the s.c.f. K were plotted against the following parameters:—

h/r for constant h/D,

h/D for constant h/r,

h/d for constant r/d,

r/d for constant h/d,

and d/D for constant r/d.

All these curves must be smooth and continuous, and corresponding points on each curve must be consistent. The graphs were drawn to satisfy these conditions, while paying due regard to the experimental points, and the final curves of K against h/r and K against d/D are given in Figs. 4 and 5. The parameters specifying the dimensions of the "insert" model are considerably different from those of the other models tested. The results of this test were therefore not taken into consideration when determining the general shape of the curves given in Figs. 4 and 5.

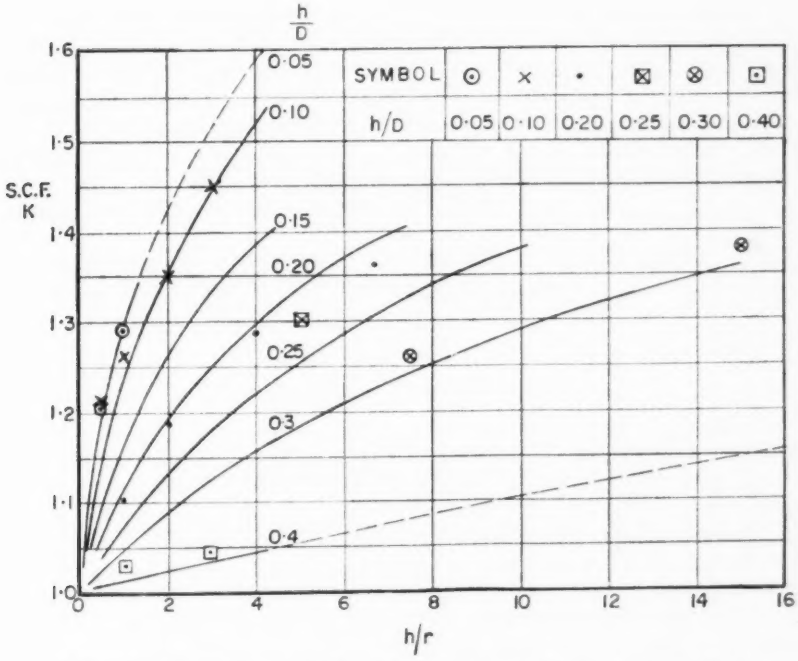

FIGURE 4. Stress concentration factor K against h/r for constant values of h/D.

For all the shouldered shafts tests, the curves within the range of the experimental results have been drawn as full lines. Results for $h/d = 0{\cdot}05$, outside the test range, were obtained by extrapolation and the curve in this region is shown as a broken line.

For given values of r and d, K increases initially, reaches a maximum value and then decreases as D is increased. This behaviour, which cannot be explained by any simple argument, also occurs in pure bending and to a lesser extent in the case of axial load.

For all three forms of loading and for all values of r/d, the results of the photoelastic tests inevitably predict an ultimate decrease in the s.c.f. as the value of d/D is decreased. This fall in the s.c.f. is still present even if the maximum estimated error band is put on the experimental points. Furthermore, were this trend not really present, it seems most unlikely that it should appear consistently throughout a relatively large number of photoelastic tests, conducted for a number of different forms of loading.

For the sake of completeness the results of the insert test have been included in Fig. 5, and a possible shape for the complete curve for $r/d = 0{\cdot}1$ is indicated by the chain-dotted line. It is interesting to note that the results of this test confirm

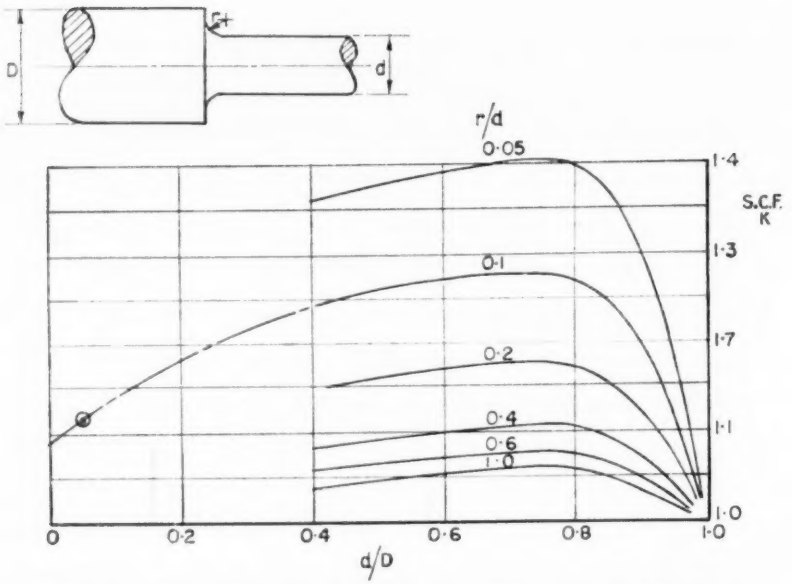

FIGURE 5. Stress concentration factor K against d/D for constant values of r/d.

the trend already observed, but it should be emphasised that this curve and the single test on which it depends are subject to larger possibility of error than the family of curves in the region $d/D > 0{\cdot}4$.

A more complete discussion of the significance of the fall in the s.c.f. for large values of D is given in Section 5.4 of Part II, describing the bending tests, which is to be published later. Fig. 5 also shows that the s.c.f. increases continuously as r/d is decreased.

The curves shown as full lines in Fig. 6 have been obtained, by interpolation*, from the combined results of Jacobsen[2] and Wiegand[3], which have been generally accepted as the design criteria for shouldered shafts subjected to torsion. These curves are in fair agreement with the results of the present tests (shown as chain-dotted lines) for high values of d/D, but show increasingly marked differences as d/D and r/d are decreased.

Jacobsen made use of an electrical analogy to obtain results, for $0{\cdot}005 < r/d < 0{\cdot}12$, which indicate that the s.c.f. is asymptotic to a limit as d/D decreases to zero, whereas the results of the present tests indicate that the factor reaches a maximum value and then decreases for d/D less than 0·7. The analogue requires

*The author is indebted to Miss M. E. Michael, of the Technical Department of the Royal Aeronautical Society, for the preparation of these curves.

the use of a steel "razor blade" model (shown in Fig. 7) having the same profile as a longitudinal section through the shouldered shaft. It is necessary for the thickness of the steel model to vary as the cube of the radial distance from the shaft axis. Since zero thickness is unobtainable in practice, Jacobsen used a model representing a 12 in. diameter shaft having a $1\frac{1}{2}$ in. diameter axial bore. The thickness of the model varied from 0·002 in. at the bore to 1 in. at the outer surface. Jacobsen mentions that it is difficult to maintain the profile of the cross section within the small limits required for the electrical tests.

The analogue used gives the twisting moment as $N = 2\mu I$, where I is the total current flowing through the model, and the shear stresses as

$$\widehat{r\phi} = \mu r\, \partial\Phi/\partial r$$

and $$\widehat{z\phi} = \mu r\, \partial\Phi/\partial z,$$

where $\partial\Phi/\partial r$ and $\partial\Phi/\partial z$ are the potential gradients in the appropriate directions on the surface of the model. The probes used for measuring the potential gradients were 0·1 in. apart (*cf.* 0·5 in. maximum shoulder root radius) and it was estimated that an error of up to 2 per cent was incurred by faulty probe contact. The potential difference across the probes was measured by a galvanometer, which had to be recalibrated immediately after each reading in order to obviate the effects of drift. The difference between the potential gradients measured at corresponding points on the curved and on the flat sides of the model was as much as 10 per cent when r/d or D/d became large. Jacobsen suggests that his results are subject to

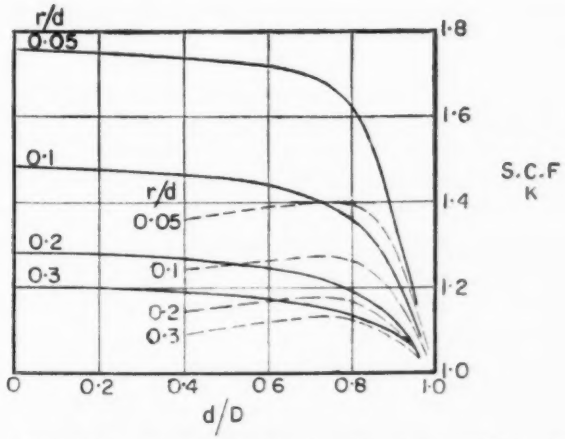

FIGURE 6. Comparison of the combined results of Jacobsen and Wiegand with those of the present investigation.
——— Jacobsen[2] (electrical analogue) and Wiegand[3] (precision strain gauge).
— — — Allison.

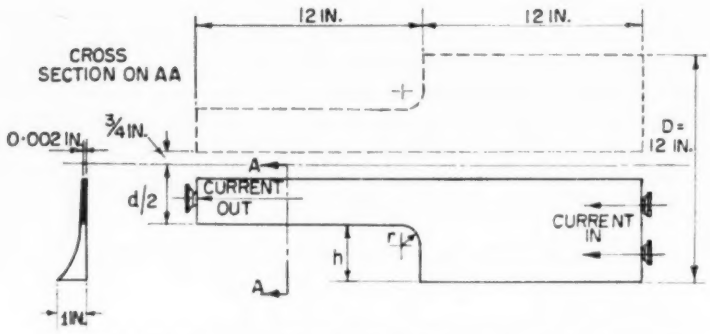

FIGURE 7. Diagram showing the model used by Jacobsen, and the dimensions of the shaft which it represents.

the greatest inaccuracy in these regions and it is interesting to note that the maximum divergence between his results and those of the present investigation occurs for small d/D ratios.

Wiegand obtained results in the range $0{\cdot}1 < r/D < 0{\cdot}25$, using a strain gauge of 1·3 mm. gauge length. For large values of d/D, the results of these tests are in agreement with those of the present investigation. Despite the fact that Wiegand's experiments cover the range $0 < d/D < 0{\cdot}5$, no decrease in the s.c.f. is predicted for the smaller values of d/D. From a sample calculation it appears that the maximum strain measured in the tests was of the order of $4{\cdot}3 \times 10^{-5}$ (*i.e.* an extension of 2×10^{-5} inches). It seems unlikely that the measurement of quantities of this order would lead to the calculation of stress concentration factors having an accuracy which is better than ± 10 per cent, although Wiegand estimates the accuracy of his curves to be ± 5 per cent. The difference in the results may be attributed to the fact that Wiegand used the base length of a mechanical extensometer to measure strains which actually occur on a curved arc. This would explain the divergence of the families of curves as r/d decreases and the fact that the position of the peak stress recorded by Wiegand is farther up the fillet than has been found in the present investigation.

Undoubtedly the s.c.f. for small d/D ratios are too high to be reconciled with the photoelastic results, even if the maximum error band is put on the families of curves, and it can only be concluded that the results obtained in this region by Jacobsen and Wiegand are incorrect.

It can be shown, in the particular case of the torsion of a cylindrical shaft of variable cross section, that the stress system is non-dilational and is therefore independent of the elastic constants. The implication of this result is that the stress systems in geometrically similar shafts, made of different materials, will be exactly comparable and that the stress concentration factors obtained using a photoelastic resin as the shaft material will be identical with those obtained in a similar steel shaft.

The only attempt to obtain a theoretical solution for the shouldered shaft in torsion is that due to Sonntag[4] who has taken a polynomial solution of the torsion function ϕ in an attempt to solve the problem for a number of grooves and shoulders. He does not fully satisfy the boundary conditions in any of the cases and, for the shouldered shaft in particular, considers only the first four terms of the solution, without first establishing the convergence of the series. No reliance can be placed upon the results obtained by Sonntag.

ACKNOWLEDGMENTS

The author wishes to thank Col. H. T. Jessop and Mr. C. Snell for their kind help, advice and criticism throughout the period of this research.

REFERENCES

1. JESSOP, H. T., SNELL, C. and ALLISON, I. M. The Stress Concentration Factors in Cylindrical Tubes with Transverse Circular Holes. *The Aeronautical Quarterly*, Vol. X, p. 326, November 1959.

2. JACOBSEN, L. S. Torsional Stress Concentrations in Shafts of Circular Cross Section and Variable Diameter. *Transactions of the American Society of Mechanical Engineers*, Vol. 47, p. 619, 1925.

3. WIEGAND, A. Determination of the S.C.F. of a Stepped Shaft Stressed in Torsion, by Means of a Precision Strain Gauge. *Luftfahrtforschung*, Vol. 20, p. 217, July 1943. Translation N.A.C.A. T.M. 1179, September 1947.

4. SONNTAG, G. Grooves in Shafts Subjected to Torsion. *Zeitschrift für angewandte Mathematik und Mechanik*, Vol. 9, p. 1, 1929.

Review

Jet Propulsion Engines. Volume XII of *High Speed Aerodynamics and Jet Propulsion*. Edited by O. E. Lancaster. Oxford University Press, London, 1959. 799 pp. Illustrated. £7.

Most readers must surely have met earlier volumes of this admirable series, whose only and inescapable fault is that they are so packed with information that their price individually, let alone *in toto*, is bound to deter many who would wish to possess them. So it may be said at the outset that the volume under review is well up to standard. As a collective work, it is probably best to deal with it by taking the various contributions separately.

A. *Historical Development of Jet Propulsion*, by F. J. Malina, R. C. Truax and A. D. Baxter, is an admirably concise survey of the history of the various forms of reaction engine (including rockets, a legitimate inclusion under the heading of the book which is pursued later), and has a valuable bibliography.

B. *Basic Principles of Jet Propulsion*, by Maurice Roy, is the expected masterly disentanglement of the subtle and often misunderstood intricacies of thermal and propulsive efficiencies for various engine configurations.

C. *The Turbojet Engine*, by C. A. Meyer, is a selection of topics under this heading, covering performance and control, thrust augmentation and testing; the diagrammatic presentation of the matching problem on page 128 repays close study.

D. *The Turboprop Engine*, by I. H. Driggs and O. E. Lancaster, not only presents the highly original method of performance analysis which the authors have made familiar in other publications, but also takes note—not before time—of the fact that the turboprop has a "prop" as well as a "turbo", and spends useful time discussing propeller performance.

E. *The Ramjet Engine*, by D. D. Wyatt and B. T. Lundin, is, again, chiefly concerned with performance aspects, including the very important topic of variation of specific heats, but it also gives a survey of the characteristics of test facilities.

F. *Intermittent Jets*, by J. V. Foa, discusses not only the pulsejet, but also a variety of less-familiar proposals for cyclically-operating air-breathing engines.

G. *The Liquid Propellant Rocket Engine*, by M. Summerfield, is less analytical than some of the preceding sections and goes more fully into design considerations. Paradoxically, it is nevertheless devoid of worthwhile photographs of current practice, unlike the earlier parts.

H. *Solid Propellant Rockets*, by C. E. Bartley and M. M. Mills, places more emphasis on combustion problems and grain design, as is to be expected, but again dwells briefly on mechanical design.

I. *The Ramrocket*, by I. Glassman and J. V. Charyk, is necessarily a mainly theoretical survey.

J. *Jet Rotors*, by A. Gail, discusses the dynamics and aerodynamics of jet-driven helicopter and propeller blades.

K. *Atomic Energy in Jet Propulsion*, by R. Zirkind surveys, in turn, nuclear physics, reactor principles, shielding and cooling.

L. *Future Prospects of Jet Propulsion*, by F. Zwicky, applies morphological and topological principles to the discussion of possible future forms of engine, and will certainly cause most readers to wonder what has hit them.

It will have been seen that the mere statement of the various fields covered by this vast book has taken a lot of space. An overall assessment is very hard to make fairly. One feels that considerations of space and time have militated against any close integration of the various topics covered, some of which should not have received such full treatment in a balanced review of the jet propulsion field at large: this is particularly true of Sections F, I, J, and K. Contrariwise, some mention of such things as ion rockets, turbo-rockets and the various forms of turbo-fan would have had more general appeal than the high-flown language of much of Section L.

Were the last of these sections to be replaced by a more conventional peep into the future, and the rest coalesced into a shorter précis of fringe topics, one would have had a golden, rather than a curate's, egg. As it is the authors have dealt nobly with an enormous field, and their joint labours form a classic milestone. But what a pity the editor issued invitations to contribute so freely: and surely the title ought to be more honest about the primarily performance and theory bias of the whole work.

Nevertheless, no serious student of the propulsive art ought to neglect to dip into this book variously and often, for he will find much to inform, stimulate, puzzle and occasionally infuriate him.

J. R. PALMER.

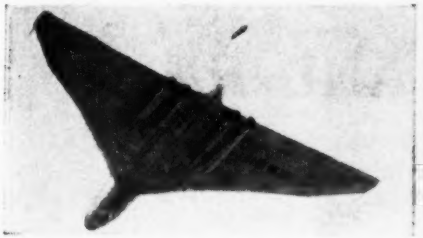

The Bristol Siddeley Olympus turbojet powers the Avro Vulcan V-bomber.

The Bristol Siddeley Gamma rocket motor powers the Saunders-Roe Black Knight space probe.

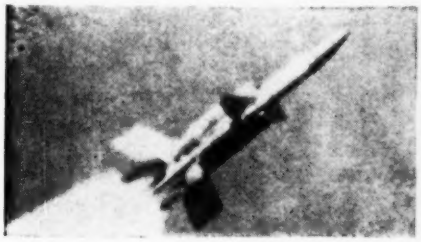

The Bristol Siddeley Thor ramjet powers the Bristol/ Ferranti Bloodhound guided missile.

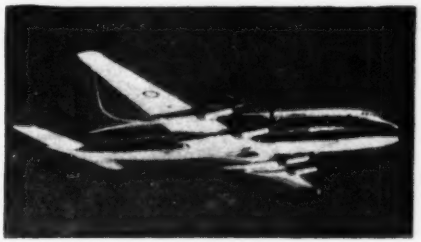

The Bristol Siddeley Proteus turboprop powers the Bristol Britannia military transport.

The Bristol Siddeley Marine Proteus powers the "Brave" class 96-ft boats built by Vosper Ltd.

Bristol Siddeley Maybach diesel engines power the British Railways "Bristolian" express.

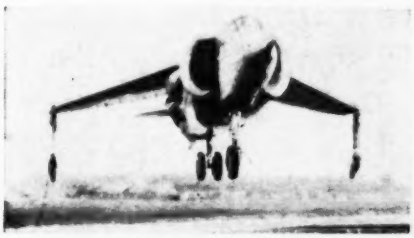

The Bristol Siddeley BS 53 turbofan powers the Hawker P 1127 VTOL strike fighter.

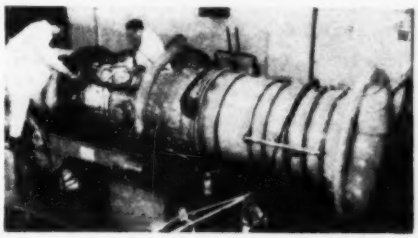

The Bristol Siddeley Olympus will power BAC's new tactical/support reconnaissance aircraft—the TSR 2.

BS

Bristol Siddeley Engines Limited—one of the largest producers of motive power units in the world

CHAPMAN AND HALL

Published under the authority of the
Royal Aeronautical Society

AIRCRAFT HYDRAULICS

edited by **H. G. CONWAY**

Volume I—Hydraulic Systems

Size 10 in. x 6 in. 146 pages 107 illustrations

35s. net

Volume II—Component Design

Size 10 in. x 6 in. 216 pages 120 illustrations

45s. net

INSTRUMENTATION IN TESTING AIRCRAFT

by **C. N. JAQUES**

Size $8\frac{3}{4}$ in. x $5\frac{1}{2}$ in. 292 pages 117 illustrations

45s. net

LANDING GEAR DESIGN

by **H. G. CONWAY**

Size 10 in. x 6 in. 342 pages 366 illustrations

56s. net

AIRCRAFT ELECTRICAL ENGINEERING

edited by **G. G. WAKEFIELD**

Size 10 in. x 6 in. 350 pages 201 illustrations

50s. net

37 ESSEX STREET - LONDON WC2

NOTICE TO CONTRIBUTORS

1. All communications should be addressed to the Editor, The Aeronautical Quarterly, 4 Hamilton Place, London, W.1.

2. Papers for consideration should be typewritten with double spacing and be accompanied by a summary of not more than 250-300 words. *Papers must be as short as possible*, otherwise considerable delay in publication will result, and in any case they should not be longer than twenty foolscap pages. Full descriptions and complete results of work, as written for an internal report, are not suitable for publication in *The Aeronautical Quarterly*, and such reports need to be rewritten in concise form. Only necessary equations should be included in the text; routine mathematics should be omitted or given as an Appendix to the paper. Illustrations should be reduced to a minimum. The titles of papers should be kept short—with sub-titles if necessary.

3. Only simple symbols and formulae should be typewritten. All others should be written clearly in ink. Greek letters should be indicated and a clear distinction drawn between capital and small letters. Particular attention should be paid to the use of alpha and *a*, kappa and *k*, mu and *u*, nu and *v*, eta and *n*. The letter *l* must be distinguished from the numeral 1, and the letter *O* from the zero 0.

   The use of dots, bars, and so on, over letters, or the use of dots as multiplication signs and bars for brackets should be avoided as far as possible.

   Suffixes and prefixes must be indicated clearly and complicated suffixes and prefixes should be avoided.

4. A list of *all* symbols used, both in the illustrations and text, *must* be given whether they are standard or not.

5. *Clear* diagrams or sketches must be submitted for redrawing by the Society's draughtsman.

   Photographs must be not less than half plate size and must be clear black and white glossy prints.

6. References should be given in the form:—
   WARD, G. N. Calculation of Downwash Behind a Supersonic Wing. *The Aeronautical Quarterly*, Vol. I, p. 35, May 1949.

7. The copyright of every paper printed in *The Aeronautical Quarterly* is the property of The Royal Aeronautical Society. Permission to reprint or to use any paper will not be unreasonably refused.

8. It is a condition of publication that the author shall have obtained consent where necessary to use any material in his paper which is copyright or the property of any other person or his employers.

9. Authors will be entitled to 20 reprints of their papers free of charge. This number will be shared between joint authors.

The Aeronautical Quarterly is published at the Offices of The Royal Aeronautical Society, 4 Hamilton Place, Piccadilly, London, W.1, at 15s. 0d. net for a single number to non-members and 7s. 6d. net for a single number to members of The Royal Aeronautical Society. Instructions for Contributors are given above. None of the papers must be taken as expressing the opinion of the Council of The Royal Aeronautical Society unless such is definitely stated to be the case. All communications for publication or advertisement in The Quarterly should be addressed to—The Editor, The Aeronautical Quarterly, 4 Hamilton Place, W.1.

Telephone: Grosvenor 3515. Telegraphic Address: Didaskalos, Audley, London

THE AERONAUTICAL QUARTERLY

It is the aim of *The Aeronautical Quarterly* to attract not only original papers contributing to aeronautical science and engineering, and papers developing new or improved methods of analysis and experimental techniques, but also papers on allied sciences which have a bearing on aeronautical problems. *The Aeronautical Quarterly* is open to authors of any nationality and is not restricted to members of the Society. Most papers can be published within nine months of receipt. Short papers, of not more than 2,000 words, are published much more quickly.

VOLUME XII

Volume XII of *The Aeronautical Quarterly* will be published in four parts, in February, May, August and November 1961. The prices, *including postage and packing*, are:—

	To Members of the Society		*To Non-Members*	
	£ s. d.		£ s. d.	
Per Part	8 0	($1.15)	15 6	($2.20)
Subscription (4 parts)	1 12 0	($4.50)	3 2 0	($8.70)

Papers to be published in future issues include:—

J. H. B. Smith—Lift/Drag Ratios of Optimised Slewed Elliptic Wings at Supersonic Speeds.

D. B. Spalding—The Theory of Melting Ablation, with Vaporisation, Gas-Phase Chemical Reaction, Surface Pyrolysis and Transient Effects.

R. H. Gallagher and I. Rattinger—An Experimental and Theoretical Study of Low Aspect Ratio Wing Behaviour.

S. C. Redshaw and K. R. Rushton—A Study of the Various Boundary Conditions for Electrical Analogue Solutions of the Extension and Flexure of Flat Plates.

N. Curle—The Effects of Heat Transfer on Laminar-Boundary-Layer Separation in Supersonic Flow.

I. T. Cook and K. C. Rockey—Shear Buckling of Clamped and Simply-Supported Infinitely Long Plates Reinforced by Transverse Stiffeners.

D. S. Houghton and D. J. Johns—A Comparison of the Characteristic Equations in the Theory of Circular Cylindrical Shells.

I. M. Allison—The Elastic Stress Concentration Factors in Shouldered Shafts. Part II.

G. J. Hancock—The Static Aeroelastic Distortion of Slender Configurations. Parts I and II.

PRINTED BY THE LEWES PRESS WIGHTMAN & CO. LTD., LEWES, SUSSEX, ENGLAND, AND PUBLISHED BY THE ROYAL AERONAUTICAL SOCIETY, 4 HAMILTON PLACE, LONDON W.1, ENGLAND.